

Lawrence Berkeley National Laboratory

Recent Work

Title

THE PHOTODISSOCIATION OF WATER OVER DOPED IRON OXIDES: MATERIALS AND MECHANISMS

Permalink

<https://escholarship.org/uc/item/1wz80937>

Author

Hendewerk, M.L.

Publication Date

1985-11-01



Lawrence Berkeley Laboratory

UNIVERSITY OF CALIFORNIA

Materials & Molecular Research Division

RECEIVED
LAWRENCE
BERKELEY LABORATORY

OCT 16 1986

LIBRARY AND
DOCUMENTS SECTION

THE PHOTODISSOCIATION OF WATER OVER DOPED IRON
OXIDES: MATERIALS AND MECHANISMS

M.L. Hendewerk
(Ph.D. Thesis)

November 1985

TWO-WEEK LOAN COPY

*This is a Library Circulating Copy
which may be borrowed for two weeks.*



LBL-22142
c.2

DISCLAIMER

This document was prepared as an account of work sponsored by the United States Government. While this document is believed to contain correct information, neither the United States Government nor any agency thereof, nor the Regents of the University of California, nor any of their employees, makes any warranty, express or implied, or assumes any legal responsibility for the accuracy, completeness, or usefulness of any information, apparatus, product, or process disclosed, or represents that its use would not infringe privately owned rights. Reference herein to any specific commercial product, process, or service by its trade name, trademark, manufacturer, or otherwise, does not necessarily constitute or imply its endorsement, recommendation, or favoring by the United States Government or any agency thereof, or the Regents of the University of California. The views and opinions of authors expressed herein do not necessarily state or reflect those of the United States Government or any agency thereof or the Regents of the University of California.

The Photodissociation of Water over Doped Iron Oxides:
Materials and Mechanisms

Monica Hendewerk

Ph.D. Thesis

November 1985

The Photodissociation of Water over Doped Iron Oxides:
Materials and Mechanisms

Monica Hendewerk

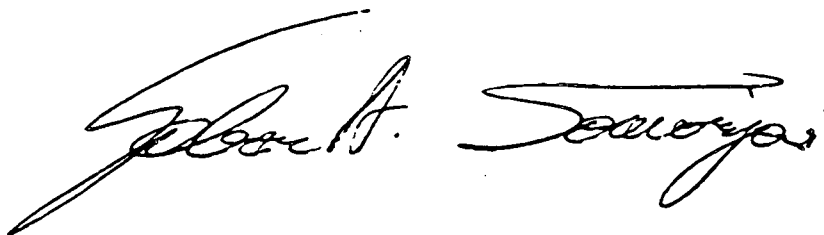
Materials and Molecular Research Division
Lawrence Berkeley Laboratory,
and Department of Chemistry
University of California, Berkeley, CA 94720

Abstract

The main goal of this project has been to study the possibility of economically converting solar energy to chemical energy. It was found that two iron oxide electrodes, one containing MgO and the other SiO₂, connected to form a short circuited assembly would successfully photodissociate water when illuminated with light. No external energy source was necessary. The power conversion efficiency of this cell proved to be low. Extensive research followed in which the Mg-doped electrode and the short circuited assembly were thoroughly characterized. Although the Mg-doped material is not a true p-type semiconductor, it possesses very unique properties. In photoelectrochemical experiments, the Mg-doped ceramic discs produce cathodic currents under illumination. Sintered discs of Si-doped and Mg-doped α -Fe₂O₃ give measurable photocurrents when put in ohmic contact with each

other to form a short circuited assembly in which both H_2 and O_2 are produced from water.

As a supplement to these studies and as a correlation to water photodissociation, experiments have been performed using ultra high vacuum techniques (thermal desorption spectroscopy, ultraviolet photoelectron spectroscopy, and x-ray photoelectron spectroscopy to study the reaction of H_2O with stoichiometric and partially reduced single crystals of $\alpha-Fe_2O_3$ (basal plane). K was added to simulate the presence of alkali metals in the electrolyte solution used in the short circuited assemblies. Reduced iron oxides were produced which are stable to relatively high temperatures (500 K) due to an oxidized outermost layer. Substrate water interactions on the reduced iron oxide crystals are dissociative, while on the oxidized crystal they are not. K interacts strongly with the iron oxide surface and again the water adsorption properties were dissociative.

A handwritten signature in cursive script, appearing to read "Robert A. Sauerbrey". The signature is written in dark ink on a white background.

To my mother, with love

Acknowledgements

First and foremost I must thank Gabor Somorjai. An itemized list of his contributions to my graduate career and my future would be longer than my thesis. This has been a most profitable four years. I cannot think of a better advisor, a better group, or a better school to have gotten a Ph.D. from.

I owe many many thanks to Chris Leygraf who started me off on the right foot and starred with me in the celebrity year of 1982 when hydrogen was it instead of coke.

As a result of some avaricious dreams of economic feasibility, this project bloomed at an accelerated rate. It was extremely exciting. The consequence of this promise to science was an enormous interest in the project so that the results compiled here, by me, are a combination of the ambitious ideas and collaborative work of many people. None of these gifted minds belonged to graduate students, so that the writing of my thesis stands to be the first opportunity to bring together all of the widely varying experiments and results which have been been acquired by attacking this problem from different perspectives in different corners of the laboratory: from solid state bulk properties of the electrode material generated with synthetic inorganic expertise to the electrochemical results as studied by true solution chemists, to the very physical spectroscopic studies of the near surface region in ultra high vacuum.

I would like to thank Kurt Sieber and Clement Sanchez who gave the project a much needed redirection toward materials research and who generously shared their knowledge and the tricks of the trade

for making single crystals. I am also grateful for many stimulating discussions and ideas from Miguel Salmeron in the last year.

In addition, I should acknowledge Hiroshi Nakanishi, Dave Neiman, and John Turner for their contributions to the water project.

The entire technical and support staff of MMRD deserve thanks for making progress possible. The electronics shop was my favorite place to go. Power supplies always failed at crucial moments, yet I cannot remember a time when Jim Severns did not miraculously fix my box very quickly and with a smile on his face. Of course, without Glenn Baum, Hank Brundle, Keith Franck, John Holthuis, Don Krieger, Cathy Sterling, and Sandy Stewart, I would never have gotten anywhere.

Last but not least, I must thank my family and friends for their never ending support, encouragement, and pride. Randy Grimes has always been there to make my day a happy one.

The dedication of my thesis to my mother is only a small compensation for all that she has given to me.

This work was supported by the Director, Office of Energy Research, Office of Basic Energy Sciences, Material Science Division of the U.S. Department of Energy under contract number DE-AC03-76SF00098.

Table of Contents

Abstract.....	1
Acknowledgements.....	ii
Chapter One: Introduction.....	1
Figures.....	11
References.....	19
Chapter Two: Experimental.....	22
Doping of Semiconductor Electrodes.....	22
The Space Charge Layer.....	25
Materials Preparation	
Synthesis of Doped Polycrystalline Iron Oxides.....	27
Single Crystal Growth of Doped Iron Oxides.....	27
Characterization	
Bulk X-ray Diffraction.....	28
Scanning Electron Microscopy.....	30
Electrical Properties.....	30
Magnetic Susceptibility.....	31
DC Photoelectrochemical Measurements.....	31
Depletion Layer Capacitance Measurements.....	35
AC Photoelectrochemical Measurements.....	38
Figures.....	40
References.....	52
Chapter Three: Results and Discussion.....	53
Polycrystalline Mg-doped and Si-doped Iron Oxides.....	53
The Onset for Photocurrent.....	54
The Influence of Sintering Temperature on Mg-doped Iron Oxide..	59
Composition vs Sintering Temperature and Dopant Concentration..	63

Electrical Properties Governed by Sintering Temperature and Dopant Concentration.....	65
Photocurrent Response to Variations in Mg Dopant Levels.....	66
The Effect of O ₂ Purging of the Electrolyte Solution on Photocurrent.....	67
pH Dependence of Photocurrents.....	68
Stability of the Photocurrents of the Mg-doped Iron Oxides.....	69
Figures.....	73
References.....	90
Chapter Four: A Short Circuited Iron Oxide Assembly For the Photodissociation of Water.....	92
Depletion Layer Capacitance Measurements.....	94
The Production of H ₂ and O ₂ Gases From the Short Circuited Assembly.....	103
Long Term Stability of the Iron Oxide Semiconductor Assembly..	108
Reproducibility of Photocurrents and H ₂ Gas Production.....	109
AC Photoelectrochemical Measurements.....	111
Figures.....	115
References.....	131
Chapter Five: Ultra High Vacuum Studies.....	134
Introduction.....	134
Ultra High Vacuum Surface Analysis.....	135
X-ray Photoelectron Spectroscopy.....	136
Ultraviolet Photoelectron Spectroscopy.....	139
Auger Electron Spectroscopy.....	141
Argon Ion Bombardment.....	142
Low Energy Electron Diffraction.....	142

Thermal Desorption Spectroscopy.....	144
Data Treatment.....	146
Results and Discussion	
Oxidized/Reduced Single Crystals: Work function changes..	146
Thermal Desorption of Water from Iron Oxide.....	148
Interactions of Water with Iron Oxide Single Crystals....	151
Water Interactions on a K Covered Surface.....	153
Conclusions.....	155
Figures.....	156
References.....	184

Chapter One

Introduction

The main goal of this project has been to study the possibility of economically converting solar energy to chemical energy. It was decided to focus on using semiconductors and light for assisting the thermodynamically uphill reaction of dissociating water to form hydrogen and oxygen gas. Hydrogen is an important fuel. It can be used as a gas or converted to a metal hydride and transported before extracting the stored energy. The first objective was to find a semiconducting material which would be suitable for photodissociating water in a p/n diode assembly.

Many photoelectrochemical studies aimed at the photodissociation of water with semiconductor electrode systems require the use of an applied external bias in addition to irradiation by light of greater than bandgap energy (REF 1.1). Various ways to eliminate the need for an external potential have been explored (REF 1.2-1.5). One such way is to use a photochemical diode cell in which photoactive p-type and n-type semiconductors are put in ohmic contact in a short circuit configuration as a photocathode and photoanode for oxidation and reduction reactions (REF 1.6-1.9). Another method would be to incorporate the two electrodes into one by depositing metal catalysts on semiconductor electrodes. Such photocatalytic devices would be valuable if they could be used for the generation of H_2 and O_2 in two separate compartments. This would provide a means of transforming solar power into either chemical energy by collecting H_2 , or into electrical energy by utilizing the

photocurrent between the p-type and n-type electrodes.

Previous experiments in this laboratory showed that SrTiO_3 when coated with a thin film of platinum produced H_2 gas from H_2O at very high rates without any external applied bias (REF 1.10). However, the bandgap of this material is in the ultraviolet so that very little of the radiation from the sun is utilized, and platinum is a very expensive catalyst. It was for this reason that a search was made for a more suitable material. The most important criteria were that the material have a bandgap which would allow a greater portion of the sun's energy to be utilized, that the electrodes exhibit stability in solution, and that the system be economically practical to use as a means of converting water to hydrogen and oxygen gases.

There have been many discussions about suitable materials for photocatalytic reactions using solar energy (REF 1.11-1.14). Ferric oxide (Fe_2O_3) is a good candidate for such reactions. It is abundant and therefore inexpensive, and it is stable in both acidic and basic aqueous solutions. The most attractive features are that it has large absorption coefficients (REF 1.15) and a bandgap of 2.2-2.3 eV (REF 1.16-1.20) which is in the visible region of the solar spectrum and allows the utilization of 40% of the radiation from the sun (Figure 1.1).

The photoelectrochemical characteristics of n-type iron oxides for water decomposition using $\alpha\text{-Fe}_2\text{O}_3$ or metal-deposited $\alpha\text{-Fe}_2\text{O}_3$ in the form of single crystals (REF 1.21,1.22), polycrystalline discs (REF 1.23-1.26), and thin films (REF 1.27-1.32) have been extensively studied. The theoretical efficiency

of a semiconductor electrode with a bandgap of 2.2 eV is > 20 percent (Figure 1.2). Whereas a large number of n-type Fe_2O_3 photoelectrodes have been successfully used, no p-type Fe_2O_3 has so far been shown to exhibit photocatalytic behavior (REF 1.33-1.37).

It was our goal to develop a p/n diode assembly comprised of doped iron oxides. Of the many attempts at doping polycrystalline sintered iron oxide discs with divalent cations to produce a suitable cathode for such a p/n diode assembly, the best results were obtained by the addition of Mg in the form of MgO to $\alpha\text{-Fe}_2\text{O}_3$ using previously reported techniques for producing sintered n-type iron oxides (REF 1.26). Although a true p-type diode was never produced, a very unique material was developed.

In photoelectrochemical experiments, the Mg-doped ceramic discs as photoelectrodes show cathodic currents under illumination, but do not exhibit true p-type diode characteristics. Nonetheless, this Mg-doped iron oxide material can be used as a photocathode in aqueous solution and will operate in a short-circuited assembly in which H_2 and O_2 are produced from water. Sintered discs of Si-doped and Mg-doped $\alpha\text{-Fe}_2\text{O}_3$ give measurable photocurrents (Table 1.1) when put in ohmic contact with each other to form a short circuited assembly as shown in Figure 1.3.

There are several requirements which must be met in order for the photodissociation of water to take place in a short circuited p/n diode assembly. The dissociation of water to hydrogen and oxygen requires energy of $\Delta G_{298} = 4.6 \text{ eV}$ (228 kJ/mol). Irradiating a semiconductor assembly with one electrode having the conduction band located negative of the H^+/H_2 redox couple and

TABLE 1.1

Measured Photocurrents in Iron Oxide Assemblies
After One Hour of Exposure in 0.01 N NaOH

n-type: $\text{Si}/(\text{Si} + \text{Fe}) = 2 \text{ atom } \%$

Mg-doped: $\text{Mg}/(\text{Mg} + \text{Fe}) = 1, 5, 10 \text{ and } 20 \text{ atom } \%$

Mg/(Mg + Fe) (atom %)	1	5	10	20
	<u>Photocurrent (μA)</u>			
Both electrodes illuminated	5	8	13	3
Only n-type illuminated	2.5	2.5	3.5	2.5
Only Mg-doped illuminated	1.5	1.5	4	0.5
no illumination	<0.5	<0.5	<0.5	<0.5

the other electrode with the valence band positioned at an energy more positive than the O_2/OH^- redox couple on an electrochemical scale with light, one may produce electrons in the excited state and electron vacancies at the surface that can perform the photochemical reduction ($2H^+ + 2 e^- \rightarrow 2H \rightarrow H_2$) and oxidation ($2OH^- + 2e^- \rightarrow H_2O + 1/2 O_2$) of water. These specific thermodynamic criteria must be satisfied for this process to be feasible. The conduction band edge of the p-type semiconductor in solution must lie at a potential more positive than the $H^+ + e^- \rightarrow 1/2H_2$ half cell potential. Similarly, the valence band edge of the n-type semiconductor must be more negative than the $2OH^- \rightarrow 2e^- + 1/2 O_2 + H_2O$ half cell potential (Figure 1.4). When the electrodes are immersed in an aqueous solution a depletion layer is formed in the near surface region of the semiconductor at the electrode/electrolyte interface. This depletion layer is essentially an electric field which serves as a force for driving electrons or holes to the surface in n-type and p-type semiconductors, respectively. Electrons at the surface of the p-type photocathode mediate the conversion of hydronium ions to hydrogen gas, while electron vacancies oxidize hydroxyl species to oxygen at the n-type photoanode. The majority carriers recombine to contribute to the measured photocurrents. These requirements dictate that the semiconductor bandgap be greater than 1.23 eV, the one electron potential needed to dissociate water ($H_2O \rightarrow H_2 + 1/2 O_2$, $\Delta E_0 = 1.23$ eV), and that one of the semiconductors have a majority of positive carriers (p-type) while the other electrode have a majority of negative carriers (n-type).

A number of semiconductors which satisfy these basic thermodynamic criteria are shown in Figure 1.5. The smaller bandgap materials (i.e. sulfides) are more reactive than the larger bandgap materials (i.e. oxides) (Figure 1.5). A large proportion of these undergo side reactions in aqueous solution which result in corrosion or decomposition of the electrode surface rendering them inactive. In addition, these smaller bandgap materials fall in a region of low spectral flux density from the sun (Figure 1.6). Many of the transition metal oxides are excellent candidates for water photodissociation since the bandgaps are large enough to afford some stability in solution and small enough to utilize the radiation from the sun.

Iron oxide, $\alpha\text{-Fe}_2\text{O}_3$, satisfies both criteria. It has a band gap of 2.3 eV which is large enough that photocorrosion of the electrode in aqueous solutions is not a problem, and small enough so that visible light can be used to excite electrons from the valence band to the conduction band in order to initiate the photodissociation process. Pure and doped $\alpha\text{-Fe}_2\text{O}_3$ have been shown to be good n-type electrodes, but have not been known to have conduction band molecular orbitals available for the transmission of electrons with energies compatible with the requirements for hydrogen reduction in an aqueous solution.

In this study, it has been found that by cosintering MgO and $\alpha\text{-Fe}_2\text{O}_3$ at high temperatures the valence band of the Mg-doped electrode and the conduction band of the Si-doped electrode are positioned at energies with respect to the redox couples in solution (H^+/H_2 and O_2/OH^-) such that the simultaneous evolution of

H₂ and O₂ from water with an iron oxide short circuited assembly is thermodynamically feasible (REF 1.38).

As is shown in Table 1.1 the greatest current flow occurred upon simultaneous illumination of both semiconductors. This photocurrent was always greater than the sum of the current from illuminating only one of the electrodes in the assembly. It is also noteworthy to mention that for the p/n assemblies the dark currents were very small (~0.5 μ A). This is a good indication that there were no corrosion processes or other reactions occurring in the dark.

Table 1.1 shows the measured photocurrents and hydrogen production from one such assembly. The economic feasibility of utilizing such an assembly for commercial solar energy conversion is not only dependent upon the cost of the materials but the output power of the device per unit time. The chemical output power of the polycrystalline assembly can be calculated either from the photoinduced hydrogen production rate or from the measured photocurrents across each p/n assembly using photon energies in the visible range of the solar spectrum. By integrating the photocurrents from our best assembly and assuming that all electrons which cross the electrode/electrolyte interface proceed to reduce hydronium ions to H₂ gas molecules, a power conversion efficiency of slightly less than 0.05% was obtained. This can be compared with other p/n photoelectrolytic cells in which efficiencies were reported which were one order of magnitude higher (REF 1.8,1.9). These cells contained single crystal TiO₂ (E_g = 3.0 eV) or SrTiO₃ (E_g = 3.2 eV) as n-type electrodes and required considerably higher photon energies than the present cell which

would make them unlikely candidates for photochemical solar energy conversion.

A p/n diode assembly which demonstrates a power conversion efficiency of 0.05% does not constitute a commercial solar energy conversion system. After the initial discovery of a working short circuited iron oxide assembly much time was devoted to understanding the iron oxide system that had been created and characterizing the electrodes, particularly the Mg-doped iron oxide. In order to increase the efficiency of this electrochemical cell it was necessary to focus on each of the fundamental steps involved in the photodissociation process individually to ascertain its contribution to the functionality of the cell. The basic steps involved in the water photodissociation process on the p-type electrode are outlined in Figure 1.7. Illumination of the semiconductor with light having energy greater than the bandgap of the material excites an electron from the valence band into the conduction band. This electron hole pair is separated by an electric field gradient which drives the minority carrier to the surface of the electrode. In subsequent steps ionic species are adsorbed onto the surface and electronic transfer of the minority carrier across the electrode/electrolyte interface occurs. The reduced (p-type) or oxidized (n-type) species may undergo a further reaction such as the recombination of two hydrogen atoms to form H_2 before being desorbed from the surface. Within these steps are many parameters which control the efficiency of an electrochemical cell: the bandgap, bulk, surface and grain boundary recombination rates of photogenerated electron hole pairs, absorption of light by the electrode and the electrolyte solution,

the internal cell resistance and the electrode kinetics.

Since the open circuit voltage, V_{oc} , increases as the bandgap energy increases and the efficiency of a short circuited p/n cell is directly proportional to the open circuit voltage it is advantageous to use the largest bandgap material possible. However, efficient use of the solar spectrum is also important. The bandgap must be small enough to utilize visible light. Bulk material, surface states, and grain boundaries all increase the cross section for non-radiative recombination processes which obviously reduce the rate of electron transfer across the electrode/electrolyte interface thereby decreasing the efficiency of the cell. The reduction of protons to form hydrogen molecules depends heavily on the electrode kinetics, i.e. the adsorption, reduction, and recombination steps.

In the electrochemical cell we found that reduced iron oxides act as p-type photocathodes in an alkali metal hydroxide solution. A more detailed examination of the nature of these reduced iron oxide states was performed via ultra high vacuum analysis techniques. Single crystals of pure and Ge-doped α - Fe_2O_3 were synthesized to study the interaction of water and alkali metals with the iron oxide surface under ultra high vacuum conditions. In the UHV chamber it was shown that reduced iron oxides can be produced which are stable to relatively high temperatures (500 K). Oxidation of the outermost exposed layers occurs very rapidly, but the reduced Fe species lying below the surface are protected by this outer oxidation layer and remain reduced even at high temperatures. After exposure to thousands of Langmuirs of water and subsequent annealing only a few of the outermost layers are oxidized. These deep lying

reduced species are primary contributors to the catalytic activity of a short circuited iron oxide assembly.

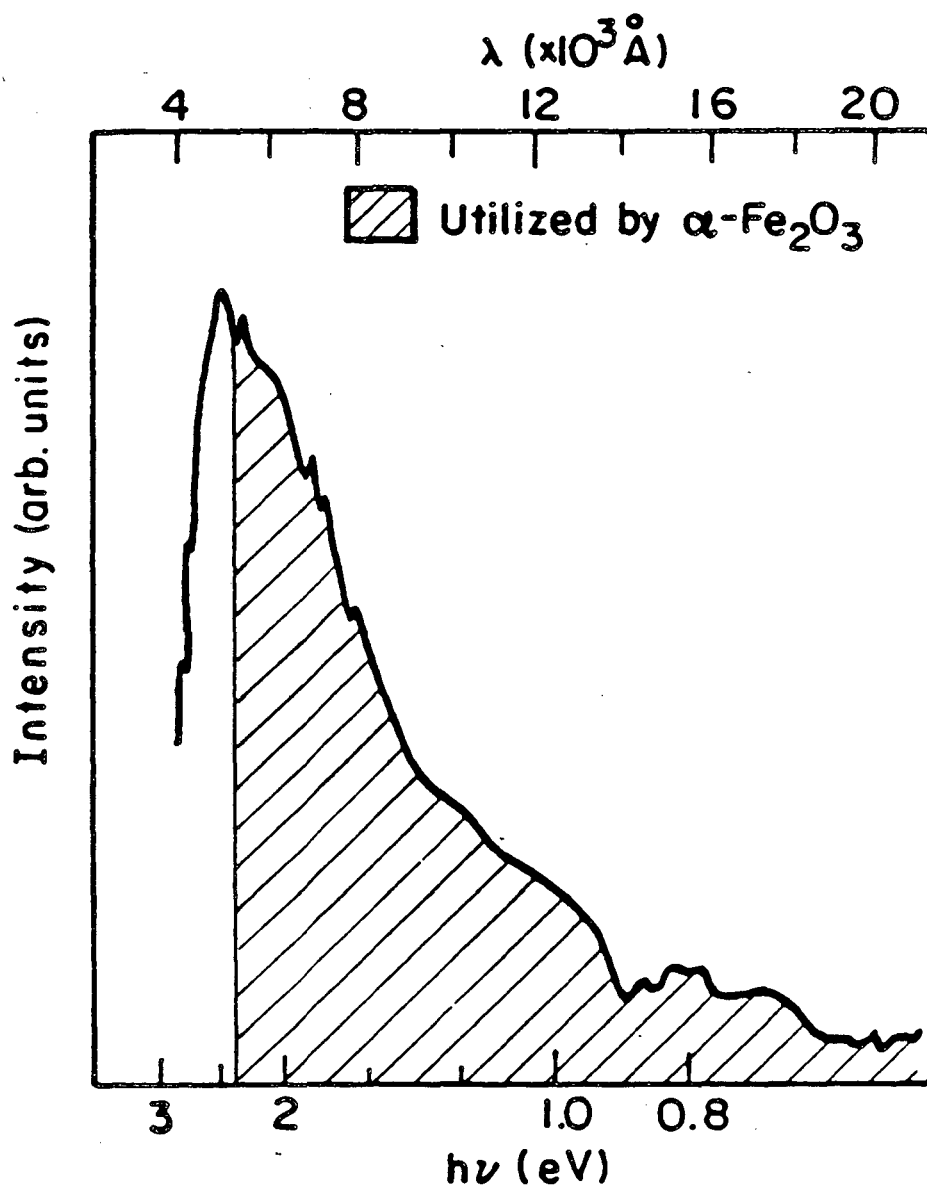
H₂ production was not observed in the UHV experiments when light was used to photodissociate adsorbed water on the single crystals, because the kinetics of the dissociation reaction were too slow. It is also possible that the (001) face of α -Fe₂O₃ is not the active face in the photodissociation process. Thermal desorption studies revealed that substrate-water interactions on the (001) basal plane of a fully oxidized stoichiometric α -Fe₂O₃ crystal are very weak as evidenced by the lack of multiple desorption peaks for the mono- and multilayers of water. Because of the rapid formation of an oxidized layer on the sputter reduced iron oxide, it too, exhibits weak water-substrate interactions.

The presence of the alkali metal in the electrolyte solution of the p/n assembly apparently has little effect on the photodissociation process. K interacts very strongly with the iron oxide surface, but does not change the water adsorption properties on the iron oxide surface. K cannot be thermally desorbed nor does it penetrate into the bulk. It is easily removed with light argon ion sputtering. Water decomposes on the K to form K-OH and subsequent annealing breaks the O-H bond to give H₂ gas leaving the O behind as a potassium oxide.

In the past four years the Mg-doped iron oxide material and the short circuited assembly have been characterized macroscopically and microscopically, piece by piece and as a whole. Extensive studies of the Mg-doped iron oxide material and the short circuited assembly are presented here.

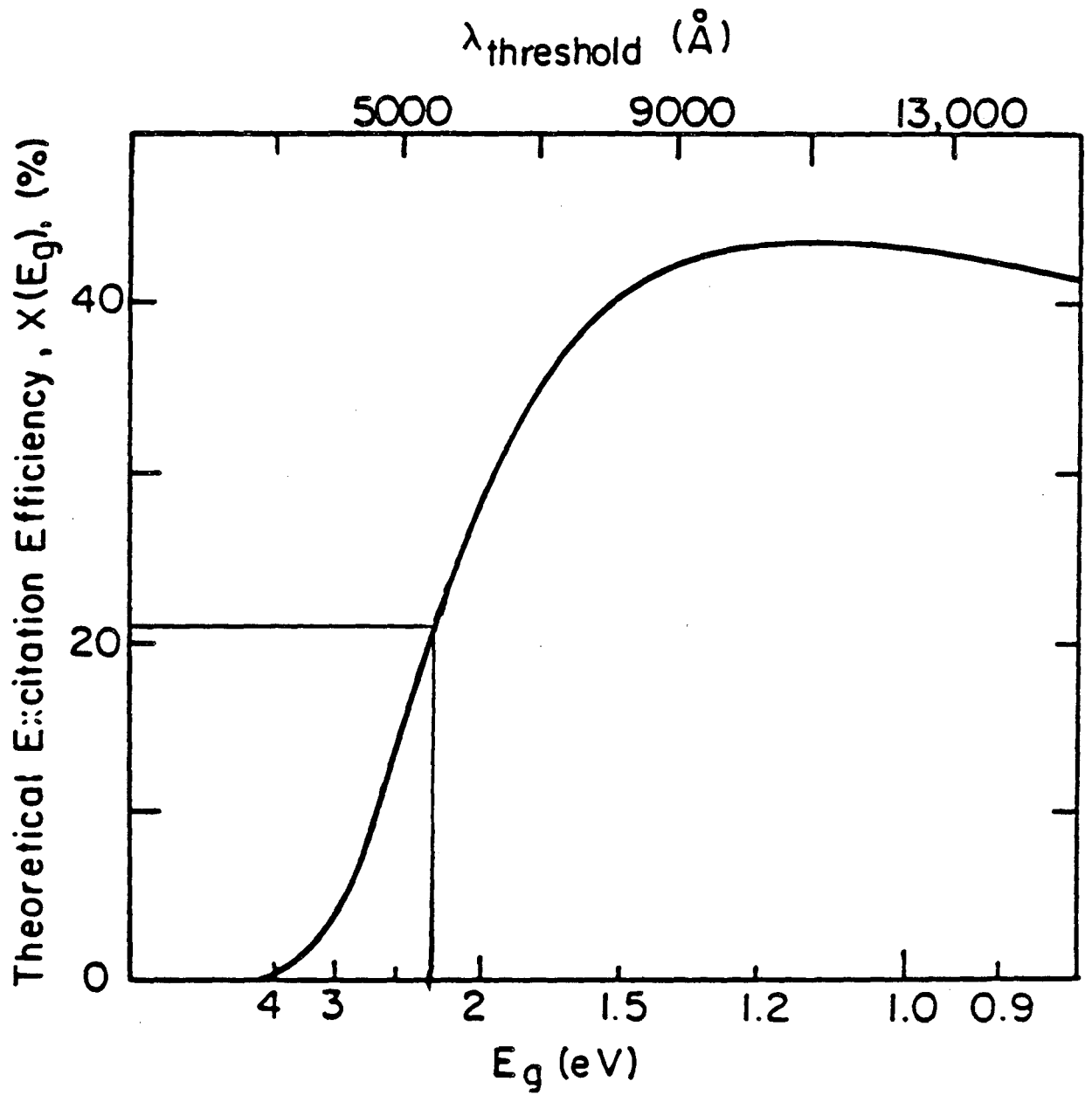
Figure Captions

- Figure 1.1. Spectral intensity from the sun as a function on wavelength. The shaded area represents 40% of the total solar flux density.
- Figure 1.2. Maximum excitation efficiency for a single-threshold quantum absorber as a function of threshold energy (bandgap).
- Figure 1.3. Schematic illustration of a short circuited electrode assembly for the photodissociation of water using doped iron oxides.
- Figure 1.4. Energy level diagram for an operating short circuited iron oxide assembly.
- Figure 1.5. Valence and conduction band edges for several transition metal oxides. Also included are potentials for hydrogen and oxygen evolution.
- Figure 1.6. Band gaps of some oxides and sulfides in relation to spectral flux density of solar radiation.
- Figure 1.7. The basic steps for the reduction of water at a p-type electrode.



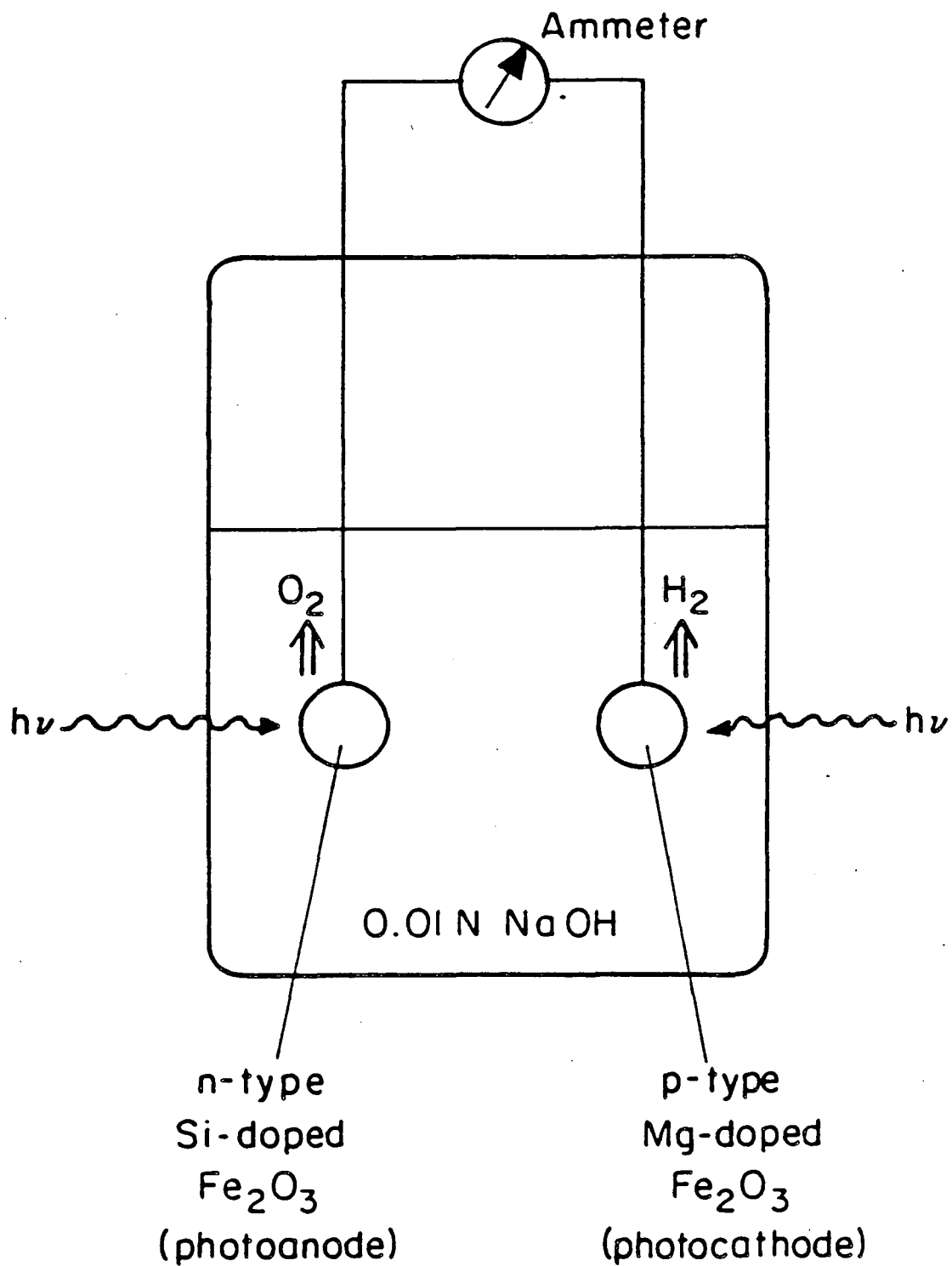
XBL855-6259

Figure 1.1.



XBL 818-6331

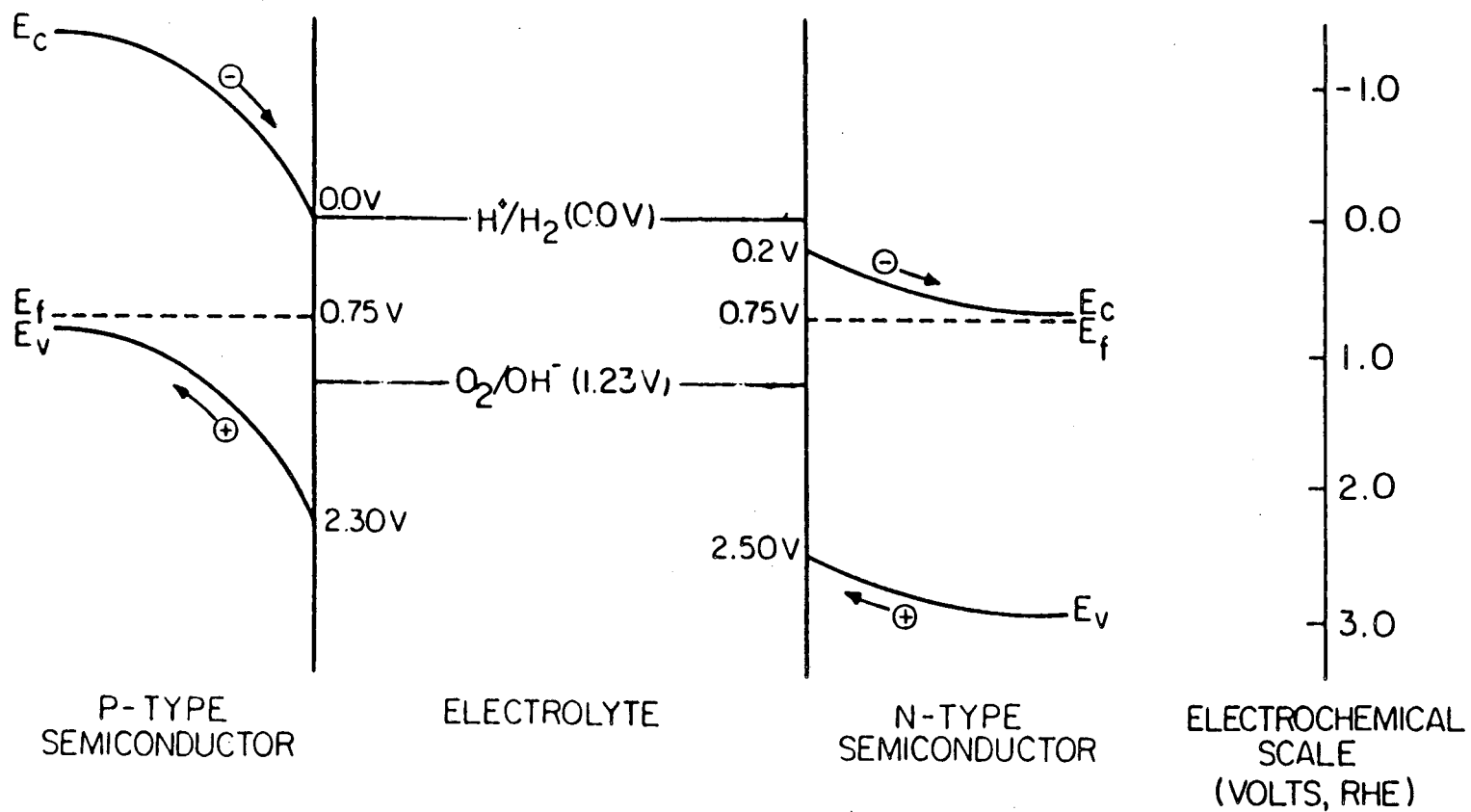
Figure 1.2.



XBL 835-5725

Figure 1.3.

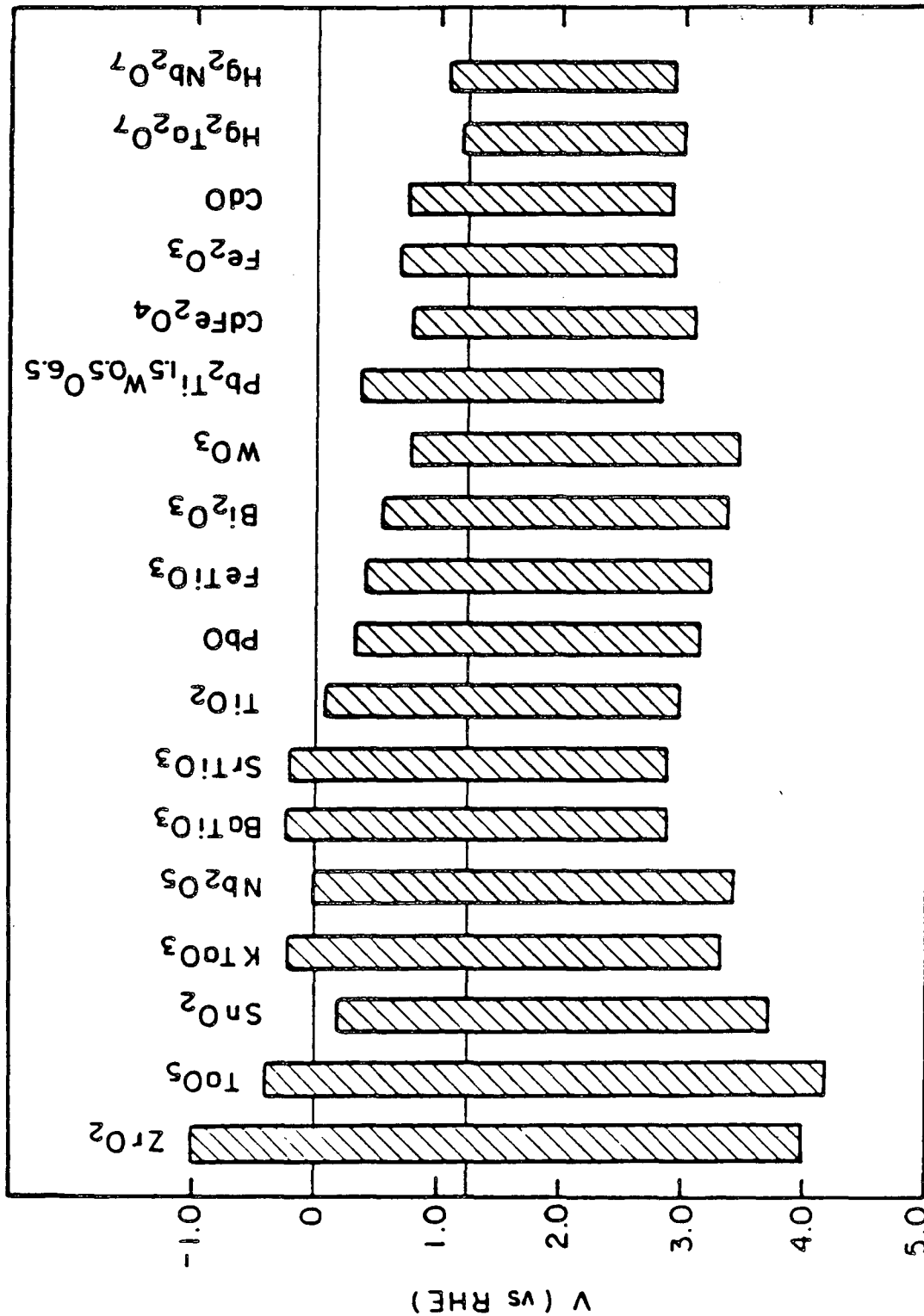
ENERGETICS OF CONNECTED P-TYPE AND N-TYPE IRON OXIDES



XBL 832-5181A

Figure 1.4.

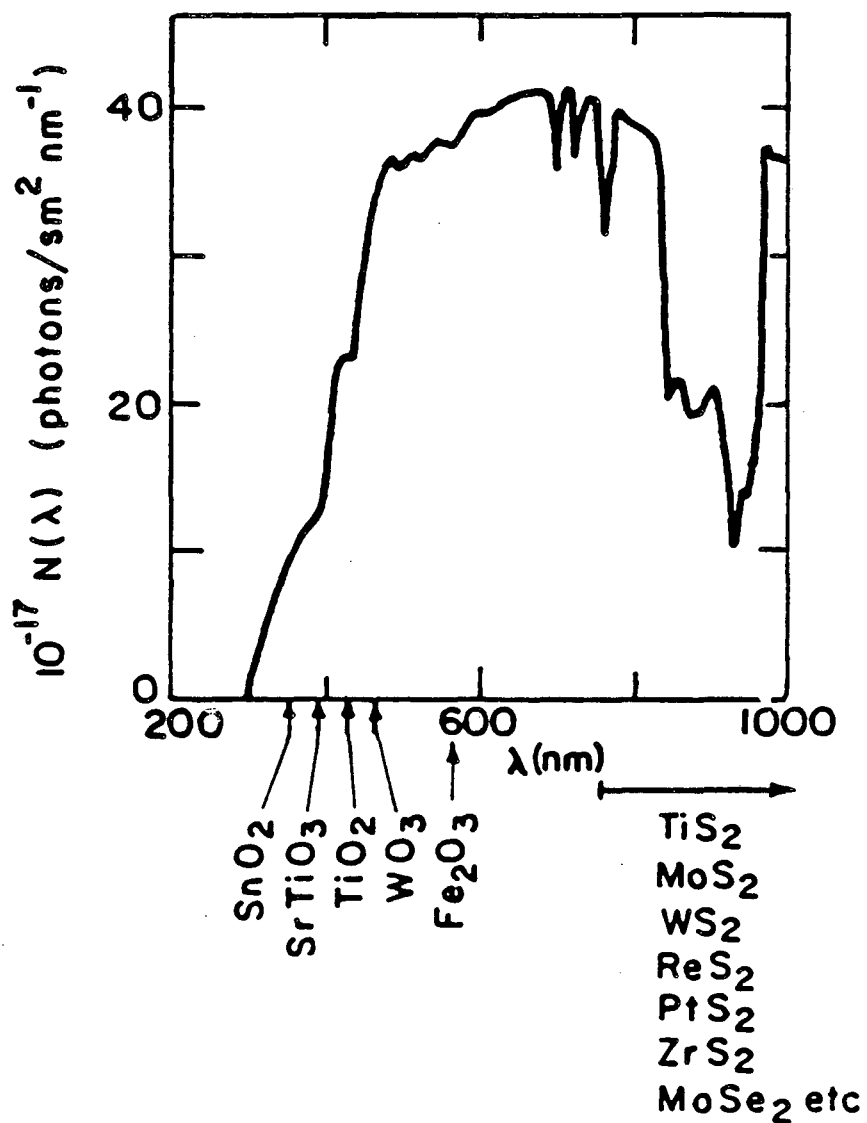
Band Gaps and Flat Band Potentials (uncorrected for PZP)



LBL 855-6267

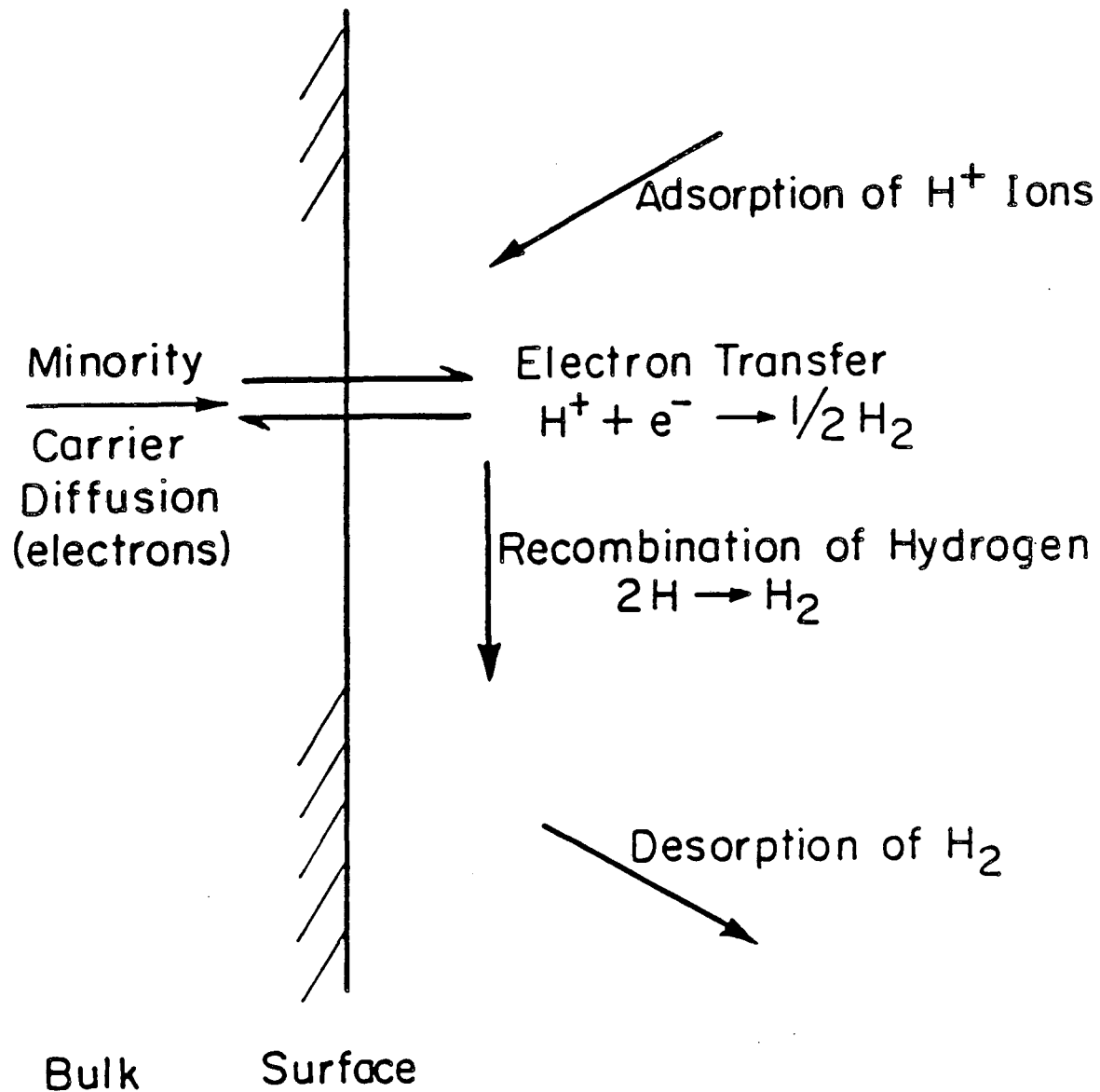
Figure 1.5.

**Band Gaps of Some Oxides and Sulphides
in Relation to Spectral Flux Density of
Solar Radiation**



XBL855-6271

Figure 1.6.

Reduction of H_2 at a p-type Iron Oxide Electrode

XBL 842-6673

Figure 1.7.

References

- 1.1. K.L. Hardee, A.J. Bard, J. Electrochem. Soc., 124, 215 (1977).
- 1.2. D.S. Ginley, M.A. Butler, J. Appl. Phys., 48, 2019 (1972).
- 1.3. M.A. Butler, D.S. Ginley, J. Appl. Phys., 48, 3070 (1977).
- 1.4. I.T. Liou, C.Y. Yang, S.M. Levine, J. Electrochem. Soc., 129, 342 (1982).
- 1.5. H. Yoneyama, H. Sakamoto, H. Tamura, Electrochim. Acta, 20, 341 (1975).
- 1.6. H. Yoneyama, H. Sakamoto, H. Tamura, Electrochim. Acta, 20, 341 (1975).
- 1.7. H. Mettee, J.W. Otvos, M. Calvin, Solar Energy Mater., 4, 443 (1981).
- 1.8. A.J. Nozik, App. Phys. Lett., 30, 567 (1977).
- 1.9. K. Okashi, J. McCann, J. O'M. Bockris, Nature, 266, 610 (1977).
- 1.10 S. Ferrer, G.A. Somorjai, Surf. Sci. 94, 41 (1980).
- 1.11. H. Gerischer, Topics in applied Physics, 31, edited by B.O. Seraphin (Spring-Verlag, Berlin, 1979), p. 115.
- 1.12. M.S. Wrighton, Acc. Chem. Res., 12, 303 (1979).
- 1.13. A. Heller, Acc. Chem. Res., 14, 54 (1980).
- 1.14. A.J. Bard, J. Phys. Chem., 86, 172 (1982).
- 1.15. L.A. Marasak, R. Messier, W.B. White, J. Phys. Chem. Solids, 41, 981 (1980).
- 1.16. C.T. Chen, B.D. Cahan, J. Opt. Soc. Am., 71, 932 (1981).
- 1.17. W.H. Strehlow, E.L. Cook, J. Phys. Chem. Ref. Data 2, 163 (1973).
- 1.18. Kittel, Introduction to Solid State Physics, J. Wiley and

Sons, 1953, p. 276.

- 1.19. W.H. Strehlow, E.L. Cook, J. Phys. Chem. Sol., 24, 1183 (1963).
- 1.20. F.P. Koffyberg, K. Dwight, A. Wold, Sol. St. Comm., 30, 1735 (1979).
- 1.21. K.D. Sieber, C. Sanchez, J.E. Turner, G.A. Somorjai, J. Chem. Soc., Faraday Trans. I, 81, 1263 (1985).
- 1.22. C. Sanchez, M. Hendewerk, K.D. Sieber, G.A. Somorjai, J. Solid State Chem., 61, 3377 (1986).
- 1.23. K.G. McGregor, M. Calvin, J.W. Otvos, J. Appl. Phys., 50, 369 (1979).
- 1.24. P. Iwanski, J.S. Curran, W. Gissler, R. Memming, J. Electrochem. Soc., 128, 2128 (1981).
- 1.25. R. Shinar, J.H. Kennedy, J. Electrochem. Soc., 130, 392 (1983).
- 1.26. J.H. Kennedy, K.W. Frese, Jr., J. Electrochem. Soc., 125, 723 (1978).
- 1.27. K.L. Hardee, A.J. Bard, J. Electrochem. Soc., 124, 215 (1977).
- 1.28. J.S. Curran, W. Gissler, J. Electrochem. Soc., 126, 56 (1979).
- 1.29. S.M. Wilhelm, K.S. Yun, L.W. Ballenger, N. Hackerman, J. Electrochem. Soc., 126, 419 (1979).
- 1.30. R.M. Canda, Electrochim. Acta 26, 1803 (1983).
- 1.31. L.S.R. Yeh, N. Hackerman, J. Electrochem. Soc., 124, 833 (1977).
- 1.32. A.S.N. Murthy, K.S. Reddy, Mat. Res. Bull., 19, 241 (1984).
- 1.33. R. Shinar, J.H. Kennedy, Solar Energy Mater., 6, 323 (1982).
- 1.34. K.L. Hardee, A.J. Bard, J. Electrochem. Soc., 123, 1024 (1976).

- 1.35. R.K. Quinn, R.D. Nasby, R.J. Baughman, Mat. Res. Bull., 11, 1011 (1976).
- 1.36. L.S.R. Yeh, N. Hackerman, J. Electrochem. Soc., 124, 833 (1977).
- 1.37. R. Shinar, J.H. Kennedy, Solar Energy Mat., 67, 323 (1982).
- 1.38. J.E. Turner, M. Hendewerk, G.A. Somorjai, Chem. Phys. Letters, 105, 581 (1984).

Chapter Two

EXPERIMENTAL

Doping of Semiconductor Electrodes (REF 2.1)

Semiconductor Band Structures

The electronic properties of semiconductors are completely determined by the electrons excited into the conduction band and holes left behind in the valence band. In the ground state of a semiconductor at $T = 0$ K, all bands are either completely filled or completely empty, and within the independent electron model, electrons in a completely filled band can carry no current. At $T = 0$ K the lowest unoccupied bands are denoted conduction bands and the highest occupied bands are labelled as the valence bands. Electrons which are excited into the conduction bands can conduct and concomitantly conduction of electron vacancies or holes can occur in the valence band out of which the electrons have been excited. The electrons will be found almost exclusively in levels near the conduction band minima, while the holes will be confined to the neighborhood of the valence band maxima. The conduction bands of α - Fe_2O_3 and Fe_3O_4 are comprised of $\text{Fe}(3d)$ orbitals while the valence bands consist of 90% $\text{O}(2p)$ orbitals with some additional $\text{Fe}(3d)$ contributions. The region between the valence and conduction bands, the bandgap, is unoccupied and is forbidden for occupation by an electron.

Carrier Densities in Thermal Equilibrium

A very important property of any semiconductor at temperature T is the number of electrons per unit volume in the conduction band,

n_c , and the number of holes per unit volume in the valence band, p_v . The values of $n_c(T)$ and $p_v(T)$ depend critically on the presence of impurities. The effect of impurities is to introduce additional levels at energies between the top of the valence band, ϵ_v , and the bottom of the conduction band, ϵ_c without appreciably altering the density of levels in the conduction band, $g_c(\epsilon)$, and $g_v(\epsilon)$. Since conduction is entirely due to electrons in conduction band levels or holes in valence band levels, regardless of the concentration of impurities, the numbers of carriers present at temperature T will be given by

$$n_c(T) = \int_{\epsilon_c}^{\infty} d\epsilon g_c(\epsilon) \frac{1}{e^{(\epsilon - \mu)/k_B T} + 1}$$

$$p_v(T) = \int_{-\infty}^{\epsilon_v} d\epsilon g_v(\epsilon) \frac{1}{e^{(\mu - \epsilon)/k_B T} + 1}.$$

Impurities affect the determination of n_c and p_v only through the value of the chemical potential, μ . It is common practice to refer to the chemical potential of a semiconductor as the Fermi level. Since the chemical potential lies in the energy gap, there is no one electron level whose energy is actually at the Fermi level, in contrast to the case of a metal. Thus the usual definition of the Fermi level (that energy below which the one-electron levels are occupied and above which they are unoccupied in the ground state of a metal) does not specify a unique energy in the case of a semiconductor. Any energy in the gap separates occupied from unoccupied levels at $T = 0$. The term Fermi level should be regarded as a synonym for chemical potential in the context of semiconductors.

Using the case of an intrinsic semiconductor one can derive a

simple equation for the chemical potential of a doped semiconductor

$$\mu = \epsilon_v + 1/2 E_g + 1/2 k_B T \ln\left(\frac{p_v}{n_c}\right).$$

From this equation one can see that for an undoped semiconductor the chemical potential is located midway between the valence and conduction band ($p_v = n_c$) as shown in Figure 2.1A.

Impurity Levels

Impurities that contribute to the carrier density of a semiconductor are called donors if they supply additional electrons to the conduction band, and acceptors if they supply additional holes to (i.e. capture electrons from) the valence band. Most donor impurities are atoms that have a higher valence than the atoms which they are going to replace in the bulk material, while acceptors have a lower chemical valence. In this case Si^{4+} acts as a donor in the iron (Fe^{3+}) oxide lattice, creating an n-type semiconductor, while, ideally, Mg^{2+} acts as an acceptor, for the creation of a p-type semiconductor (REF 2.2). For an n-type material (Si-doped) the additional electron introduced by the impurity should be thought of as being in a superposition of conduction band levels of the pure host material, which is appropriately altered by the additional localized charge $+q$ representing the impurity. The electron can minimize its energy by using only levels near the bottom of the conduction band. Since small energy gaps are generally associated with large dielectric constants, the binding energy of the electron for the impurity atom is very much smaller than the actual ionization potential of the atom. Since this binding energy is measured relative to the energy of the conduction band levels from which the bound impurity level is formed, it can be concluded that

donor impurities introduce additional electronic levels at energies ϵ_d which are lower than the energy ϵ_c at the bottom of the conduction band, by an amount that is small compared with the energy gap E_g (Figure 2.2). Since this energy difference between the donor level and the conduction band is small, the electron is easily excited from the donor level to the conduction band leaving a tightly bound localized vacancy and a "free" electron in the conduction band. This increases the number of carriers in the conduction band relative to the valence band and thus the chemical potential also rises. This is shown schematically in Figure 2.1B for both p-type and n-type semiconductors.

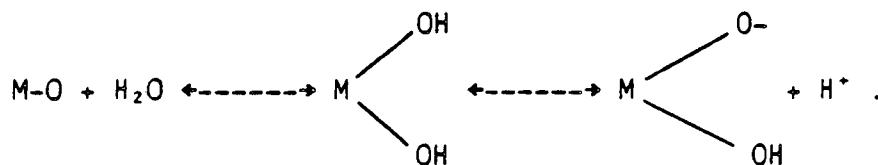
The Space Charge Layer

Once the semiconductor has been immersed in solution and has reached equilibrium the chemical potentials of the two systems must be equal. Using the n-type semiconductor as an example one can see that if the chemical potential of the solution is less than that of the semiconductor, electrons will flow from the semiconductor to the solution via a charge transfer reaction at the electrode/electrolyte interface. The accumulated excess charge forms an electric double layer which has a particular structure depending mainly on the concentration of the mobile and immobile charge carriers at both sides of the interface (Figure 2.1C). It can be shown that the amount of adsorbed ionic charge at the surface depends mainly on the composition of the electrolyte and very little on the excess charge on the semiconductor (REF 2.3,2.4). The position of the valence band edge of an oxide semiconductor in an aqueous solution is generally fixed due to the strong interaction of the O(2p) orbitals

with water, binding protons or hydroxyl groups (REF 2.5). The following equilibria have to be considered.



and



This is an important consideration since with the band edges fixed at a given level with respect to the chemical potential of the solution, only the distribution of electronic charge in the semiconductor varies when a bias is applied to the electrode or when the Fermi level of the semiconductor is otherwise altered.

Depletion Layer Widths

The spatial extent of the space charge layer into the bulk of the material from the surface is very dependent on the charge carrier concentrations (dopant concentrations). The higher the concentration of carriers is per unit volume the narrower the space charge layer will be since the electrons transferred to the solution when creating the depletion layer will be available from very near the surface, whereas with low dopant levels the electrons would have to travel from deeper within the bulk (Figure 2.1C). The width of the depletion layer is given by (REF 2.6)

$$W_d = (2\epsilon\epsilon_0 V_{bb}/qN)^{1/2}$$

and can be determined if the amount of band bending, V_{bb} , and the majority carrier density, N , of the semiconductor are known. ϵ is the dielectric constant for iron oxide (REF 2.7) and the other constants have their usual values: ϵ_0 , the permittivity of free space, and q , the charge on an electron. V_{bb} is the applied potential beyond the flatband potential and is easily determined once the flatband potential has been obtained from a Mott-Schottky plot of measured space charge capacitances. Similarly, the carrier density can be obtained from a Mott-Schottky plot. See Chapter 4 for a detailed explanation of Mott-Schottky measurements and the equations used for the extraction of these parameters.

Materials Preparation

Synthesis of Mg-doped and Si-doped Polycrystalline α -Fe₂O₃

Mg- and Si-doped iron oxide samples were prepared by mixing powders of α -Fe₂O₃ (MCB Manufacturing Chemists, reagent grade) with either SiO₂ (Alfa Products) or MgO (Mallinckrodt, analytical reagent grade), all with a nominal purity of 99.9% or better. The mixed powders were pressed (7000 Kg/cm²) to form pellets 10mm in diameter which were then sintered on a Pt grid under an atmosphere of pure N₂, pure Ar, or air in a vertical tube furnace at 1340-1480°C for at least 20 hours. The discs were rapidly cooled to room temperature in air or in water when removed from the furnace. By sintering the pellets in this temperature region and by subsequent rapid cooling the resistivity of the mixed oxides was lowered.

Single Crystal Growth of Doped Iron Oxides

Single crystals of substituted α -Fe₂O₃ were prepared by

chemical vapor transport using tellurium(IV) tetrachloride as a transport agent (Figure 2.3). Approximately one gram of charge consisting of Fe_2O_3 (MCB reagent) with one mole percent of elemental dopant (Ge, Mg, Nb, Pb, etc.) was placed in a ~5 cm x 13 mm I.D. silica tube along with 20 mg of Te metal. The tube was evacuated to below one micron and backfilled with 400 torr of chlorine gas then sealed. An identical procedure was used to prepare pure Fe_2O_3 crystals for comparison, except that the addition of the dopant to the charge was omitted. The tubes were placed in the zone transport furnace and back transported for 24 hours from 900°C to 800°C. The charge was then transported for 10 days. The temperature of the charge zone during transport was 890°C and that of the growth zone 780°C. After 10 days the furnace was turned off and left to cool to room temperature. The tubes were then removed from the furnace, opened under vacuum, and the product washed with dilute nitric acid, rinsed with water, then dried with acetone. The 6 x 5 x 1 mm platelets shown in Figure 2.4 are examples of the crystals grown using this technique. Most often the platelets had areas of $> 30 \text{ mm}^2$ but were very thin ($< 1 \text{ mm}$ thick). The face of the crystals, as determined by bulk x-ray diffraction and LEED was the (001) basal plane with a hexagonal structure as shown in Figure 5.1.

Characterization

Bulk X-ray Diffraction

Bulk x-ray diffraction analysis served many purposes with both the single crystal iron oxides and the mixed phase polycrystalline samples. Scans of the single crystals, as grown, were used to

determine the crystal face orientation. Subsequently the crystals were crushed and the finely dispersed powder samples analyzed for impurities and for d spacings to obtain the lattice parameters of the corundum structure. This technique was used primarily for phase identification in the polycrystalline samples with some attempts made to quantify the relative amounts of each phase present.

This bulk x-ray powder diffraction analysis was performed on either a Picker or a Siemens model D500 powder diffractometer equipped with a Cu K α radiation source. The detection limit of the apparatus with this technique is approximately one atomic percent.

X-ray powder patterns were taken in the region between 20° and 80° 2 θ . Known standards of commercially available spinels and α -Fe₂O₃ were used in conjunction with the standardized tables (ASTM cards) for positive phase identification. Fast scans were carried out using a scan rate of 6° 2 θ /min for phase identification. Slow scans for lattice parameter determination of the single crystals were carried out using a scan rate of 0.5° 2 θ /min. Lattice parameters were calculated using a least squares refinement technique on a PET Commodore (2001 Series) computer. All cell parameters were calculated using hexagonal indexing, and all crystallite directions are with reference to a hexagonal unit cell (Figure 2.5).

Quantitative estimations of the relative amounts of each phase present were done using the ratio of the integrated step counted intensities of the (220) spinel reflection and the (012) corundum reflection (see Figure 2.6). The integrated intensities were taken

using a step size of $0.1^\circ 2\theta$ at 2 seconds per step. The relative error in the ratio of integrated intensities is estimated to be approximately 20%. The ratios are not corrected for the relative intensities of either phase relative to corundum (Al_2O_3). The absolute error of the ratios is not substantial. There is little difference between the measured intensities, $I(\text{Fe}_3\text{O}_4)/I_{\text{cor}}$ versus $I(\text{Fe}_2\text{O}_3)/I_{\text{cor}}$. However, here, the ratios are used for comparative purposes only.

Scanning Electron Microscopy

The electrode surface morphology was studied with scanning electron microscopy carried out on either an AMR (Model 1000) or an ISI (Model DS130) microscope with surface magnification factors of 1000-5000. In addition, simultaneous elemental analysis was carried out by x-ray analysis via a Kevex probe. The quantitative limit of detection of the probe is about one atomic percent.

Electrical Properties

In the earlier work, resistivities were measured as point to point resistances across the surface of the polycrystalline samples. Later, the electrical properties of both the polycrystalline and single crystal samples were measured using the Van der Pauw (REF 2.8) technique. Contacts to the samples were made using an indium-gallium eutectic and the ohmicity of the contact was verified by repetitive measurement of the resistivity at several different current magnitudes between 10 μA and 100 mA. The variation of the electrical resistivity with temperature was measured using the same techniques except that the ohmic contacts were provided by ultrasonic soldering of pure indium metal. The carrier type of the

material was determined by qualitative measurement of the Seebeck voltage at room temperature. All electrical measurements on the single crystal iron oxides were made in the (001) basal plane.

Magnetic Susceptibility

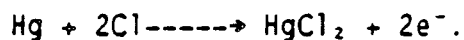
In order to check for spinel phase inclusions magnetic properties of ground single crystal powders were investigated using an S.H.E. Corporation "SQUID" susceptometer. If Fe_3O_4 phase inclusions were present in these materials a constant and large dependence on temperature would be observed. There would be no contribution to the magnetic field dependence from Fe_2O_3 because hematite is antiferromagnetically ordered in the temperature domain (10K-200K) studied. The magnetic susceptibility of the samples was measured at varying field strengths between 5 and 25 kG in the temperature region between 200 K and 10 K to examine the field dependence of the sample susceptibility at various temperatures.

DC Photoelectrochemical Measurements

The electrochemical response of many of these iron oxide electrodes was investigated as a function of applied bias (DC) both in the dark and under illumination. DC photocurrents were measured under potentiodynamic conditions (cyclic voltammetry) or steady state conditions. The apparatus in which these photoelectrochemical experiments were conducted is shown in Figure 2.7. It consists of a standard three electrode electrochemical cell filled with a water solution in which the sample, a Pt counter electrode, and a Mercuric Oxide Luggin capillary reference electrode were immersed. The electrolyte solutions used in the electrochemical cell were aqueous sodium hydroxide and sodium sulfate solutions. The sodium hydroxide

solutions were made by diluting a 10N concentrated NaOH solution (Fisher Scientific Company) with distilled water. Anhydrous sodium sulfate powder (Baker) with a nominal purity of 99.9 percent was used to prepare the 0.1 M Na₂SO₄ solutions.

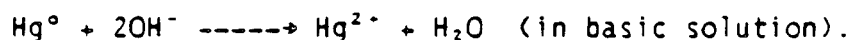
Current-voltage curves obtained in the dark and under illumination were obtained using a Pine RDE 3 potentiostat. The potentiostat applies a given DC voltage to the working electrode (iron oxide sample) with respect to a known reference voltage. The reference voltage is determined by the redox potential of the redox couple for the reference electrode. We have used both a Saturated Calomel Electrode (SCE) and a Mercuric Oxide Electrode (HgO). The redox couple for the saturated calomel electrode is



The redox potential for this reaction is -0.24 V vs. a normal hydrogen electrode (NHE) at pH = 0 (assuming no liquid junction potentials exist between the liquid in the reference electrode and the electrochemical solution in the cell). However, since there is no dependence on the concentration of OH⁻ or H⁺ this potential does not shift with the pH of the solution, i.e.

$$e = e^\circ \quad \text{at all pH's.}$$

The redox couple for the HgO electrode is



The redox potential for this reaction is -0.96 V (again assuming no liquid junction potentials exist between the liquid in the reference electrode and the electrochemical solution in the cell) vs. the normal hydrogen electrode (NHE) i.e. at pH = 0. Now, assuming that this two electron reaction is reversible one can use the Nernst

equation to calculate the redox potential at different pH's.

$$\begin{aligned}\epsilon &= \epsilon^\circ + 0.59/2 \log 1/[\text{OH}^-]^2 \\ &= \epsilon^\circ + 0.592 \log [\text{OH}^-].\end{aligned}$$

From this it is obvious that the reference potential shifts 59 mV per pH unit as is the case for the NHE. Since the hydrogen and oxygen redox potentials in water also shift 59 mV per pH unit, the same I-V curve is obtained in any pH solution when using the HgO reference electrode. This is convenient, since the pH of the solution is then irrelevant and need not be measured. It also eliminates errors due to changes in the pH of solutions used in separate experiments.

To connect the polycrystalline samples to the potentiostat a Kanthal wire was attached to one side of each sample with Ag epoxy. Silicone rubber sealant was used to insulate the wire and the epoxy from the electrolyte solution. Single crystal samples were mounted on a copper plate with an indium-gallium eutectic to provide an ohmic contact and the copper plate attached to a glass covered metallic lead. Again, the entire assembly was insulated with silicone rubber sealant.

Illumination of the sample was accomplished using a 300W or 500W tungsten halogen lamp or a 150W Xenon arc lamp. The light was focused with quartz optics and filtered first through a 5 cm water cell to absorb most of the IR radiation to avoid heating effects, then through a Corning 3-72 visible pass filter to screen the UV radiation with photons of energy ≥ 2.7 eV. After measuring the irradiance with a calibrated Epply thermopile detector and taking into account the absorption of light by the electrolyte solution and the filters, the incoming power of visible light was 37 ± 1 mW.

The electrochemical cell was also equipped with inlet and outlet valves to permit oxygen or other gases to be purged through the solution below the level of the liquid, pass over the sample, and be forced out of the cell from above the solution. Gaseous products were detected by gas chromatography and quadruple mass spectrometry.

For the p/n assembly work p-type and n-type iron oxide samples were connected by means of a Kanthal wire and a microammeter (Figure 2.8) which enabled the measurement of the photoinduced current between the samples in addition to measuring the amount of hydrogen evolved from the p-type iron oxide. These experiments were carried out in the same cell as before but without using the potentiostat. Blank experiments involving only the electrolyte and a sample holder in the cell gave no indication of H₂ production either in the dark or under illumination. A closed circulation loop containing Ar or N₂ passed above the solution for transporting the gases produced from the cell to either a gas chromatograph or to a mass spectrometer. The gas was circulated by means of a mechanical pump fitted with teflon gears.

H₂ produced in the cell was detected using a Hewlett Packard 5720A gas chromatograph fitted with a thermal conductivity detector and a molecular sieve 5A column. Calibration of the gas chromatograph was carried out by injecting small but well defined doses of H₂ and O₂ directly into the cell. The detection limit corresponds to a production rate in the cell of 10⁶ H₂ molecules/hour.

Although the detection limit for O₂ is 15 times higher, measurements of photoinduced O₂ production were more difficult

because of high leak rates (on the order of 10^{17} O₂ molecules/min) into the cell and loop system. In order to combat this problem oxygen was detected in our iron oxide electrode system via the photoproduction of ³⁴O₂ from a 0.01 N NaOH/H₂O electrolyte solution containing 6% isotopically labelled H₂¹⁸O (Alpha Ventron Distributors). Gas samples were collected from the gas circulation loop and analyzed in an UHV chamber by mass spectral analysis.

Depletion Layer Capacitance Measurements

In order to construct a solid state energy level diagram of the operating short circuited iron oxide assembly, depletion layer capacitances were measured as a function of applied voltage. These capacitance measurements were used to determine the energy location of the valence band and conduction band edges to determine the depletion layer widths and carrier densities for each type of our iron oxide semiconductors.

It can be shown that the amount of adsorbed ionic charge at the surface of an electrode in an electrolyte solution depends mainly on the composition of the electrolyte but very little on the excess charge on the semiconductor (REF 2.3,2.4). Consequently, only the distribution of the electronic charge in the semiconductor varies with applied electrode potential and this controls the differential capacitance of the interface. In an ideal depletion layer where electronic equilibrium is fully established during a periodic cycle of the voltage, and in the absence of a charge variation in surface states, the measured capacity depends only on the potential drop in the space-charge layer. The following equations represent the

results for this ideal case (REF 2.9)

$$C(\Delta\phi_{sc}) = \frac{(\epsilon\epsilon_0 qN)}{2}(\Delta\phi_{sc} - kT/q) \quad E.1.$$

$$\Delta\phi_{sc} + \Delta\phi_H = \sqrt{\Delta\phi}. \quad E.2.$$

where $\Delta\phi_{sc}$ is the potential drop in the space-charge layer of the electrode and $\Delta\phi_H$ is the potential drop in the Helmholtz double layer. ϵ_0 is the permittivity of free space, ϵ is the dielectric constant relative to vacuum of iron oxide, q is the charge of an electron, and N is the majority carrier concentration per cubic centimeter.

Equation 1 predicts that a plot of C^{-2} versus $\Delta\phi$ should give a straight line if $\Delta\phi_H$ remains constant. $\Delta\phi$, however, cannot be measured directly between two different phases. Electrode potentials are measured against a reference electrode which means that the sum of two or more electric potential differences is obtained. Since the potential difference between the reference electrode and the electrolyte is kept constant, the measured potential difference V , corresponds to $\Delta\phi$ plus a constant. V is the electrode potential versus the reversible hydrogen electrode.

$$V = \Delta\phi - \Delta\phi_{ref} \quad E.3.$$

Part of $\Delta\phi$ can, however, be measured absolutely if E.1 or another relation between C_{sc} and $\Delta\phi_{sc}$ is valid. For semiconductor electrodes, a situation of particular interest is when $\Delta\phi_{sc} = 0$. In this case, no electric field is present inside the semiconductor and the potential energy of the electrons, which is represented by the position of the band edges, is constant from the bulk up to the surface. This is the flatband situation, and the

corresponding electrode potential is called the flatband potential, V_{fb} .

Combining equations E.1. and E.3. gives the Mott-Schottky relation (REF 2.10,2.11)

$$1/C_s^2 = 2(q\epsilon\epsilon_0 A^2 N)^{-1} (V_a - V_{fb}) \quad E.4.$$

showing that the flatband potential can be determined from capacity measurements if a depletion layer is formed. This implies that no variation of surface charge occurs in the range of the experiment, i.e. that there is no electron flow across the electrode/electrolyte interface.

From these measurements the energy position of band edges in relation to the electrolyte can be obtained. The distance between the band edges and the Fermi level in the bulk of a semiconductor can be derived from the electron or hole concentration at equilibrium conditions, n_c or p_v , if the bandgap and the effective densities of states for the conduction band, N_c , and the valence band, P_v , are known.

As derived in the last section

$$\mu = \epsilon_v + 1/2 E_g + 1/2 k_B T \ln \frac{(p_v)}{n_c} \quad E.5.$$

To connect this relation with the electrode potentials, V , measured versus a reference electrode, one only has to convert electrode potentials into the free energy of electrons at the same electrostatic potential. This is obtained from the equation

$$E_f = -qV + \text{constant}_{ref} \quad E.6.$$

where the constant defines the electron in the reference electrode. For the standard hydrogen electrode, this constant has a value between -4.5 and -4.7 eV (REF 2.12-2.14) (Figure 2.9). The energy

of the Fermi level at the flatband potential is immediately obtained by inserting V_{fb} into E.6. One can then obtain the position of the band edges with E.5., either in terms of Fermi energies, or of the corresponding electrode potentials. The electrode configuration and the apparatus used for the measurements is identical to that used for the three electrode DC photocurrent measurements; a standard three electrode electrochemical cell containing a mercury oxide reference electrode, a platinum counterelectrode, and a doped iron oxide anode or cathode immersed in a 0.01N NaOH solution with the addition of a lock-in amplifier. The surface of the platinum electrode was large so that its contribution to the capacitance was negligible. An AC voltage (amplitude 10mV) with a frequency of 300 Hz $< f < 3$ kHz was superposed on the DC voltage applied to the working electrode from the Pine RDE potentiostat. Depletion layer capacitances were extracted from the phase shift of the AC current out relative to the AC voltage in by use of a PAR model 124A lock-in amplifier. Corrections were included to eliminate phase shifts introduced by the potentiostat and line impedances by rezeroing the phases of the AC and DC voltages at each DC voltage applied. Tests were performed both in the dark and under illumination of 35 mW/cm² intensity focused from a tungsten halogen lamp.

AC Photocurrent Measurements

AC experiments were carried out in order to study the photocurrent response of our samples as a function of the depth of penetration of the light. Illumination from a Xenon arc lamp was passed through an IR filter and a Heath monochromator before being focused with a quartz lens on the sample (Figure 2.10). For AC

measurements using monochromatic radiation a Bulova tuning fork chopper (model 140C) operating at 150 Hz was mounted at the exit slit of the monochromator. The AC photocurrent was detected using a PAR model 124 lock-in amplifier equipped with a model 117 preamp operating in the differential mode. With this method dark currents are eliminated since the tuning fork modulates only the light. Quantum efficiencies were determined by calculating the number of electrons generated in the AC photocurrent per number of photons striking the semiconductor surface. The photon flux was measured by replacing the sample with a calibrated silicon photodiode.

Figure Captions

Figure 2.1. A schematic representation of the location of the chemical potential (A) in an undoped semiconductor, (B) in a heavily doped n-type or p-type semiconductor, (C) in heavily doped semiconductors in equilibrium with a solution, and (D) in a p/n diode assembly.

Figure 2.2. Level density for a semiconductor containing both donor and acceptor impurities. The donor levels are generally close to the bottom of the conduction band compared with E_g , while the acceptor levels are generally close to the top of the valence band.

Figure 2.3. Preparation of iron oxide single crystals by chemical vapor transport. Starting materials on the left are transported in the gas phase to the cold zone on the right. Crystallization of the material occurs as the material condenses out of the gas phase.

Figure 2.4. Photographed Nb-doped iron oxide single crystals platelets.

Figure 2.5. Model of the corundum crystal structure. Relationship of primitive trigonal lattice and its hexagonal coordinates.

Figure 2.6. Bulk x-ray diffraction spectral intensities for powdered α -Fe₂O₃ samples.

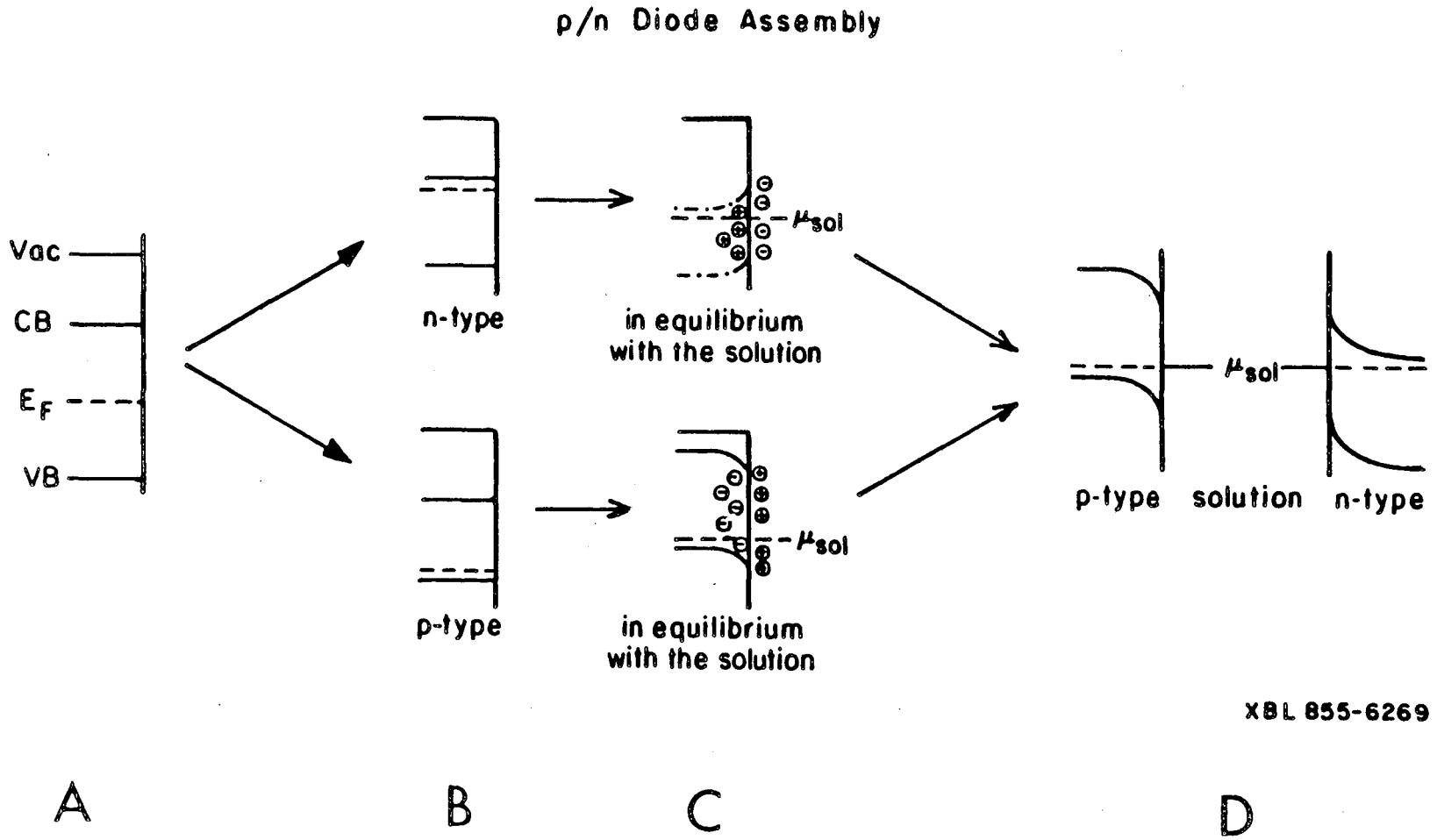
Figure 2.7. Three electrode electrochemical cell for simultaneous DC photocurrent and gas evolution measurements (top view).

Figure 2.8. Apparatus for short circuit assembly photocurrent and gas evolution studies (top view).

Figure 2.9. The relationship between the spectroscopic and electrochemical energy scales.

Figure 2.10. Apparatus for AC photoelectrochemical measurements.

Figure 2.1.



XBL 855-6269

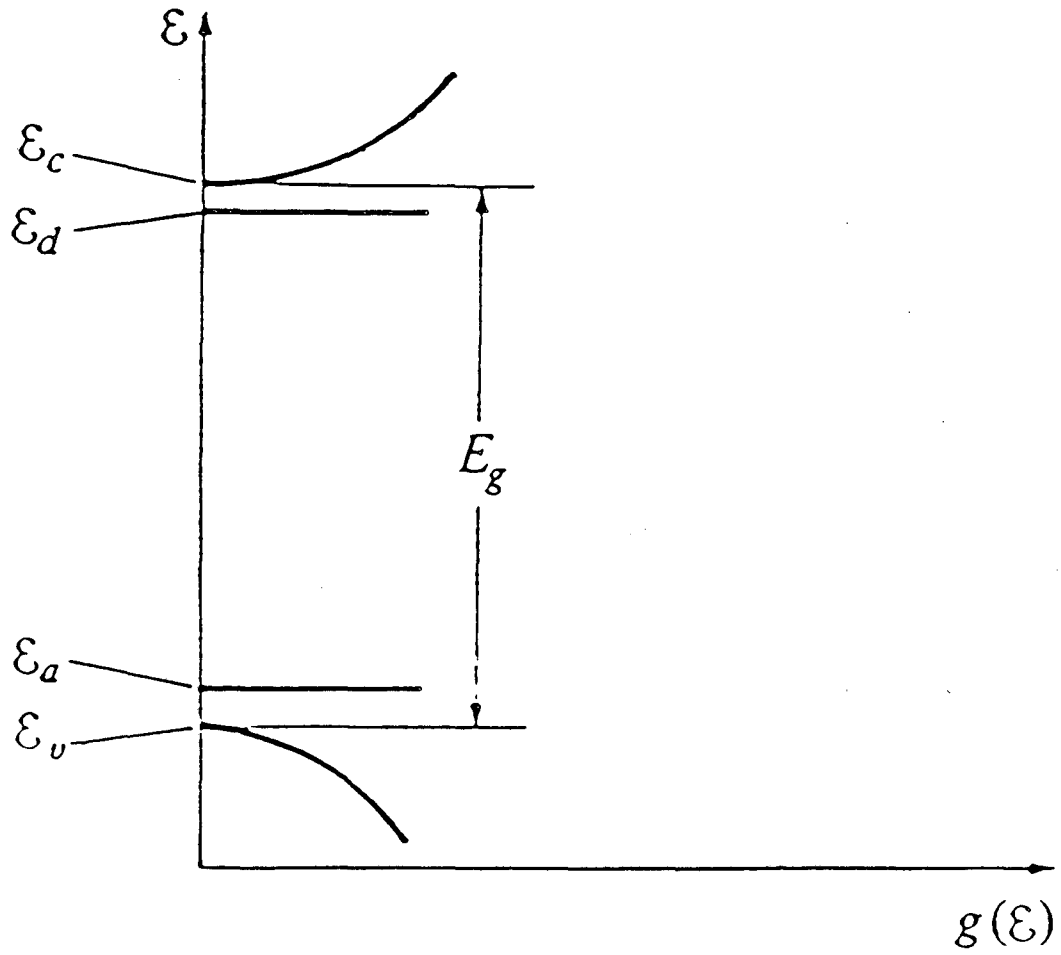
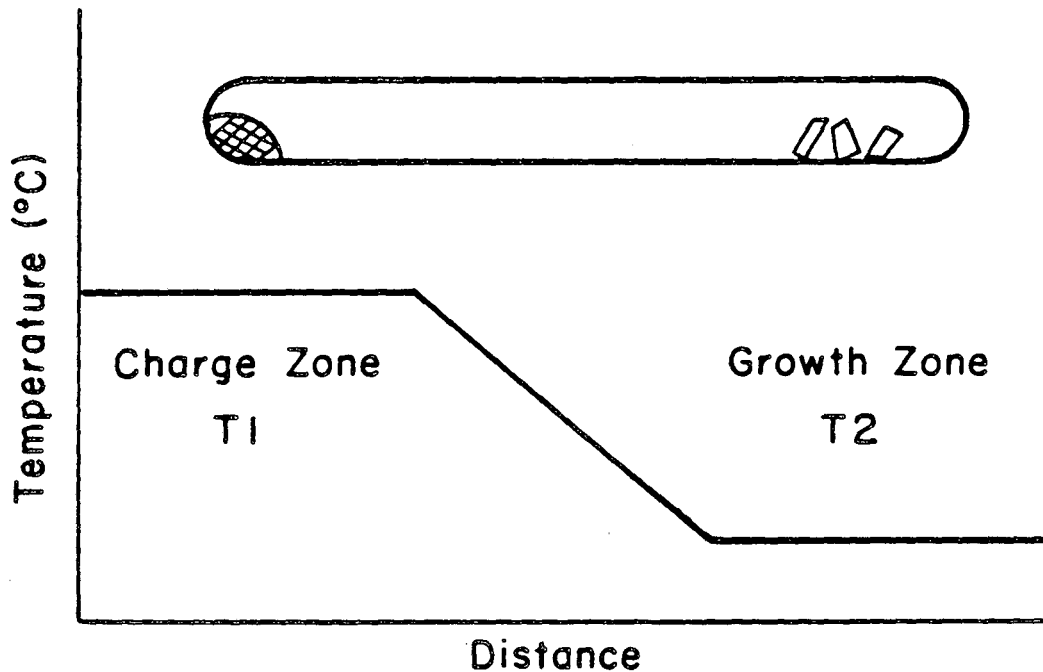


Figure 2.2.

PREPARATION OF IRON OXIDE SINGLE CRYSTALS
BY CHEMICAL VAPOR TRANSPORT REACTIONS



Transport Agent - 2.3 mg TeCl_4/cc

<u>Zone</u>	<u>Temperature</u>	<u>Composition</u>
Charge	885	$\text{Fe}_2\text{O}_3 + 1\% \text{Ge}$
Growth	790	$\text{Fe}_{2-x}\text{Ge}_x\text{O}_3$ $0.05 \leq x \leq 0.10$

Duration: 6 days

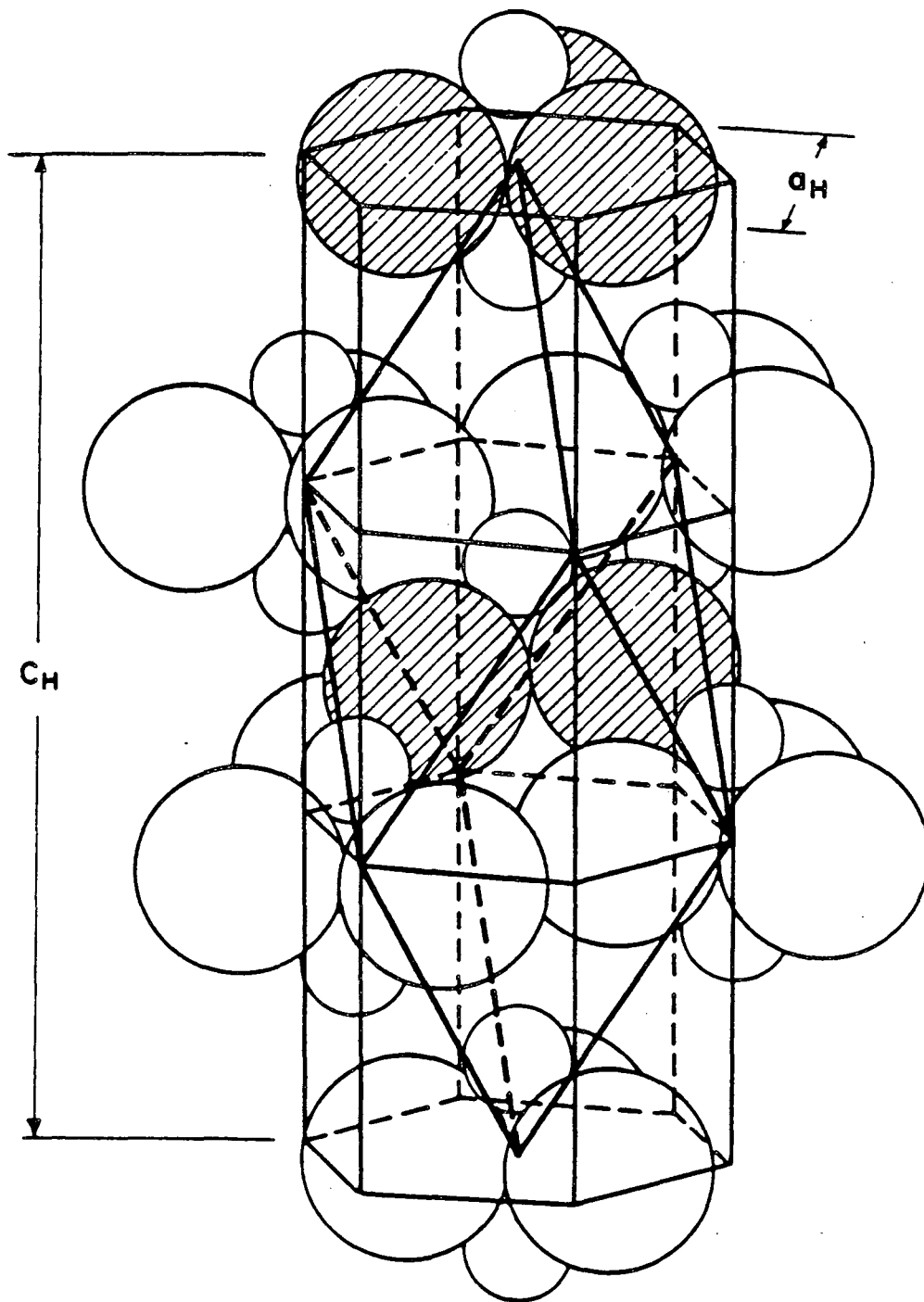
XBL 843-1079

Figure 2.3.



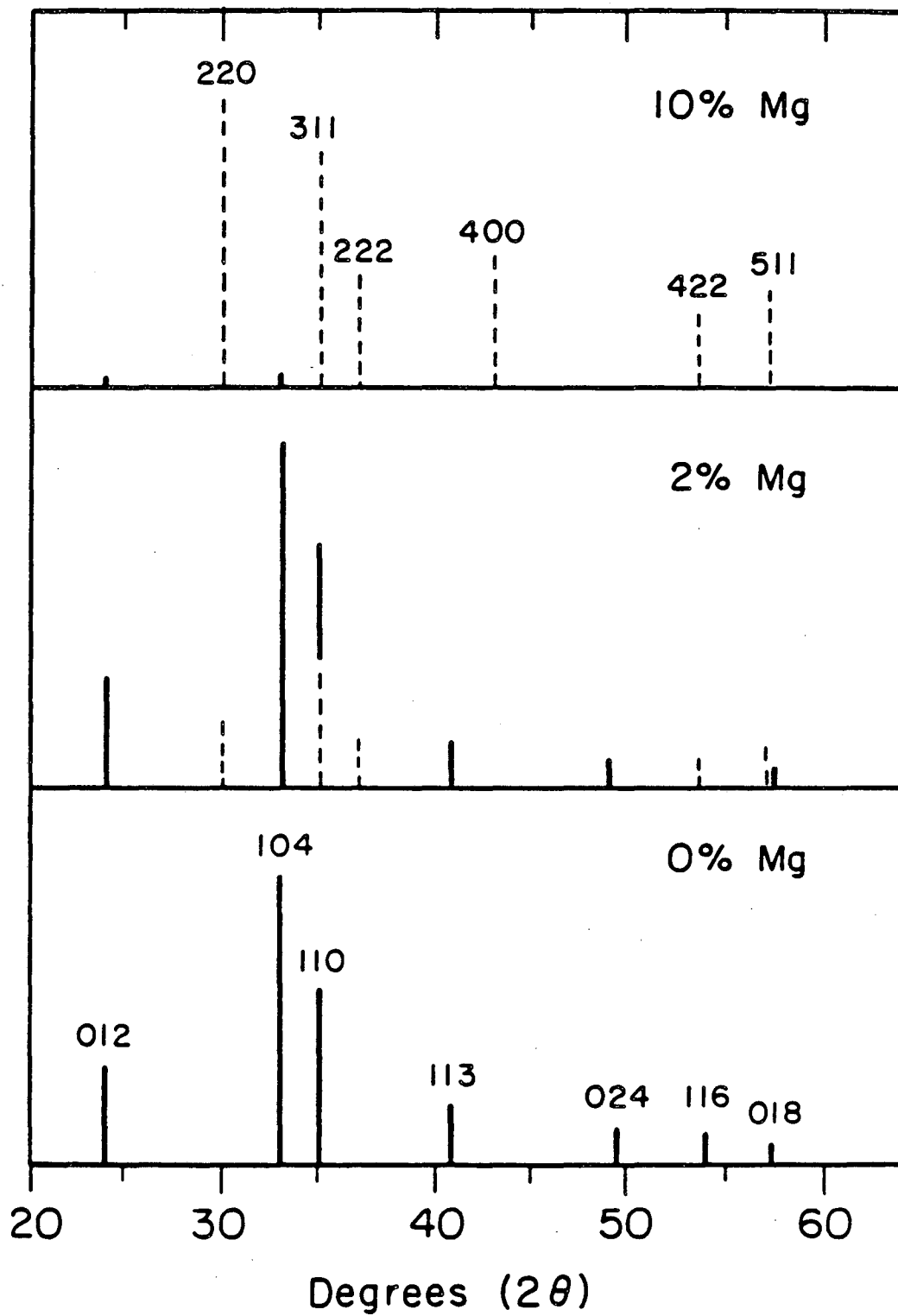
Figure 2.4.

Corundum



XBL 855-6266

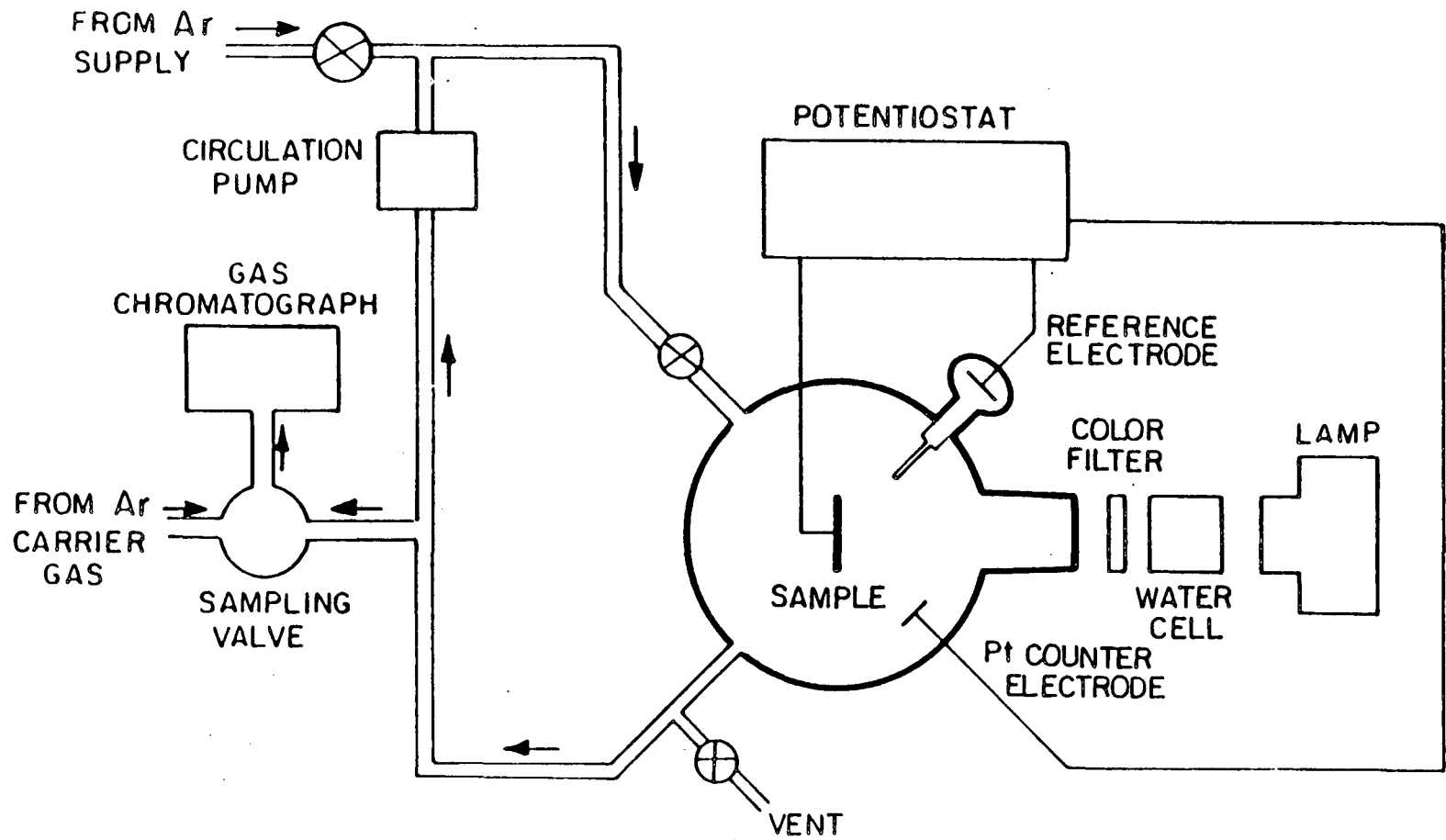
Figure 2.5.



XBL 849-3730

Figure 2.6.

Figure 2.7.



XBL 822-5133A

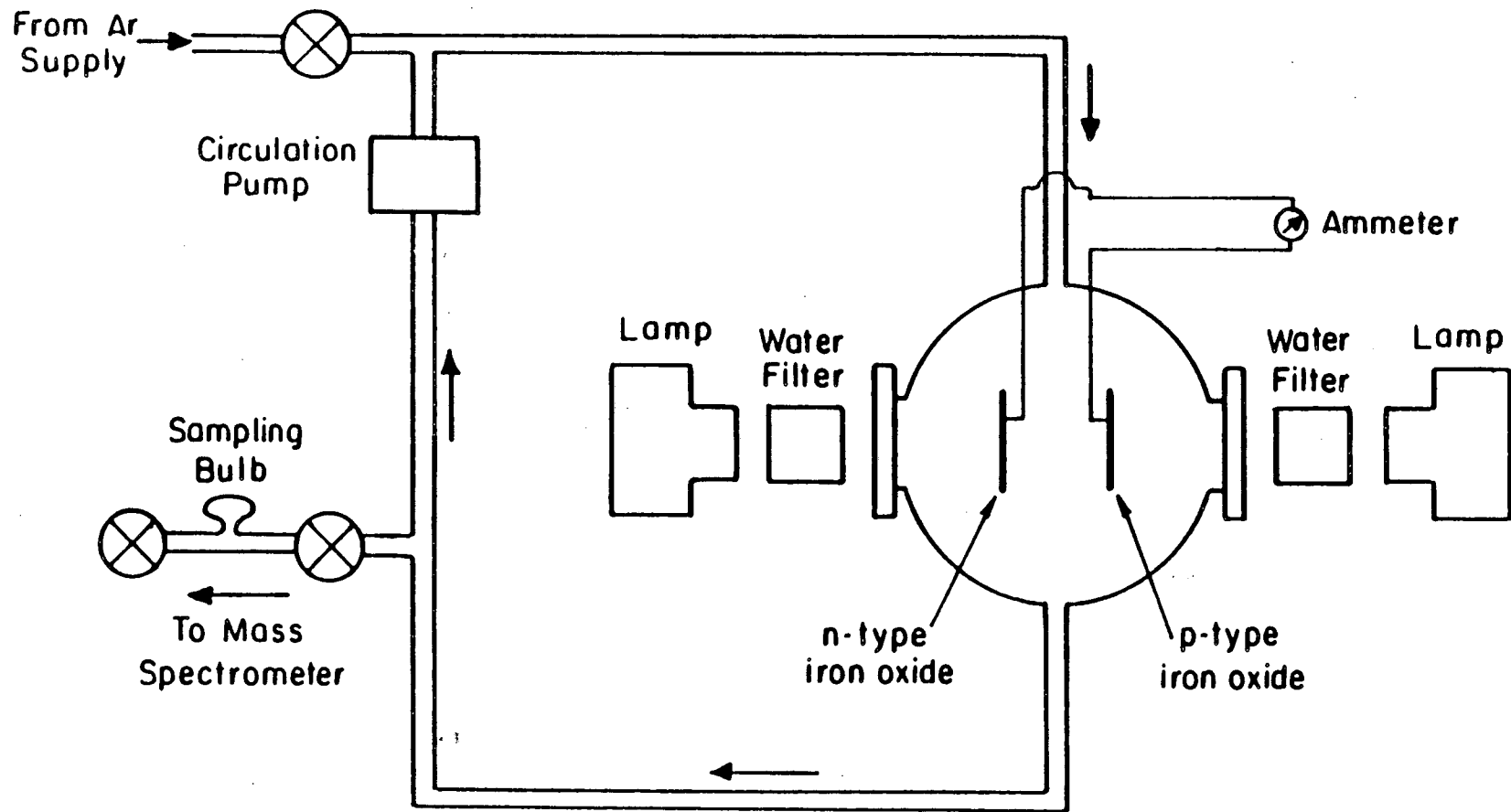


Figure 2.8.

XBL 837-6055

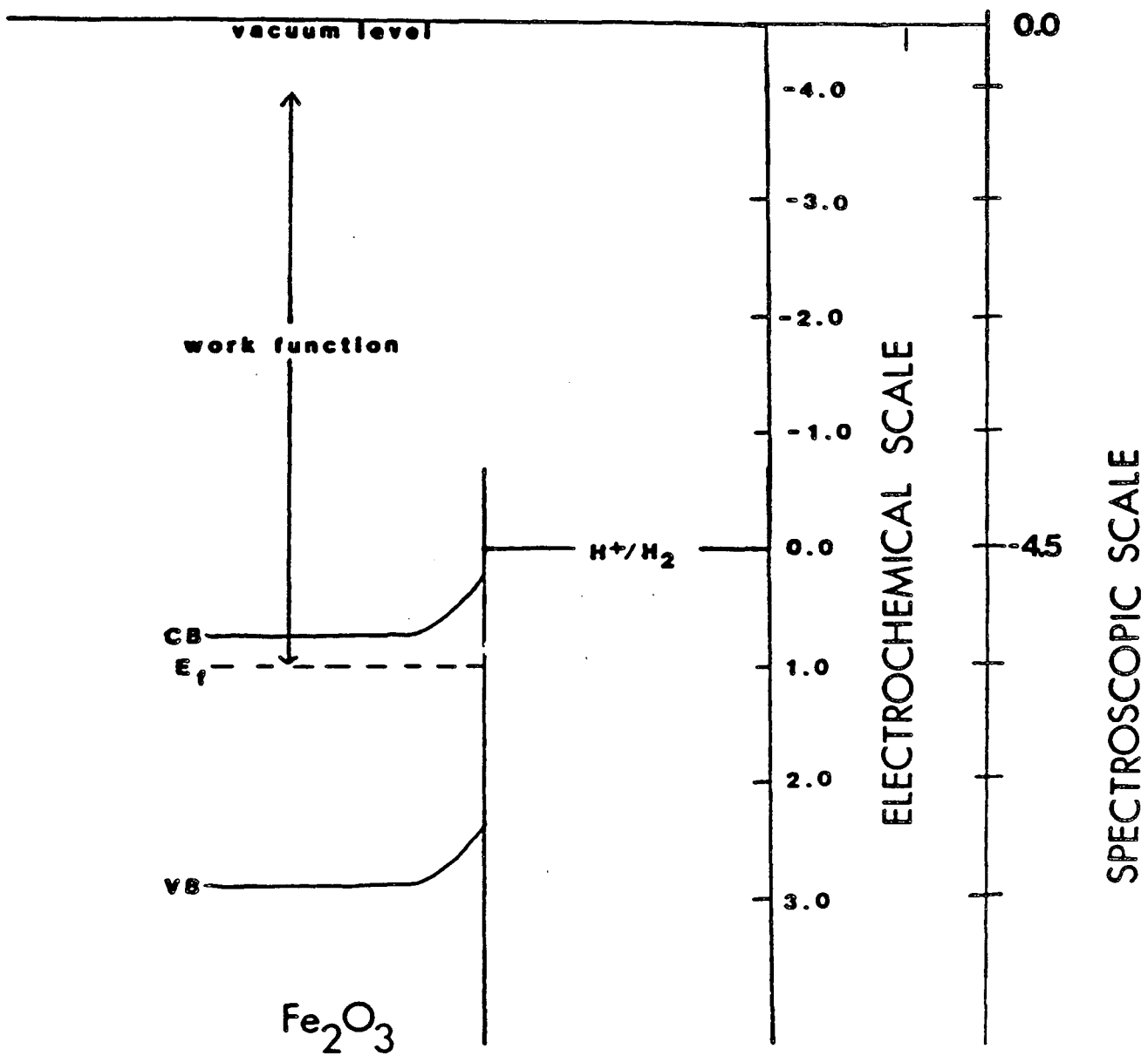


Figure 2.9.

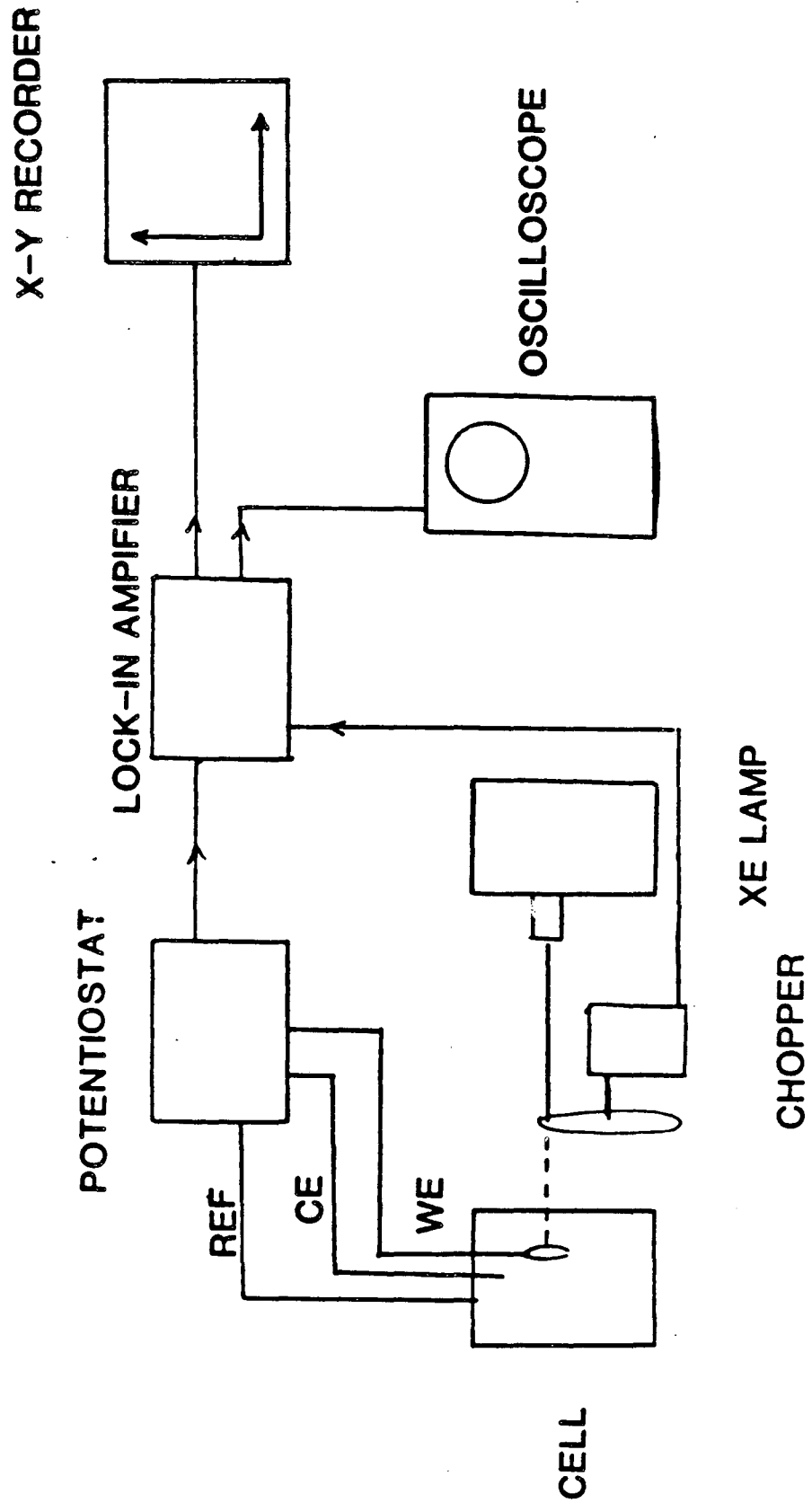


Figure 2.10.

References

- 2.1. N.W. Ashcroft, N.D. Mermin, Solid State Physics, Holt, Rinehart and Winston, 1976.
- 2.2. R.F. Gardner, F. Sweett, D.W. Tanner, J. Phys. Chem. Solids, 24, 1175 (1963).
- 2.3. V.A. Myamlin, Y.V. Pleskov, Electrochemistry of Semiconductors, Plenum, N.Y., 1967.
- 2.4. F. Lohmann, Ber. Bunsenges Phys. Chem., 70, 428 (1966).
- 2.5. D.E. Scaife, Solar Energy, 25, 41 (1980).
- 2.6. M.A. Butler, D.S. Ginley, Chem. Phys. Letters, 47, 319 (1977).
- 2.7. S.M. Wilhelm, K.S. Yun, L.W. Ballenger, N. Hackerman, J. Electrochem. Soc., 126, 419 (1979).
- 2.8. L.J. Van der Pauw, Phillips Res. Rep. 13, 9 (1958).
- 2.9. F. Dewald, Bell Syst. Tech. J., 39, 615 (1960).
- 2.10. N.F. Mott, Proc. Roy. Soc., A171, 27 (1939).
- 2.11. W. Schottky, Z. Phys., 113, 367 (1939); 118, 539 (1942).
- 2.12. F. Lohmann, Ber. Bunsenges. Phys. Chem., 70, 428 (1966).
- 2.13. S. Trasatti, Adv. Electrochem. Electrochem. Eng., 10, 213 (1977).
- 2.14. R. Gomer, G. Tryson, J. Chem. Phys., 66, 4413 (1977).

Chapter Three

Results and Discussion

Polycrystalline Mg-doped and Si-doped α -Fe₂O₃ Iron Oxides

As stated in the introduction, the initial objective of this project was to find a short circuited p/n diode assembly to photodissociate water to form H₂ and O₂ which would operate with no applied external bias and which would utilize light in the visible region of the solar spectrum. This goal was achieved quite rapidly. Sintered discs of Si and Mg doped α -Fe₂O₃ gave measurable photocurrents (Table 1.1) when put in ohmic contact with each other to form a short circuited assembly as shown in Figure 1.2.

The chemical output power of the polycrystalline p/n iron oxide assembly was calculated from the measured photocurrents of our best assembly when illuminated by visible light with energy greater than 2.2 eV. Based on the free energy change when H₂ is produced from H₂O the output power is equal to $(1.23 \times i)\mu\text{W}$ where i is the measured photocurrent in μA . Using $15\mu\text{A}$ as the photocurrent obtained from our best short circuited assembly and an input power of 35mW , a power conversion efficiency of approximately 0.05% was obtained. This would be the power conversion efficiency assuming that all electrons which cross the electrode/electrolyte interface proceed to reduce hydronium ions to H₂ gas molecules, and that there are no other reactions and/or corrosion processes occurring.

With a power conversion efficiency of 0.05% this short circuit assembly would not provide a practical means of converting solar energy to chemical energy, and thus we began our efforts to maximize

the power conversion efficiency by varying a number of parameters in the electrode preparation procedures and the operating conditions of the short circuited assembly.

The Onset Potential for Photocurrent

When considering the feasibility of a working short circuited assembly an important parameter to consider is the onset potential for the production of photocurrent for the isolated electrodes and to relate this to the location of the Fermi level of the operating short circuited assembly. For our purposes the onset potential has been defined as the lowest bias at which a photocurrent of $0.5\mu\text{A}/\text{cm}^2$ is observed.

The onset of photocurrent is directly related to the location of the Fermi level in a semiconductor. For a heavily doped semiconductor the Fermi level of the semiconductor is located approximately 25 mV from the band containing the majority carriers. Thus for a heavily doped n-type semiconductor the Fermi level is located near the conduction band while for a heavily doped p-type semiconductor the Fermi level is located near the valence band. A schematic diagram of the Fermi levels and conduction and valence bands using solid state models are shown in Figure 2.1. The potential bias at which there is no depletion layer i.e. no band bending as shown in Figure 2.1A is known as the flatband potential. When an additional bias is applied (positive for n-type, negative for p-type) which bends the bands and there is no overpotential for the redox reaction, current begins to flow. This is the onset of photocurrent.

When the two electrodes are put in ohmic contact with each other

and immersed in an electrolyte solution the Fermi levels will become equal. This energy level will be the operating potential of the assembly. This operating potential of the short circuited assembly will be some intermediate value of the open circuit Fermi levels of the individual electrodes. The DC photocurrent spectra measured separately for an n-type and a p-type sample are shown in Figure 3.1. If a photoinduced current is to occur between an n-type and a p-type sample in a short circuit configuration without any applied potential, a necessary condition is that the onset potential of the n-type sample be less (more cathodic) than that of the p-type sample so that the operating potential will be located between the onset potentials of the Mg-doped and Si-doped samples as shown in Figure 3.1. This produces the correct electric field gradients to drive electrons and holes to the surface in the cathode and anode, respectively, in order for the reduction/oxidation processes to proceed.

The lowest of the two photocurrents at that potential would determine the maximum current which could pass in the short circuited assembly. Therefore it is an advantage to shift the onset potentials of the Si-doped and Mg-doped electrodes to more negative and positive potentials, respectively, and to obtain the steepest possible rise in photocurrent with increased voltage. We have succeeded in shifting the onset potentials of these materials by controlling the dopant concentrations and with preoxidation treatments.

Table 3.1 displays the onset potential of Si-doped iron oxides in 0.01N and 1N NaOH before and after preoxidation treatment as a

TABLE 3.1

Onset Potential (mV, RHE) for Photocurrent Production of Iron OxideWith Different Atomic Fractions of Si

<u>Si/(Si + Fe)</u> (atom %)	<u>Onset Potential in</u> 1 N NaOH & 0.01 N NaOH (± 25 mV, RHE)	<u>Onset Potential After</u> Preoxidation Treatment (O ₂ purging, 60°C, 1N NaOH) (% 50 mV, RHE)
0	725	650
1	600	500
2	600	450
3	625	475
5	600	450
10	650	575
20	650	600
50	700	-

With Different Atomic Fractions of Mg

<u>Mg/(Mg + Fe)</u> (atom %)	<u>Onset Potential in</u> 0.01 N NaOH (% 50 mV, RHE)	<u>Onset Potential in</u> 0.1 M Na ₂ SO ₄ (% 50 mV, RHE)
1	1000	850
5	950	825
10	950	850
20	725	650

function of the atomic fraction of Si. The onset potential drops from 0.725 ± 0.025 V to 0.600 ± 0.025 V (RHE) upon introduction of 1 atom % Si and stays at this value with increasing Si concentration. Above 20 atom % Si the onset potential rises again. Within the error bars, these results hold true in both 0.01N NaOH and 1N NaOH with a tendency for the onset potential to be slightly less in the 1N NaOH solution.

Preoxidizing the n-type iron oxide surface produced still lower onset potentials. The preoxidation was accomplished by anodic polarization of the sample at potentials above 900 mV (RHE) or by purging the solution with oxygen at temperatures in the range of 60 to 80°C. With both oxidizing pretreatments a decline in onset potential is observed in the range of 100–200 mV for most of the Si-doped iron oxides studied. Thus, the combination of Si-doping and preoxidation of the iron oxide samples decreases the onset potential by 100 to 300 mV as compared to undoped n-type iron oxide.

The beneficial effect of Si-doping on the photoelectrochemical behavior of iron oxide is in agreement with previously reported work on sintered iron oxides prepared in a similar way (REF 3.1). Introduction of 1 atom percent of Si increases the conductivity of the iron oxide by at least three orders of magnitude and also reduces the onset potential for photocurrent production by more than 100 mV. Silicon doping levels higher than 5 atom percent seem to have no significant beneficial effect, which can at least partly be explained by smaller widths of the depletion layer in heavily doped semiconductors. In order to utilize the most advantageous onset potential and maximize the depletion layer width for better electron

hole separation the 2% Si-doped α -Fe₂O₃ was used as the photoanode in our experiments unless otherwise noted.

Table 3.1 also shows the measured onset potentials for photocurrent production from iron oxides with varied concentrations of Mg doping in 0.01N NaOH and in 0.1M Na₂SO₄ solutions. In both solutions the lower Mg dopant levels give the best results with the most cathodic onset potential, while the 20 percent Mg-doped sample exhibits 200-300 mV lower onset potentials. An explanation which is similar to that given for the Si doped electrodes can be given for the dependence of the onset potential on Mg-doping levels, which is least favorable for the highest Mg dopant concentration. The need for high quantum efficiencies and, hence, larger widths of the depletion layer would suggest the use of iron oxides with the lowest possible dopant levels.

In addition to the importance of the onset potentials of the current voltage curves, the magnitude of the photocurrent at the operating potential of the assembly should also be maximized for the greatest power conversion efficiency to be achieved. The photoelectrochemical behavior of n-type Si-doped iron oxide electrodes has been extensively studied. The results reported in the literature (REF 3.2-3.10) are in good agreement with each other and with our observations and therefore these results will not be reported here. These results show that the highest efficiency n-type α -Fe₂O₃ electrodes are those which are doped (particularly with Si). These n-type electrodes show good stability in both basic and acidic solutions (REF 3.11), and give photocurrents on the order of hundreds of mA when in an aqueous

solution and biased against a Pt counter electrode. With this in mind, we have focussed on the Mg-doped material in our short circuited assembly.

The photoactivity of the p-type iron oxide is markedly influenced by various experimental parameters. These include the dopant concentration, sintering temperature, iron oxide surface conditions and electrolyte composition. First, results are presented of photoactivity differences that were obtained by varying the dopant levels of magnesium, altering the sintering temperature during preparation, changing the pH of the electrolytic solution, and subjecting the samples to oxidative conditions. The results are presented in terms of the photocurrents defined as the difference in magnitude of the current obtained under illumination and in the dark. The data are plotted in the figures as current densities ($\mu\text{A}/\text{cm}^2$) against the applied potential voltage with respect to a reversible hydrogen electrode (RHE) (see experimental). Dark currents are not displayed, but they are smaller and within the same order of magnitude as the photocurrents.

The Influence of Sintering Temperature on Mg-Doped Iron Oxide

In a photovoltaic cell, a low resistivity of the working electrode is of crucial importance. High resistivities may be the reason why earlier studies on Mg-doped iron oxide gave no measurable photocurrents (REF 3.12), and have been the stumbling block for many studies on n-type iron oxides. By sintering samples of iron oxide with 5 atomic percent Mg ($\text{Mg}/(\text{Mg} + \text{Fe}) = 5$) at temperatures of 1425-1480°C and rapidly quenching them in water, surface point to point dark resistivities in the range of 10^1 - 10^2 Ωcm were

obtained. When the pellets were cooled to room temperature in air the cooling occurred at a slower rate. Much higher sample resistivities, on the order of 10^3 - 10^5 Ωcm , were obtained (see Table 3.2). The same table shows that sintering the pellets at temperatures of 1350°C or lower resulted in higher resistivities and that the resistivity at a given sintering temperature increased with decreasing doping level. Photocurrents from 5 percent Mg-doped samples, biased against a Pt electrode and sintered at three temperatures, are shown in Figure 3.2. A marked influence of sintering temperature on photocurrent is observed with the photoactivity increasing in the order of $1480^\circ\text{C} < 1350^\circ\text{C} < 1425^\circ\text{C}$. Earlier findings demonstrating that an increase in oxygen deficiency with increasing temperature led to an increase in the conductivity of Fe_2O_3 samples are in qualitative agreement with our study (REF 3.13,3.14).

Sample Morphology and Composition

X-ray diffraction studies of the ground sintered discs of magnesium substituted iron oxides showed the presence of only the hexagonal corundum phase of Fe_2O_3 mixed with a cubic spinel phase. It was found that the transformation from the pure Fe_2O_3 corundum phase to the spinel Fe_3O_4 occurs abruptly at around 1375°C , as reported in the literature (REF 3.15). The abruptness of this transition is consistent with the known intolerance of $\alpha\text{-Fe}_2\text{O}_3$ for non-stoichiometry.

Sample characterization by means of bulk x-ray analysis, SEM and AES show the Si-doped samples to be heterogeneous with two phases. A scanning electron microscopy picture of the surface morphology of

TABLE 3.2

Sample Characterization of Doped Iron Oxides

Sintered 1350°C, Water Quenched to Room Temperature

Sample	Type	Fe ₂ O ₃ Matrix		Precipitates	Resistivity	
		Si+Mg+Fe (atom %)	Si+Mg+Fe (atom %)	Si+Mg+Fe (atom %)	(Ω·cm)	
		atom %				
Si/(Si + Fe) = 1	n	≤ 1	---	80-90	10 ³	
Si/(Si + Fe) = 2	n	1	---	80-90	10 ³	
Si/(Si + Fe) = 10	n	5-6	---	90-100	10 ³ -10 ⁴	
Si/(Si + Fe) = 20	n	7-8	---	90-100	10 ⁴	
Mg/(Mg + Fe) = 1	p	---	≤ 1	---	10 ⁴ -10 ⁵	
Mg/(Mg + Fe) = 10	p	---	6-8	---	10 ³	

a Si doped pellet sintered at 1350°C is shown in Figure 3.3. The Si-doped samples are composed of large grains 20 to 30 μ m in width which are a Si-doped Fe₂O₃ matrix. Along the grain boundaries and on the surface are highly insulating precipitates comprised of mostly SiO₂ as determined by AES (Figure 3.4). The secondary electron absorption was monitored on a screen during the Auger experiment. The grain boundaries were discernible from the matrix due to differences in charging of the SiO₂ and the Fe₂O₃.

Doping with Mg gives quite different results. As shown in the SEM micrograph (Figure 3.5), there are no precipitates on the surface and for the same sintering temperature (1350°C) as the n-type material the grains are smaller by a factor of 5 or more. Although at least 2 structures, spinel and corundum, have been detected by bulk x-ray analysis there is no obvious physical separation of the two phases in the Mg-doped sample as seen by SEM.

A comparison of 5% Mg-doped samples sintered at 1350°C and 1480°C (Figure 3.5) shows that the grains become larger and less faceted at the higher temperature, which can be expected as the material begins to melt. The melting temperature of pure α -Fe₂O₃ is 1594°C (REF 3.16). From simple melting point depression with impurity addition to pure α -Fe₂O₃, one would expect the Mg-doped iron oxides to be near the melting point at 1480°C. There is also a phase change occurring at the higher temperature as is evidenced by bulk x-ray diffraction data. This phase change from the corundum to the spinel crystalline structure is also observable with SEM.

Theoretically, this increase in grain size would decrease the

number of grain boundaries present in the material and concomitantly, electron-hole recombination rates since grain boundaries and other defects in the structure often act as electron hole traps (REF 3.17). If bulk recombination was a rate limiting step for the electrochemical photodissociation of water using these iron oxide electrodes, then the photocurrents should show a rise with an increase in the grain size of the sintered pellets. Our photocurrent measurements show that increasing the sintering temperature by 150° during the preparation of the doped iron oxide discs resulted in significantly higher photocurrents (Figure 3.2). However, since both the grain size and the concentration of Fe_3O_4 increased simultaneously the increased photoeffect cannot be attributed solely to one of these factors.

Composition as a Function of Sintering Temperature and Dopant Concentrations

Not only is the formation of the spinel phase directly related to the sintering temperature, but it can also be controlled by the amount of MgO present in the mixture. When magnesium oxide is sintered together with pure $\alpha\text{-Fe}_2\text{O}_3$ powder the formation of a spinel phase occurs at lower temperatures than when pure $\alpha\text{-Fe}_2\text{O}_3$ is sintered.

Table 3.3 presents the uncorrected integrated intensity ratios of the spinel (220) reflection to the (012) Fe_2O_3 corundum reflection from bulk x-ray diffraction data for four iron oxide pellets containing varying amounts of Mg. The pellets were sintered at 1350°C which is below the temperature at which the spinel phase forms in pure $\alpha\text{-Fe}_2\text{O}_3$ (Figure 3.6). The (220) to (012) ratio

TABLE 3.3

Correlation of Spinel Phase Content and Resistivity
with Varied MgO Concentration in α -Fe₂O₃.

Temperature = 1350°C for 20 Hours

<u>Initial Composition</u> <u>Mole % Mg</u>	<u>I_{spinel}/I_{corundum}</u>	<u>Resistivity (Ωcm)</u> <u>300 K</u>
0.0	0	10 ⁶
2.0	0.4	3600
5.0	0.6	100
10.0	1.0	8

is an indication of the relative concentrations of the spinel and corundum phases in the ceramic discs. It is evident that the addition of magnesium oxide to the iron oxide mixture enhances the formation of the spinel phase at a lower temperature.

Kuczynski (REF 3.18) investigated the mechanism of the formation of $MgFe_2O_4$ from the binary oxides and has suggested that the formation of the spinel occurs by diffusion of cations across grain boundaries. At high temperatures oxygen is lost from Fe_2O_3 and exchange of Fe^{2+} and Mg^{2+} can occur by diffusion, resulting in a spinel phase. Further diffusion of Mg^{2+} will eventually result in the formation of the pure spinel. In the present case, it is likely that even in the initial spinel, $MgFe_2O_4$, further cation exchange takes place so that the solid solution $Fe_{3-x}Mg_xO_4$ is formed. This would explain the large amounts of spinel formed at temperatures below the corundum to spinel transition temperature of Fe_2O_3 in mixtures containing only a small amount of magnesium oxide, (10% or less).

Electrical Properties Governed by Sintering Temperature and Dopant Concentrations

Table 3.3 also presents the room temperature electrical properties of the same ceramic discs. In all cases qualitative Seebeck voltage measurements indicated that the materials were n-type semiconductors, as would be expected from the phases present. Figure 3.7 shows a graph of electrical resistivity versus sintering temperature at constant preparative conditions. A graph of $I_{spinel}/(I_{corundum} + I_{spinel})$ versus temperature for a constant concentration is also plotted on the same axis. There is

an obvious correlation between the amount of spinel present and the electrical resistivity of the samples. An increase in the amount of spinel present lowers the resistivity (REF 3.19).

The evolution of the electrical resistivity with composition, coupled with the carrier type, suggests that electrical conduction in these materials may occur through a percolation of carriers provided by the spinel phase inclusions, because $\alpha\text{-Fe}_2\text{O}_3$ is a high resistivity material while Fe_3O_4 is a semimetal at room temperature (REF 3.20).

Photocurrent Response to Variations in Mg Dopant Levels

Four oxides were prepared and studied under identical conditions except that the atomic percent of magnesium ($\text{Mg}/(\text{Mg} + \text{Fe})$) was altered between 1, 5, 10 and 20 percent. The effect of these different Mg-doping levels on the photocurrent response of the samples is illustrated in Figure 3.8 for 0.01N NaOH and in Figure 3.9 for 0.1M Na_2SO_4 . In both solutions the higher doping levels (10-20 atom percent) result in higher p-type photocurrents at more cathodic applied potentials. This increase can probably be attributed at least in part to lower resistivities with increased Mg-doping levels.

Photocurrents measured in an 0.01N NaOH electrolyte solution are shown in Figure 3.8. The samples doped with 5 and 10 percent Mg have an onset potential of 950 ± 50 mV vs. RHE and exhibit photocurrents which increase monotonically with a more cathodic applied potential. The 20 percent doped oxide has an onset potential approximately 125 mV more negative than for samples with 5 and 10 percent doping levels but the photocurrent rises steeply so

that 5, 10, and 20 percent doping levels differ only slightly once very cathodic potentials are reached (100–200 mV vs RHE). The photocurrents when only 1 percent magnesium doping was used are quite low and correspondingly the resistivity of the sample was quite high. The same study carried out in a 0.1 M Na_2SO_4 solution (Figure 3.9) yielded qualitatively identical results although the magnitudes of the current densities were somewhat higher.

As seen in Figures 3.8 and 3.9, the onset potential for p-type photocurrent production is higher (more anodic), the lower the Mg doping levels are (see Table 3.1). Traditionally, this behavior is qualitatively explained by the variation of the width of the space charge region which decreases with increasing doping level. Because we have no direct proof of Mg substitution into the iron oxide lattice it is difficult to interpret these results using this argument based on doping. However, the increase in the semimetal, Fe_3O_4 , concentration as described earlier would also decrease the depletion layer width.

The Effect of Oxygen Purging of the Electrolyte Solution on the Photocurrent.

It was observed that purging the electrolyte with oxygen gas increases the photocurrents and the dark currents of the p-type iron oxide samples. The effect of oxygen purging for 5 minutes is seen in Figure 3.10 for the same Mg-doped iron oxide discs as shown in Figure 3.2. Before oxygen purging there is a wide variation in the photocurrents of samples sintered at the three different temperatures of 1350°C, 1425°C, and 1480°C. After oxygen purging

the photocurrents are higher in magnitude and the photoactivity of all three samples appears to be very similar. Although the photocurrent of the 1350°C sintered sample after oxygen purging is slightly lower than the photocurrents of the samples sintered at 1425°C and 1480°C, it should be noted that the surface resistivities of the 1425°C and 1480°C sintered samples were the same (50 Ωcm) within experimental accuracy, while that of the 1350°C sintered sample was higher (5000 Ωcm).

pH Dependence of the Photocurrents.

Figure 3.11 depicts the results of measurements taken from a single p-type iron oxide sample in electrolytic solutions of 1N, 10^{-2}N and 10^{-4}N NaOH. The largest photocurrents were obtained in the 10^{-2}N solution with slightly lower values in the 1N solution. The photoactivity in 10^{-4}N NaOH was low and relatively constant even when extensively polarized.

While n-type iron oxide (REF 3.21) and SrTiO_3 (REF 3.22) show a monotonic increase in photoactivity with the pH of the NaOH solutions the pH dependence of the photoactivity for p-type iron oxide is different. As illustrated in Figure 3.11 the photocurrent for the same Mg-doped sample was highest in 0.01 N NaOH and significantly lower in less basic and in more basic NaOH solutions. Assuming simple H^+/OH^- equilibria at the iron oxide surface the pH of the solution should have no effect on band bending or other thermodynamic criteria required for efficient photoelectrolysis of water. This has been verified on a number of oxide photoanodes (REF 3.23). The strong pH dependence on the photoactivity of n-type SrTiO_3 has been suggested to be due to the involvement of hydroxide

ions in a rate-limiting step, such as the formation of surface hydroxyl groups, which act as hole acceptors and thereby decrease the probability of electron-hole recombination (REF 3.24). Similar arguments on p-type photocathodes would imply that a larger surface concentration of hydrogen ions acting as electron acceptors could also decrease the probability of electron-hole recombination. The higher resistivity of the lower pH solution may be why significantly lower photocurrents were observed in the 10^{-4} N NaOH solution.

Stability of the Photocurrents of the Mg-doped Iron Oxide Samples

The stability of the electrodes is a rather controversial and complicated topic to address. Mixed and inconsistent results have been obtained depending on the conditions under which the electrodes were tested. During prolonged cathodic polarization on the order of 10 hours, the photocurrents of Mg-doped samples showed no measurable alteration. Visual inspection of the iron oxide cathodes after the electrochemical measurements in the aqueous solutions of different pH in the range of 6 to 14 showed no signs of corrosion. In fact, the photocurrents of a 5 atom percent Mg-doped sample polarized at 600 mV (RHE) in the 0.01N NaOH solution increased over an 8 hour period by 50 percent (Figure 3.12) and in the 0.1 M Na_2SO_4 solution by 30 percent during the same time span.

The stability of these Mg-doped electrodes was also examined while cycling the potential bias on the electrode between +400 V and -900 V vs. an HgO electrode. Subjected to these conditions, the Mg-doped samples do not show strong stability. Figure 3.13 provides an example of the evolution of a typical cyclic voltammogram obtained by cycling a Mg-doped iron oxide electrode for several

days. After several days of cycling the dark currents decreased and the photoeffect disappeared. This result coupled with the gradual increase in photocurrents observed under cathodic bias are understandable in view of the preparative conditions for producing the pellets. From the bulk x-ray diffraction data, it is evident that the $\alpha\text{-Fe}_2\text{O}_3$ is reduced during the sintering at high temperature and that the rapid quenching of the pellets in water upon removal from the furnace "freezes" in the oxygen deficiencies. From the cyclic voltammograms, it appears that under anodic polarization the electrodes are irreversibly oxidized, while under cathodic bias the electrode reduction is enhanced. A second observation of the cyclic voltammograms is also worthy of discussion, and that is the presence of large dark currents in the cathodic region of the I-V curve. Whereas photoelectrochemical measurements gave very low dark currents (below $10 \mu\text{A}/\text{cm}^2$ at the highest potentials investigated) for Si-doped iron oxides, corresponding measurements on Mg-doped iron oxides showed much higher dark currents, around $100 \mu\text{A}/\text{cm}^2$ at the lowest potentials investigated.

A typical I-V curve for a good p-type electrode exhibiting diode characteristics is shown in Figure 3.14. The dark current is essentially zero in the anodic region until at very positive bias the diode breaks down and oxygen is evolved in the dark. Contrastingly, in the cathodic region even with large positive voltages applied to the cathode no currents are observed. Under illumination, the results are just the opposite with the photocurrents being observed in the cathodic region and no currents

being passed in the anodic region.

A comparison of the cyclic voltammogram taken from one of the polycrystalline Mg-doped iron oxides (Figure 3.13) with the diode voltammogram shows an obvious contrast. The dark currents from the polycrystalline discs are reminiscent of an n-type rather than a p-type diode, yet photocurrents are also generated in the cathodically biased region. Normally, such behavior in the dark would be considered indicative of a corrosion reaction on a cathode. However, since the Mg-doped discs are inhomogeneous multiphase materials consisting primarily of n-type $\alpha\text{-Fe}_2\text{O}_3$, it may be possible to rationalize the presence of cathodic dark currents and the apparent lack of corrosion using alternative arguments. The inhomogeneity of the material would allow for grains of doped or reduced iron oxide which exhibit cathode behavior to coexist with the primarily n-type bulk of $\alpha\text{-Fe}_2\text{O}_3$. This mixture would allow for both n-type and p-type dark and photocurrents to be observed and would also explain why the observed currents vary from sample to sample.

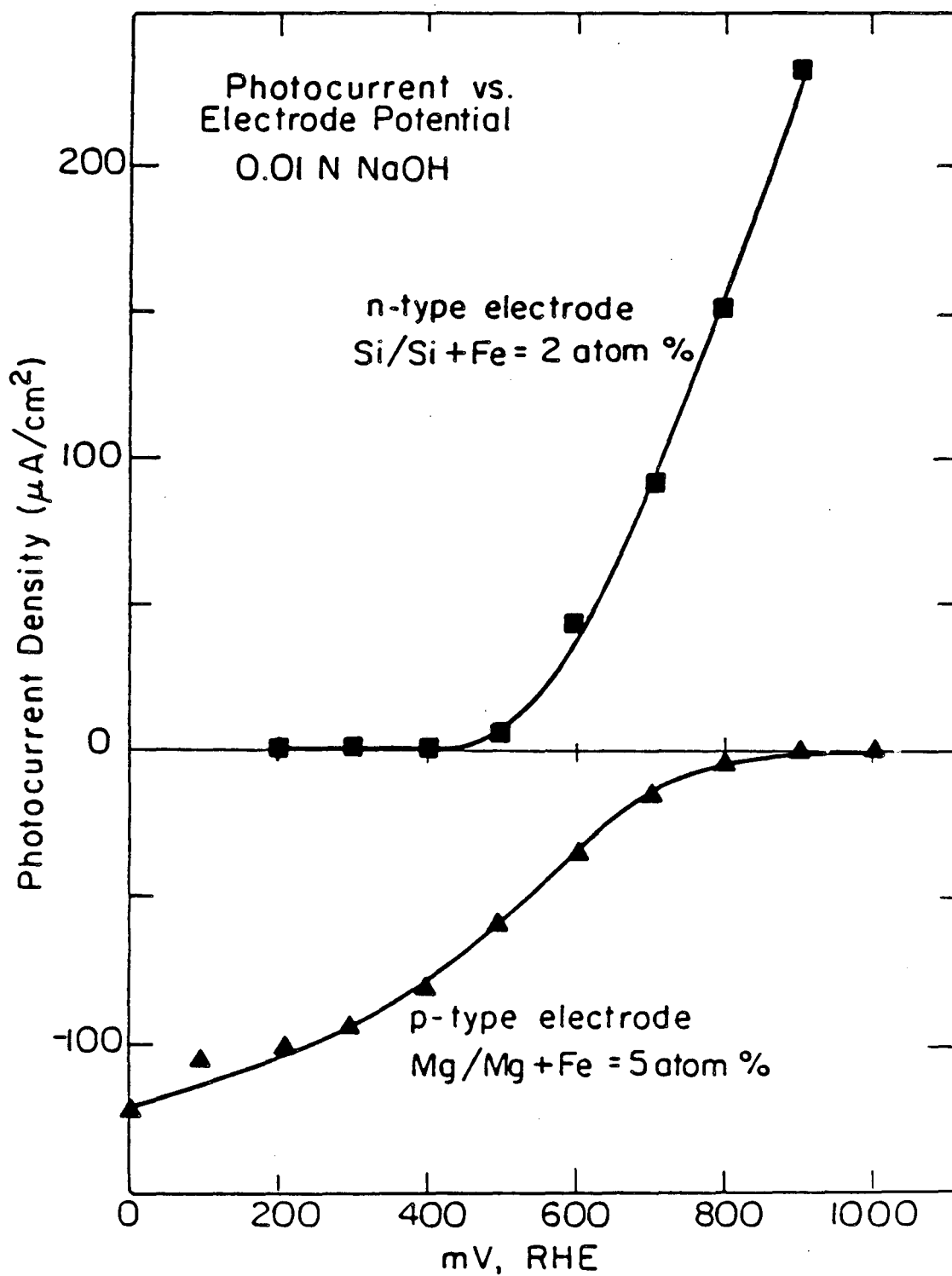
From these results and arguments it is evident that these polycrystalline Mg-doped iron oxide pellets are not true p-type diodes. Nonetheless, they do act as cathodes under biased conditions and function as a photocathode for the production of H_2 in a short circuited assembly with an n-type Si-doped iron oxide anode. Operation of the short circuited assembly can be maintained with as much as 20 μA of photocurrent for long periods of time. The lack of corrosion of these materials is consistent with reports by other workers (REF 3.11).

In the past transition metal catalysts such as Pt have been deposited on other materials (InP) (REF 3.25). SrTiO₃ (REF 3.26) to aid the progress of electrochemical reactions. It is believed that Pt aids hydrogen atom recombination and facilitates the desorption of H₂ from surfaces. Pt also reduces the recombination rate of electrons and holes by the formation of an accumulation layer in the semiconductor at the metal interface and therefore accelerates the H⁺ reduction reaction in addition to the H atom recombination catalysis (REF 3.27). We have deposited Pt in submonolayer amounts and to thicknesses > 20 nm on the iron oxides but only small beneficial effects were observed (~20% increases in photocurrents) as shown in Figure 3.15. In fact, when Pt was deposited in the form of a grid over the p-type iron oxide surface the photocurrent and the hydrogen production rate deteriorated. Presumably Pt blocked the active sites on the surface.

Figure Captions

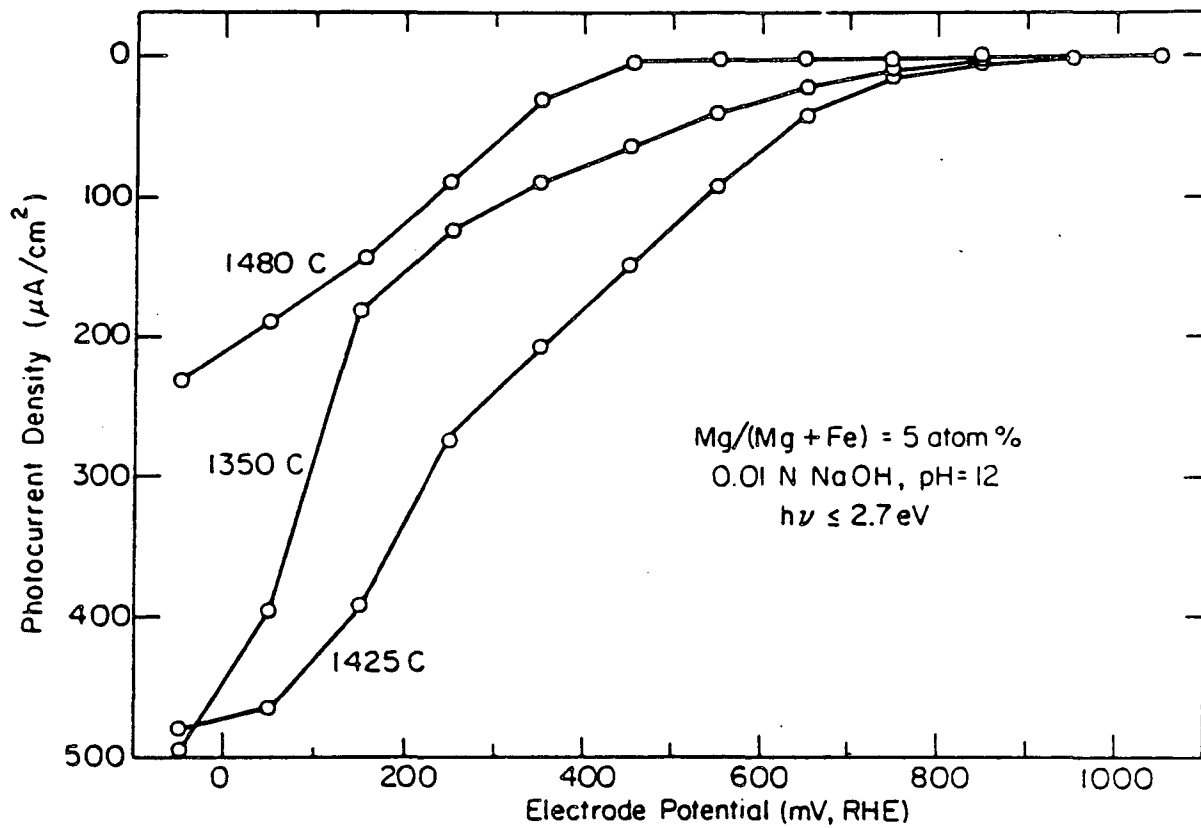
- Figure 3.1. Photocurrent vs. applied voltage for Si-doped and Mg-doped electrodes against a Pt counterelectrode.
- Figure 3.2. DC photocurrents from Mg-doped iron oxide electrodes sintered at 1350°C, 1425°C, and 1480°C.
- Figure 3.3. Scanning electron microscopy photographs of n-type Si-doped iron oxide (left) and Mg-doped iron oxide (right). The dopant levels are $\text{Si}/(\text{Si} + \text{Fe}) = 2$ atom percent and $\text{Mg}/(\text{Mg} + \text{Fe}) = 1$ atom percent.
- Figure 3.4. Auger electron spectra of Si-doped iron oxide comparing the Si rich grain boundaries and the iron oxide matrix as seen in Figure 3.3 (left).
- Figure 3.5. Scanning electron microscopy photographs of sintered and water quenched p-type iron oxide with $\text{Mg}/(\text{Mg} + \text{Fe}) = 5$ atom percent. Sintering temperatures 1350°C (left) and 1480°C (right).
- Figure 3.6. Iron-oxygen phase diagram.
- Figure 3.7. Electrical resistivity vs. sintering temperature and spinel concentration for Mg-doped electrodes.

- Figure 3.8. Photocurrent density as a function of electrode potential for various Mg-doped iron oxides in 0.01 N NaOH.
- Figure 3.9. Photocurrent density as a function of electrode potential for various Mg-doped iron oxides in 0.1 M Na₂SO₄.
- Figure 3.10. Photocurrent density after oxygen purging of a 0.01 N NaOH solution for various sintering temperatures. Mg/(Mg + Fe) = 5 atom percent.
- Figure 3.11. Photocurrent density as a function of electrode potential for various concentrations of NaOH solutions. Mg/(Mg + Fe) = 5 atom percent.
- Figure 3.12. DC currents with chopped light as a function of time from a Mg-doped iron oxide electrodes.
- Figure 3.13. Typical cycled voltammetric curves obtained from a Mg-doped iron oxide electrode.
- Figure 3.14. Perfect example of a cyclic voltammogram obtained from a pure p-type diode.
- Figure 3.15. Observed DC photocurrents from Mg-doped iron oxide electrodes with and without Pt deposited on the surface.



XBL 832-5322

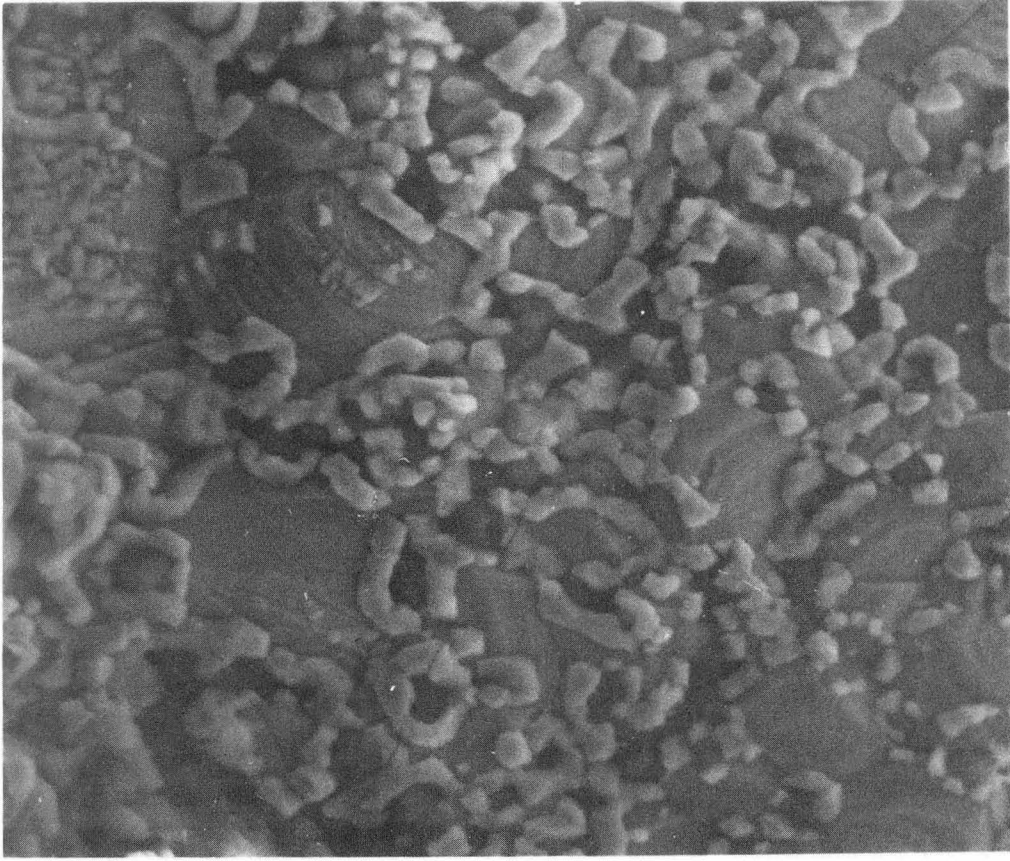
Figure 3.1.



XBL 8210-6747

Figure 3.2.

XBB 825-4587



10 μ m

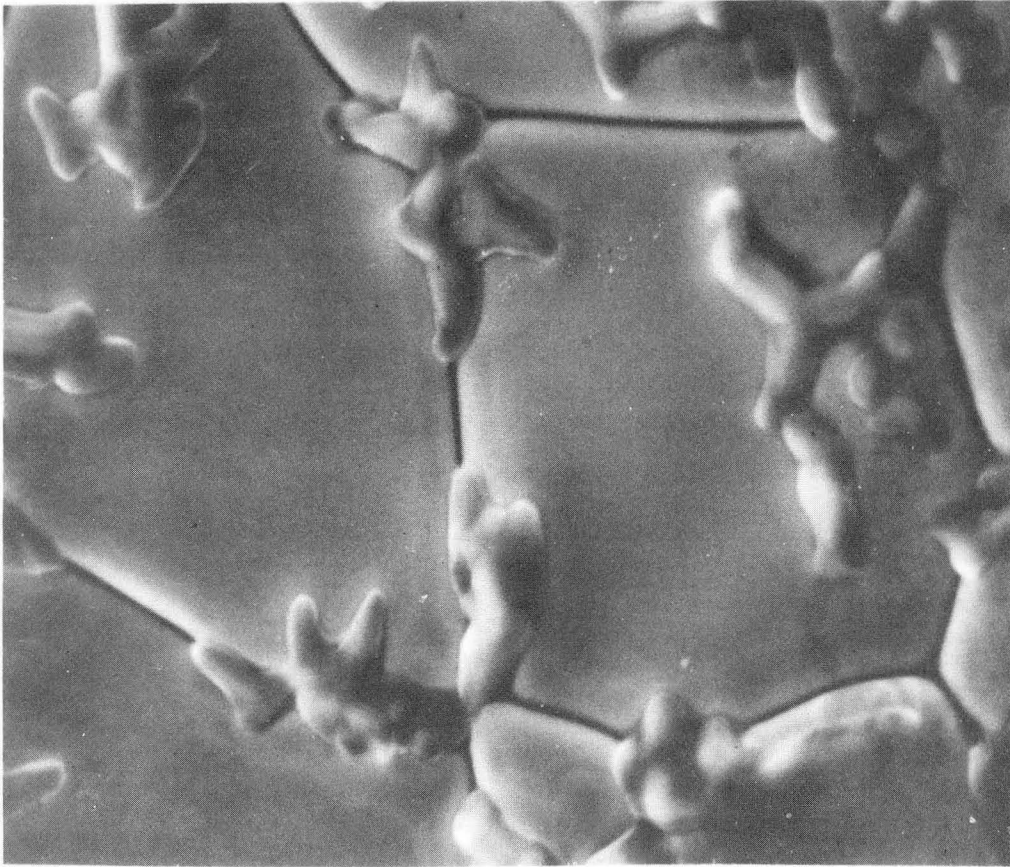


Fig 3.3.

Auger Electron Spectroscopy

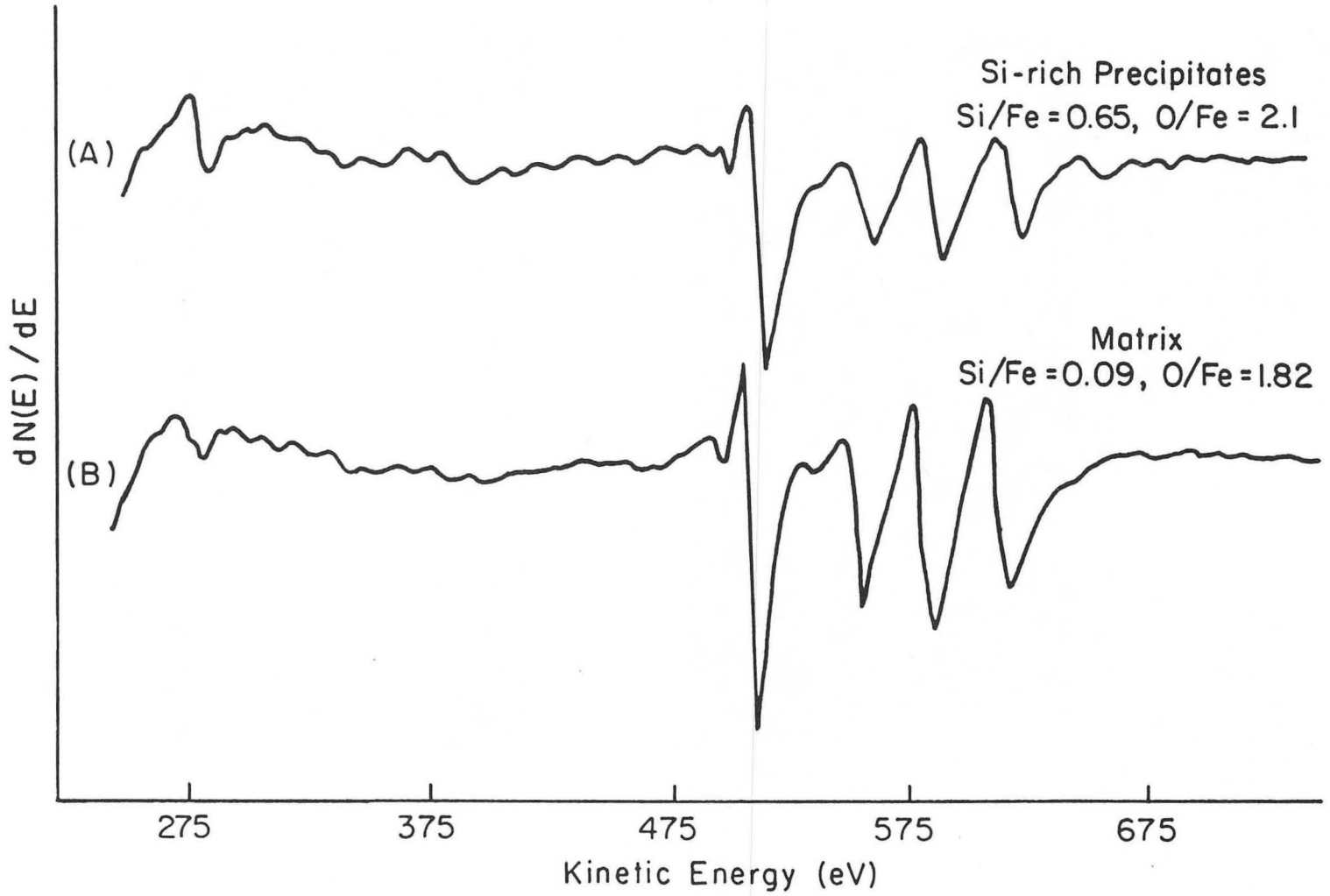
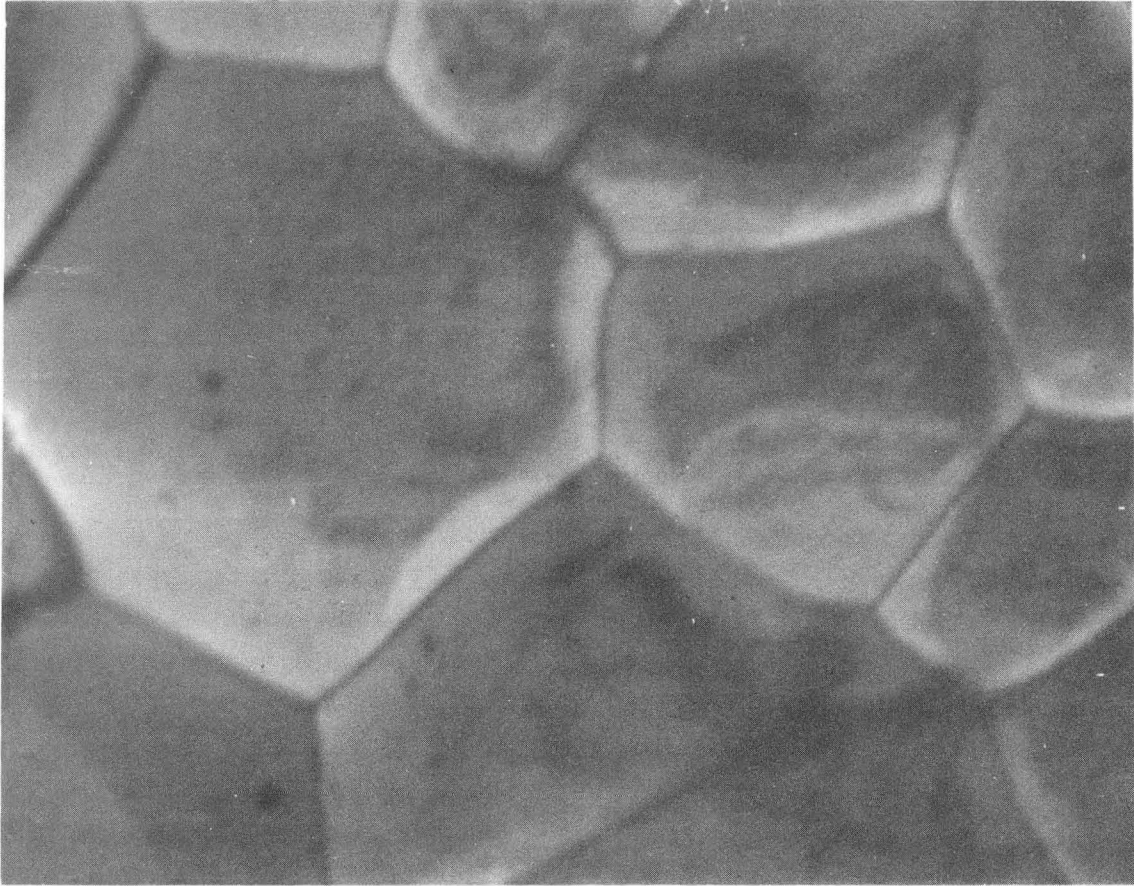


Figure 3.4.

XBB 829-8484



10 μ m

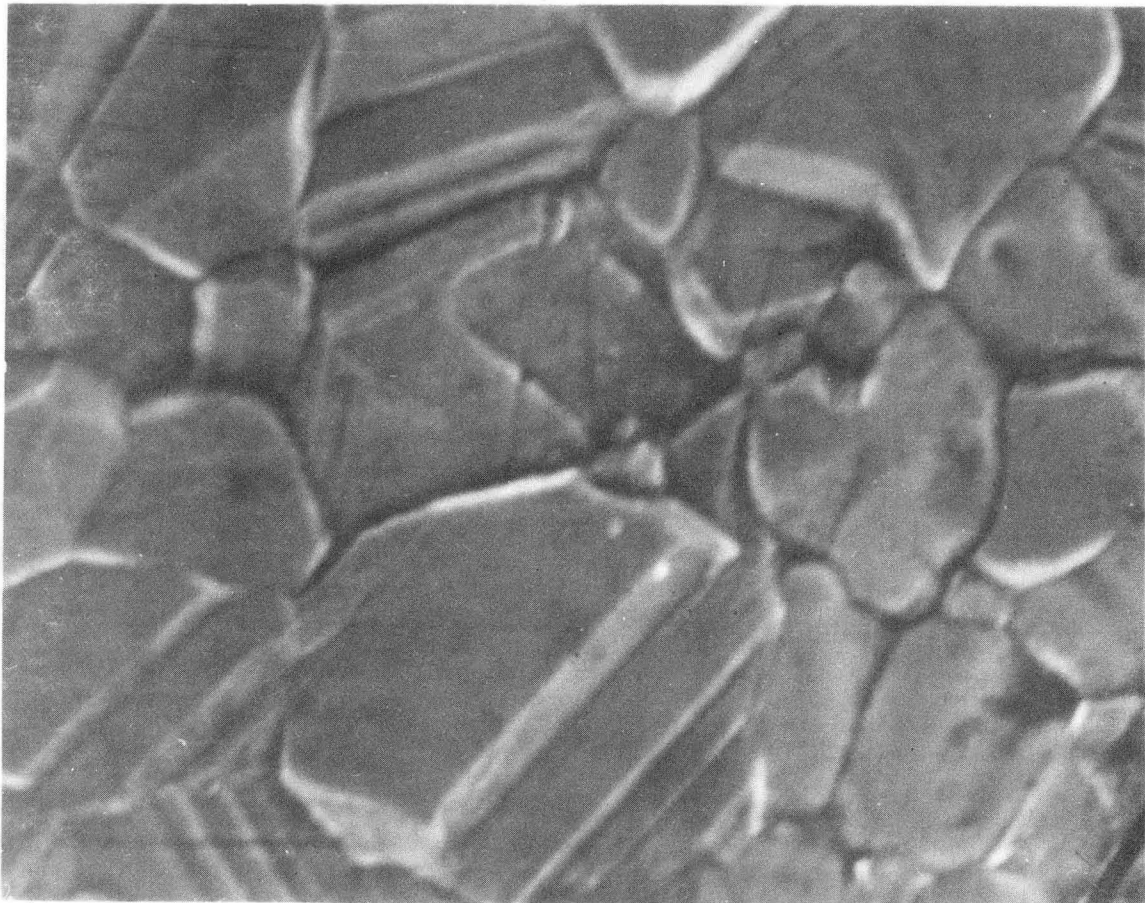


Fig 3.5.

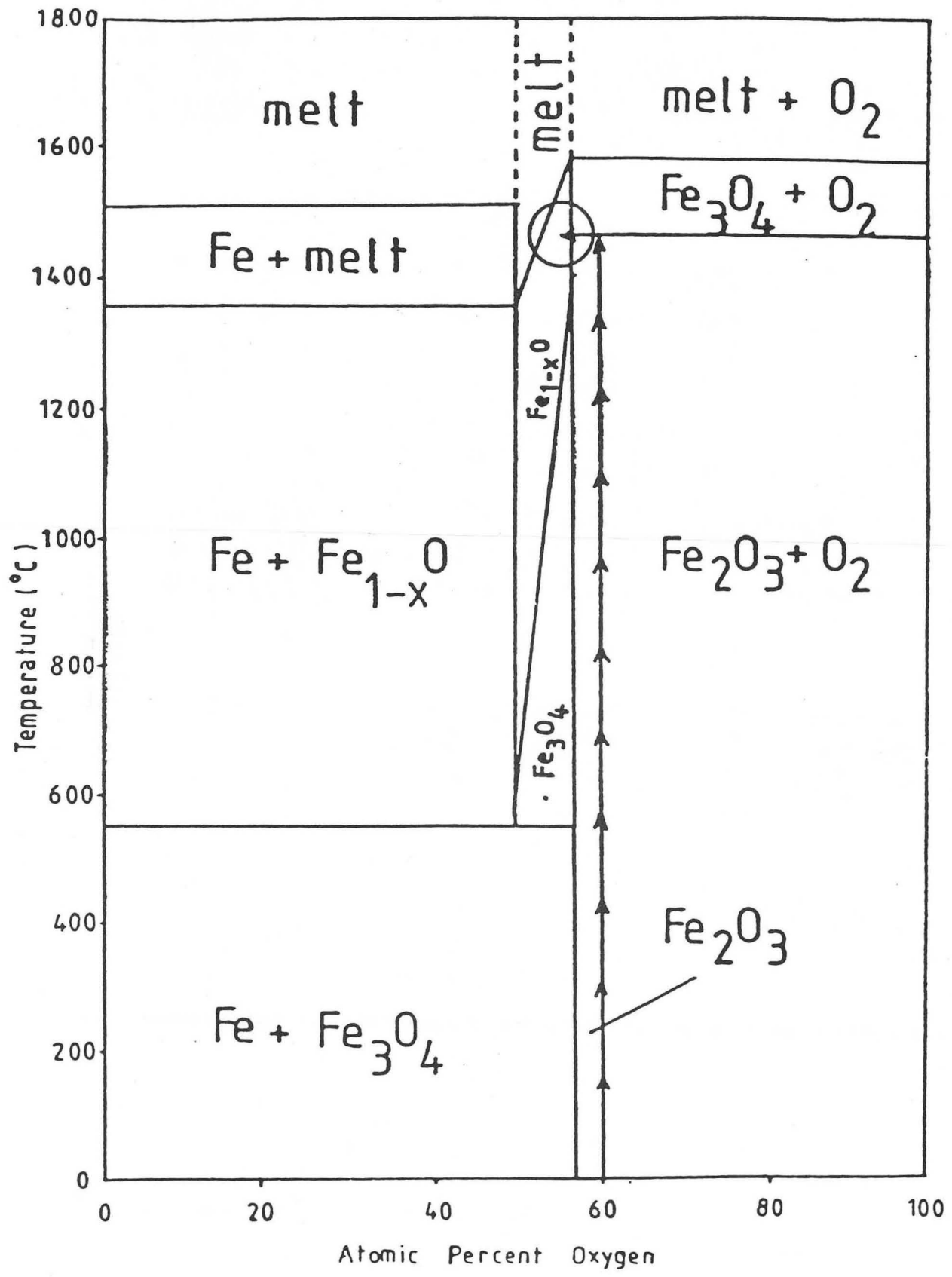
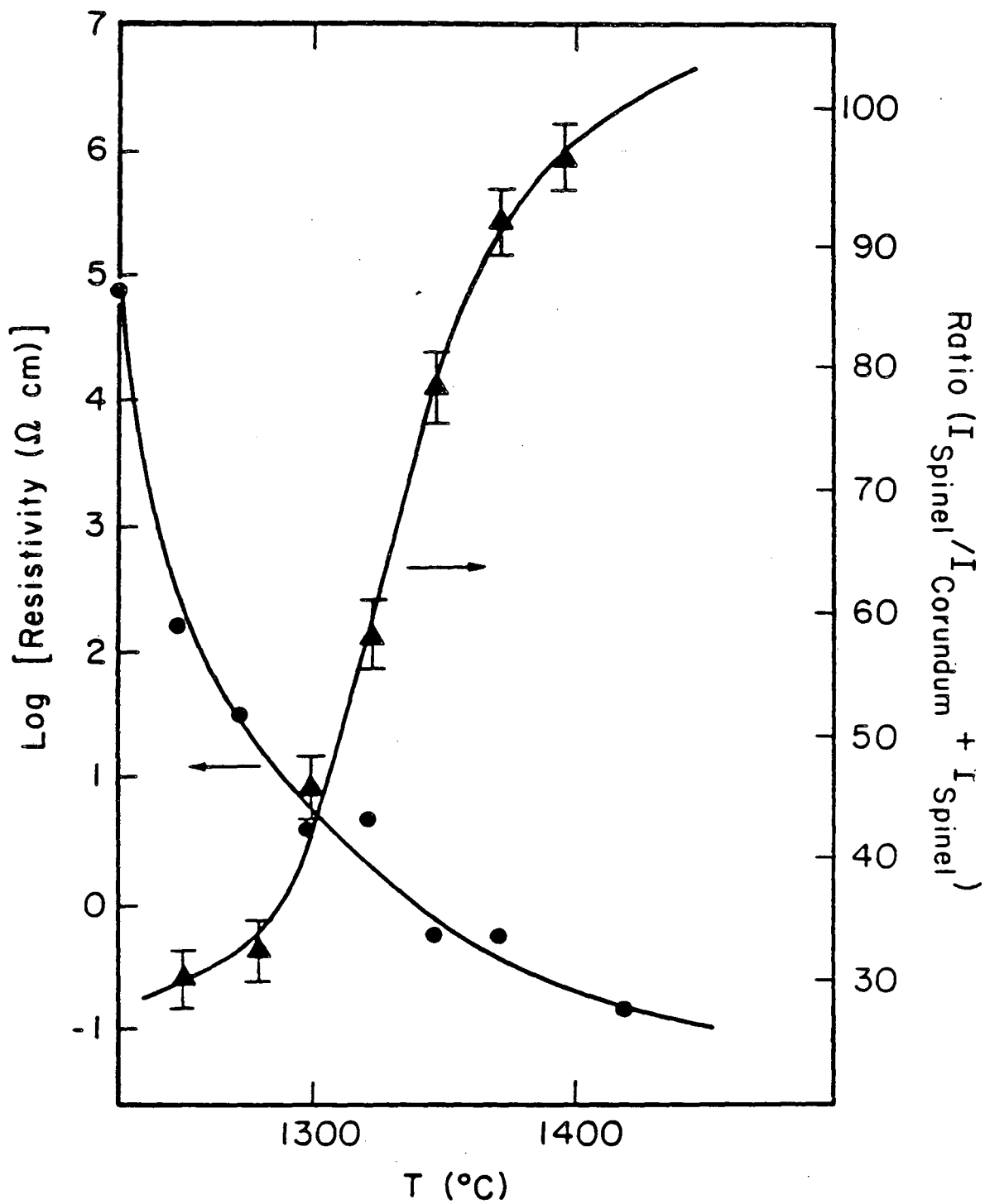
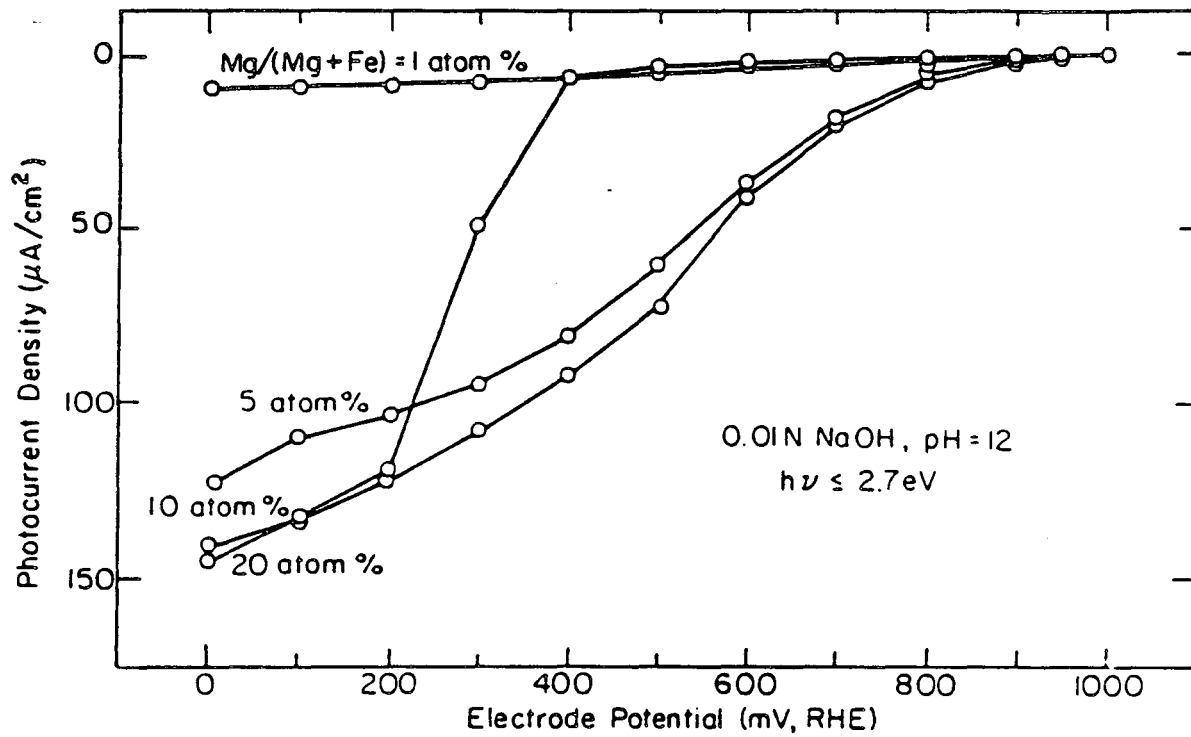


Figure 3.6.



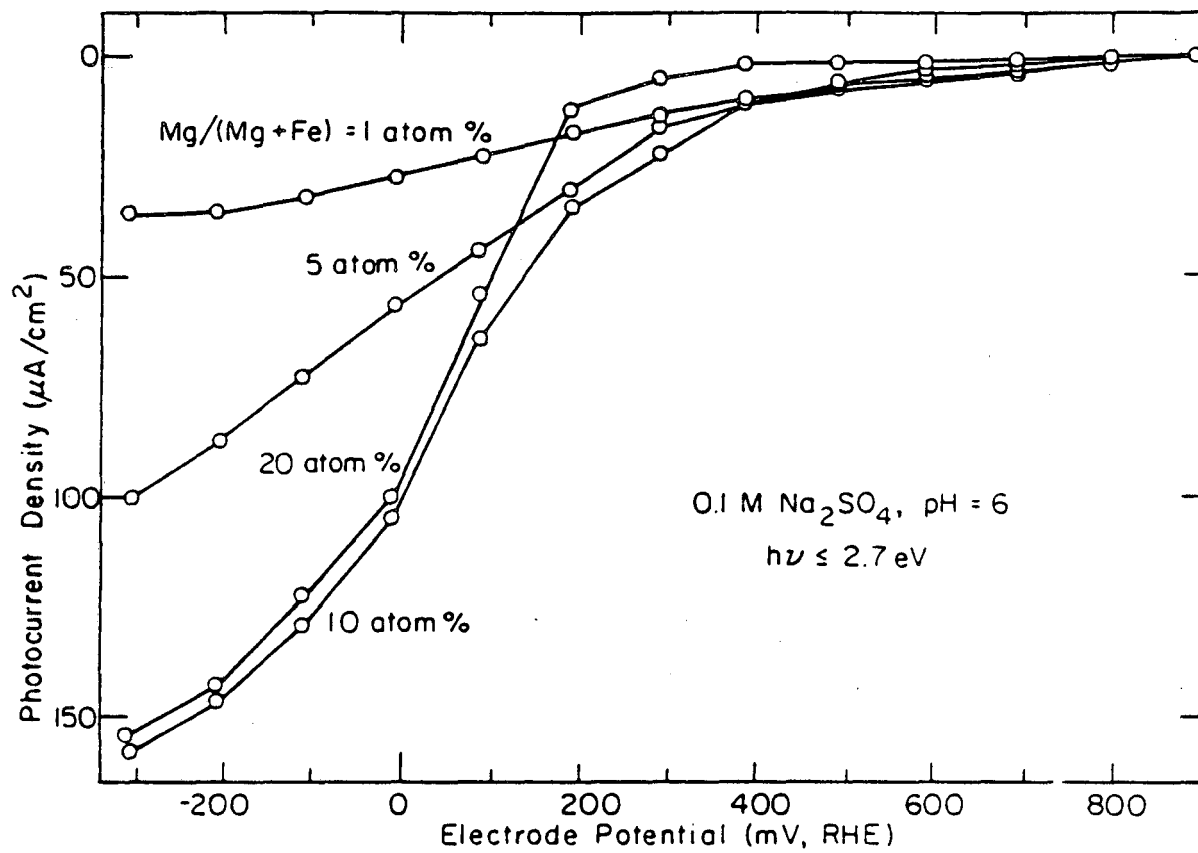
XBL 849-3729

Figure 3.7.



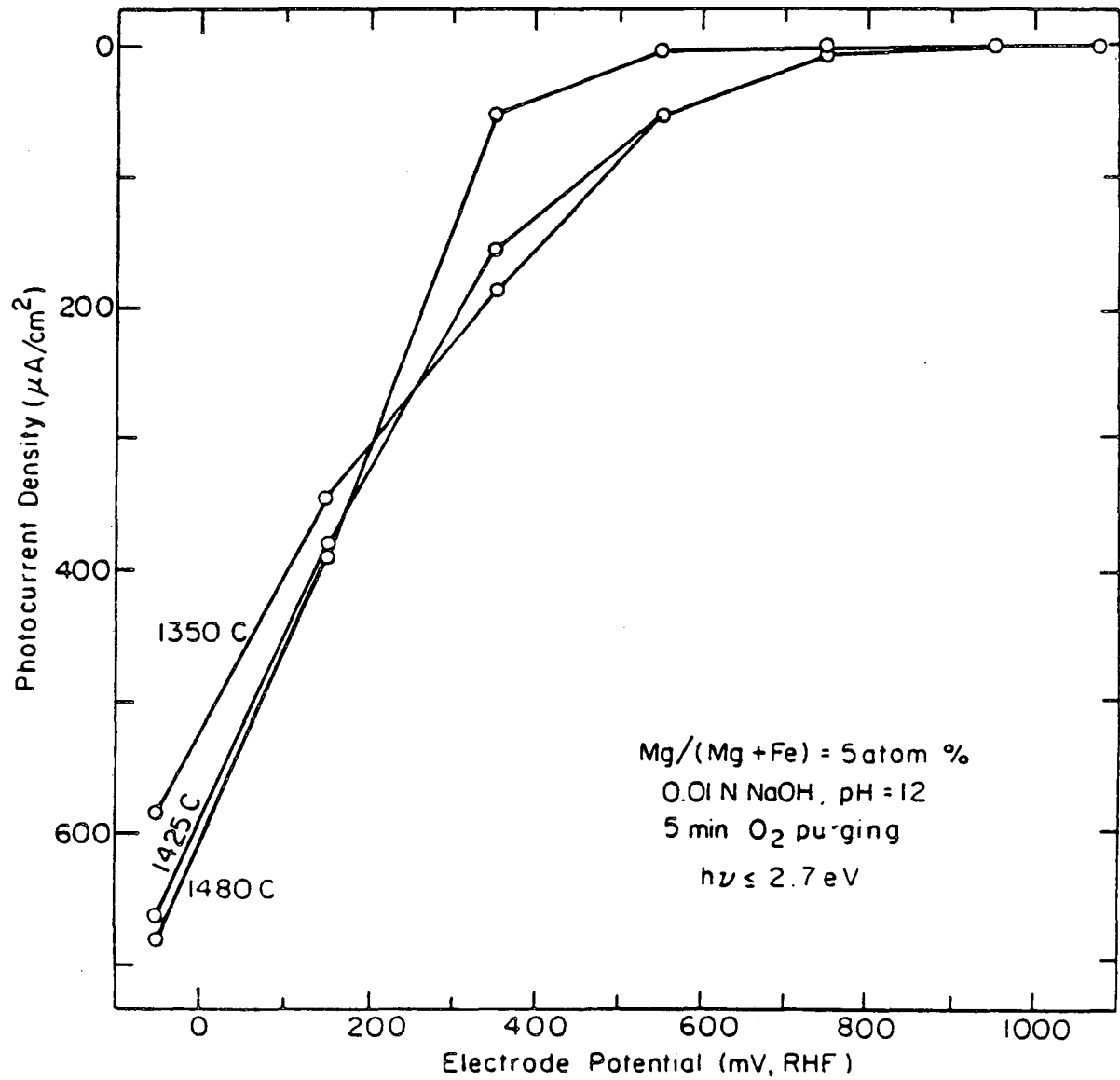
XBL 7210-6748

Figure 3.8.



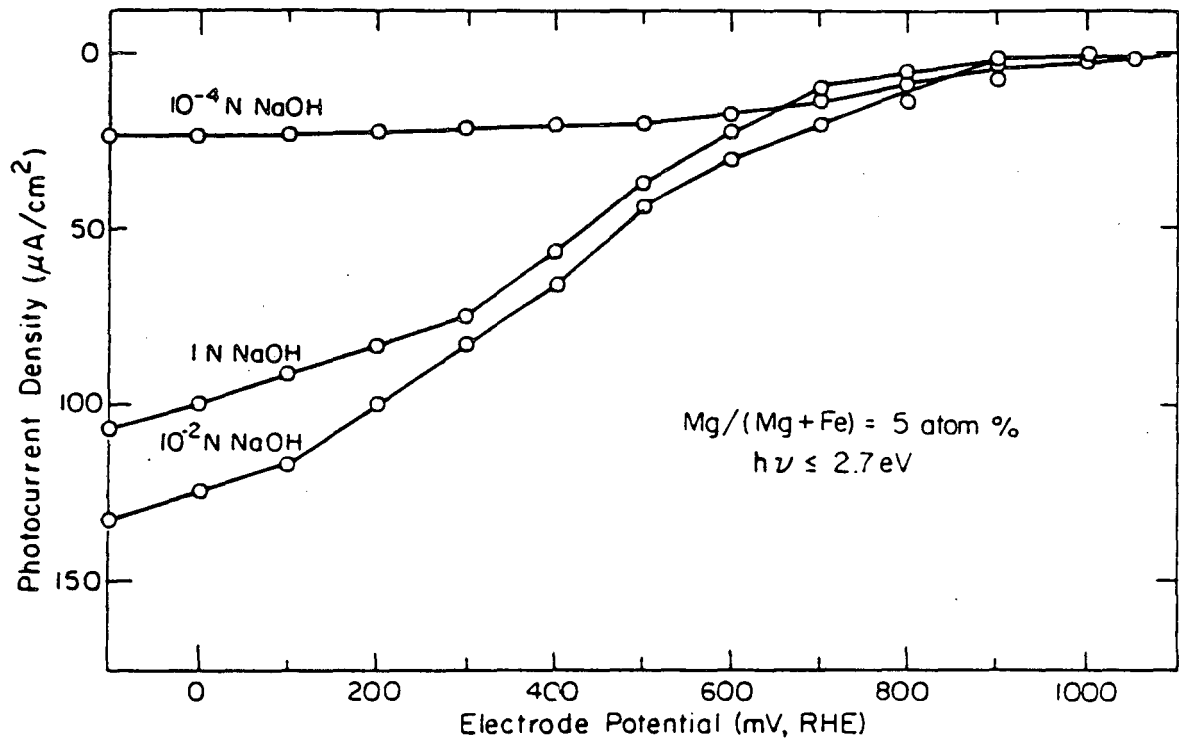
xBL 8210-6 750

Figure 3.9.



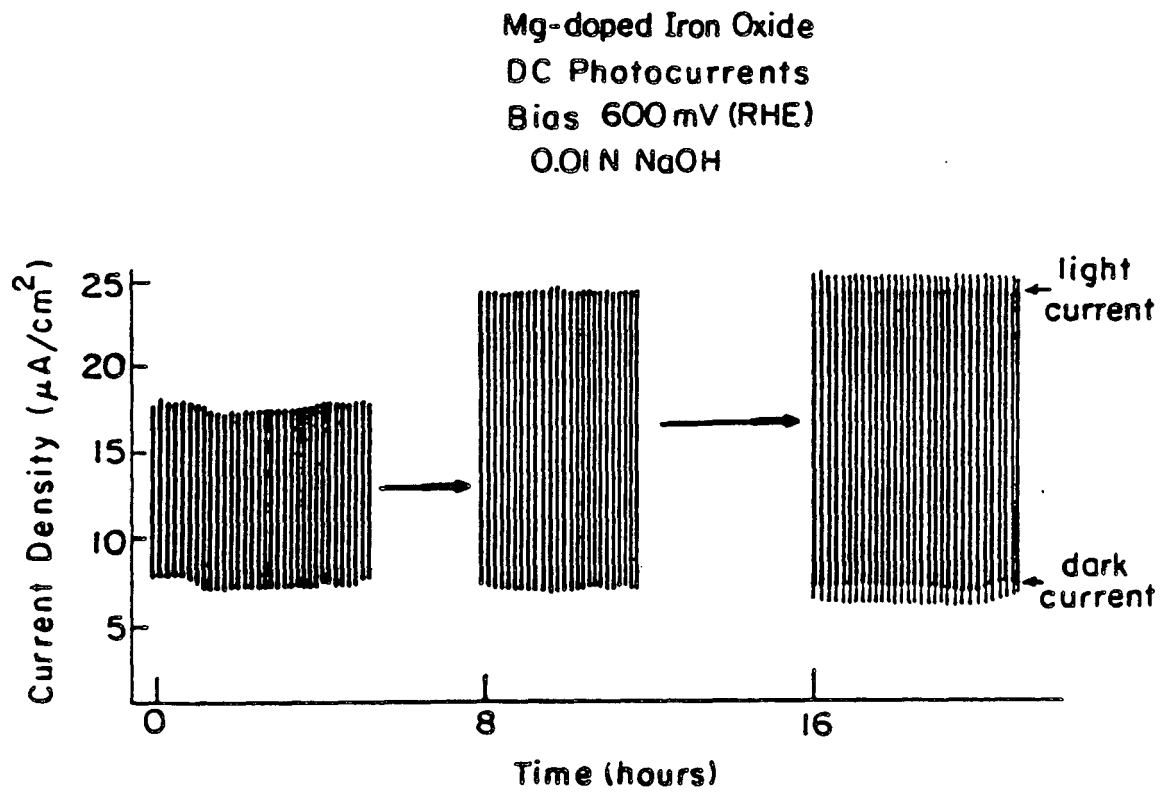
XBL 6210-6751

Figure 3.10.



XBL 8210-6749

Figure 3.11.



XBL 855-6264

Figure 3.12.

XBL 855-6263

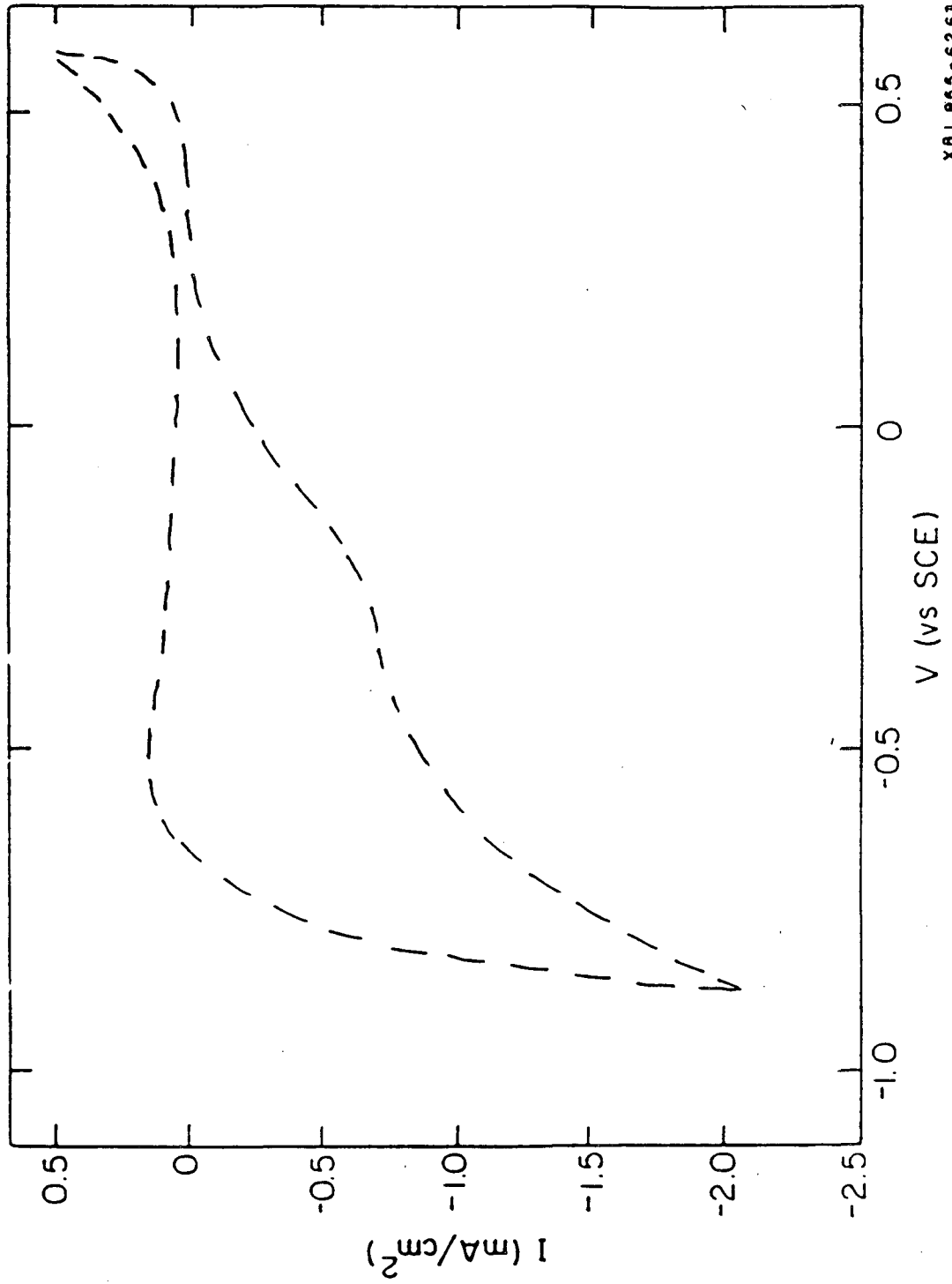
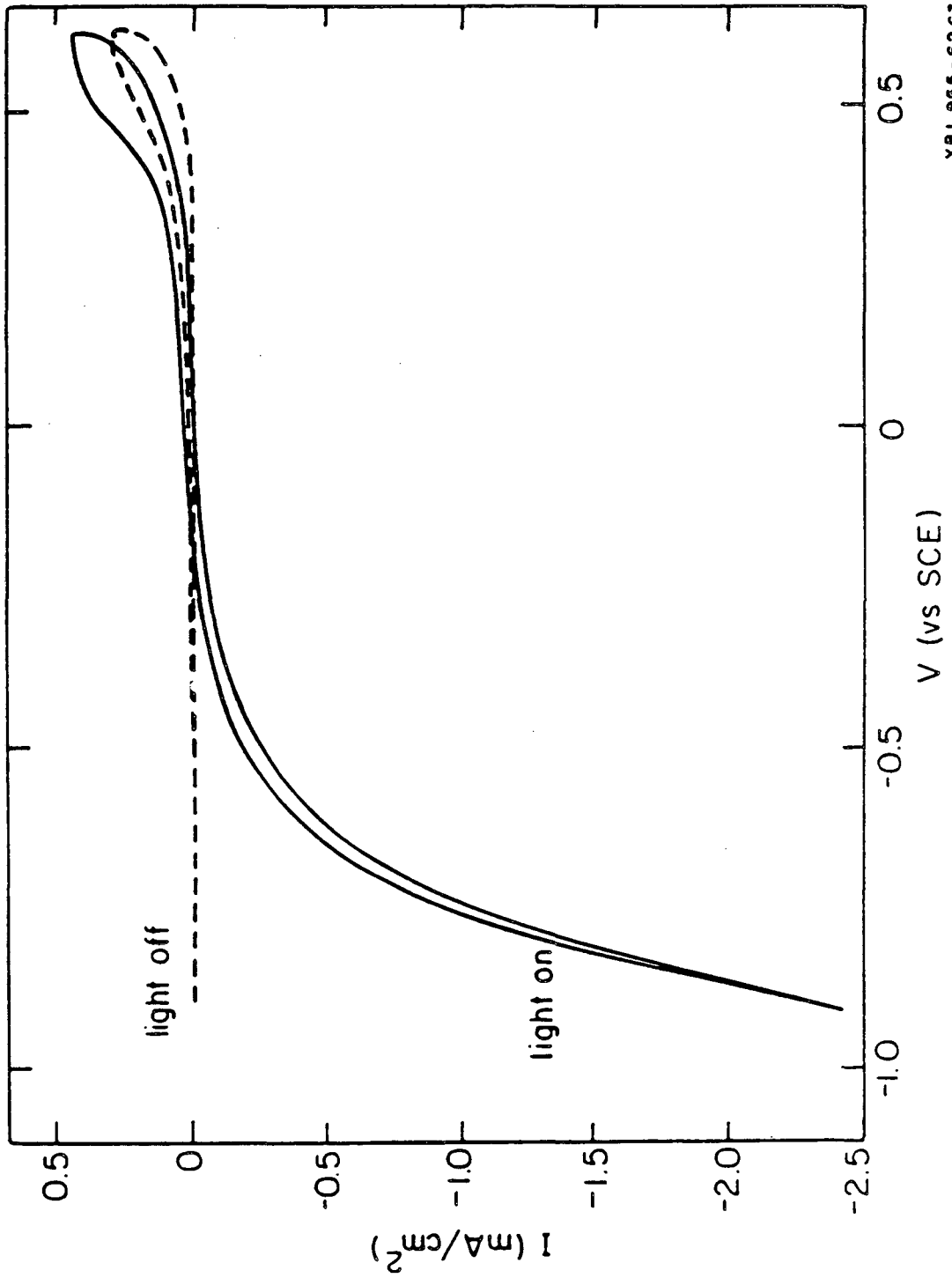


Figure 3.13.

Expected Behavior of a Pure p-Type Diode



XBL 055-6263

Figure 3.14.

5 at. % Mg-doped Iron Oxide

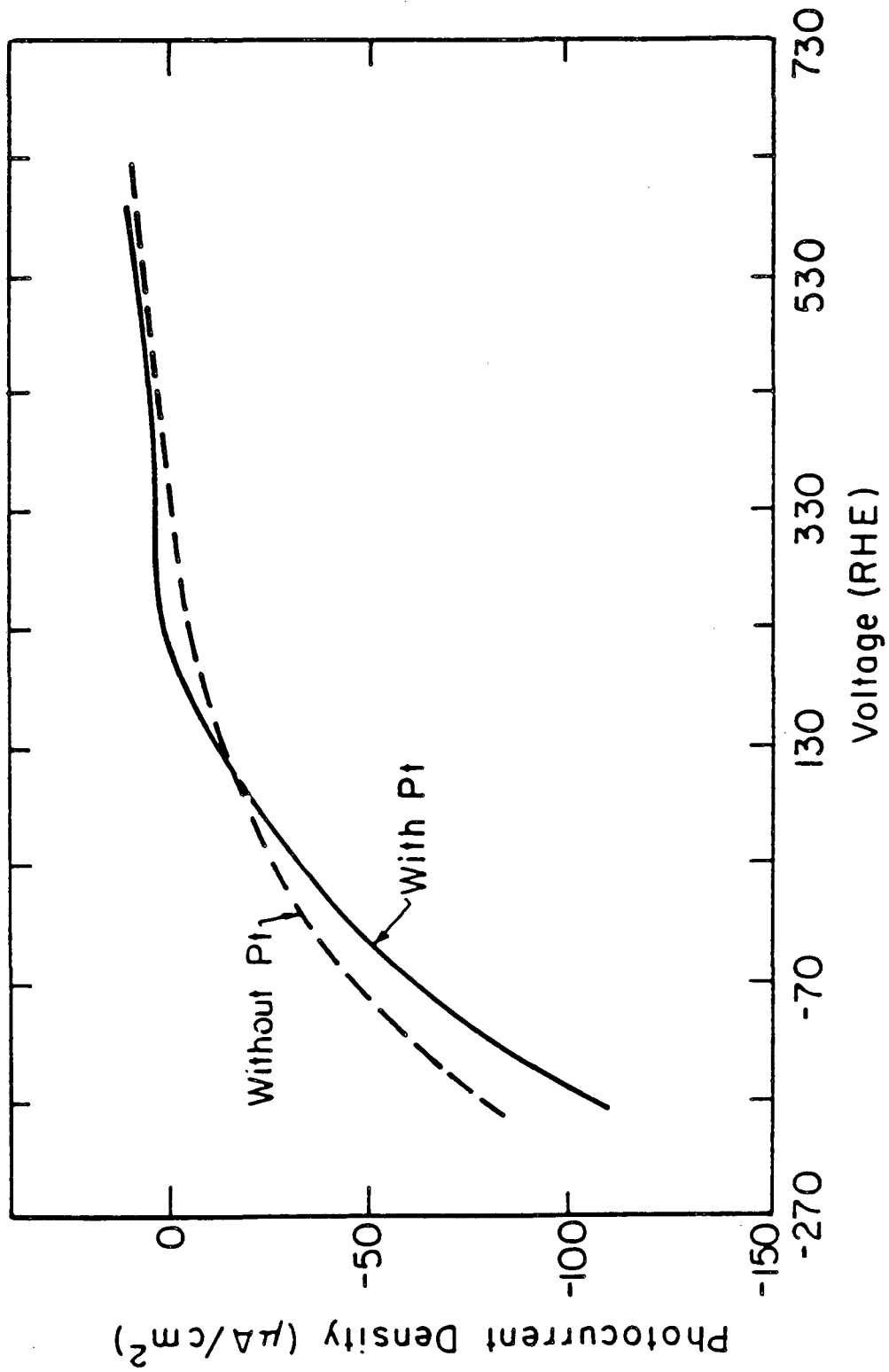


Figure 3.15.

References

- 3.1. J.H. Kennedy, R. Shinar, J.P. Ziegler, J. Electrochem. Soc., 127, 2307 (1980).
- 3.2. J.H. Kennedy, R. Shinar, and J.P. Ziegler, J. Electrochem. Soc. 127, 2307 (1980).
- 3.3. A.S.N. Murthy, K.S. Reddy, Mat. Res. Bull., 19, 241 (1984).
- 3.4. K.L. Hardee, A.J. Bard, J. Electrochem. Soc., 124, 215 (1977).
- 3.5. J.S. Curran, W. Gissler, J. Electrochem. Soc., 126, 56 (1979).
- 3.6. S.M. Wilhelm, K.S. Yun, L.W. Ballenger, N. Hackerman, J. Electrochem. Soc., 126, 419 (1979).
- 3.7. L.S.R. Yeh, N. Hackerman, J. Electrochem. Soc., 124, 833 (1977).
- 3.8. R. Shinar, J.H. Kennedy, J. Electrochem. Soc., 130, 392 (1983).
- 3.9. P. Iwanski, J.S. Curran, W. Gissler, R. Memming, J. Electrochem. Soc. 128, 2128 (1981).
- 3.10. K.G. McGregor, M. Clavin, J.W. Otvos, J. Appl. Phys., 50, 369 (1979).
- 3.11. L. Yeh, N. Hackerman, J. Electrochem. Soc., 124, 833 (1977).
- 3.12. R. Shinar, J.H. Kennedy, Solar Energy Mater., 1, 237 (1979).
- 3.13. R.F. Gardner, F. Sweett, D.W. Tanner, J. Phys. Chem. Solids, 24, 1183 (1963).
- 3.14. O.N. Salmon, J. Phys. Chem., 65, 550 (1961).
- 3.15. R. Kieckman, Ber. Bunsenges. Phys. Chem., 86, 112 (1982).
- 3.16. R.C. Weast, ed., CRC Handbook of Chemistry and Physics, 57th ed. (CRC Press, Cleveland) p. B-121.
- 3.17. A. Heller, ACS Symposium Series, ed. A.J. Nozik, 146, 57 (1981).

- 3.18. G.C. Kuczynski, Ferrites: Proceedings of the International Conference, p. 87-95. University Park Press, Baltimore, MD (1971).
- 3.19. P. Merchant, R. Collins, R. Kershaw, K. Dwight, A. Wold, J. Solid State Chem., 27, 307 (1979).
- 3.20. J.B. Goodenough, "Metallic Oxides", in Progress in Solid State Chemistry, ed. by H. Reiss, p. 297-312. Pergamon Press, NY (1971).
- 3.21. H. Mettee, J.W. Otvos, M. Calvin, Solar Energy Mater., 4, 443 (1981).
- 3.22. F.T. Wagner, G.A. Somorjai, J. Am. Chem. Soc., 102, 5474 (1980).
- 3.23. J.M. Bolts, M.S. Wrighton, J. Phys. Chem., 80, 2641 (1976).
- 3.24. F.T. Wagner, G.A. Somorjai, J. Am. Chem. Soc., 102, 5474 (1980).
- 3.25. D.E. Aspnes, A. Heller, J. Phys. Chem., 87, 4919 (1983).
- 3.26. F.T. Wagner, S. Ferrer, G.A. Somorjai, Surf. Sci. 101, 462 (1980).
- 3.27. H. Gerischer, J. Phys. Chem., 88, 6096 (1984).

Chapter Four

A Short Circuited Iron Oxide Assembly for the Photodissociation of Water

Sintered discs of Si- and Mg-doped α -Fe₂O₃ gave measurable photocurrents when put in ohmic contact with each other to form a short circuited assembly as shown in Figure 1.2. The chemical output power of the polycrystalline p/n iron oxide assembly was calculated from the measured photocurrents of our best assembly when illuminated by visible light with energy greater than 2.2 eV. Based on the free energy change when H₂ is produced from H₂O the output power is equal to $(1.23 \times i)\mu\text{W}$ where i is the measured photocurrent in μA . Using $15\mu\text{A}/\text{cm}^2$ as the photocurrent density obtained from our best short circuited assembly and an input power of 30mW , a power conversion efficiency of approximately 0.05% was obtained. This would be the power conversion efficiency assuming that all electrons which cross the electrode/electrolyte interface proceed to reduce hydronium ions to H₂ gas molecules, and that there are no other reactions.

With a power conversion efficiency of 0.05% this short circuit assembly would not provide a practical means of converting solar energy to chemical energy, and thus we began our efforts to maximize the power conversion efficiency by varying a number of parameters in the electrode preparation procedures and the operating conditions of the short circuited assembly.

If a photoinduced current is to occur between an n-type and a p-type sample in a short circuit configuration without any applied

potential, a necessary condition is that the onset potential of the n-type sample be less (more cathodic) than that of the p-type sample so that the operating potential will be located between the onset potentials of the Mg-doped and Si-doped samples as shown in Figure 3.1. When the two electrodes are put in ohmic contact with each other and immersed in an electrolyte solution the Fermi levels will become equal to each other and to the chemical potential of the solution as demonstrated in Figure 2.1. This will be the operating potential of the assembly. Also shown in Figure 2.1 is the production of a depletion layer and an accumulation layer in the n-type and p-type electrodes respectively when they are immersed in the aqueous solution. This produces the correct electric field gradients to drive electrons and holes to the surface in the cathode and anode, respectively, in order for the reduction/oxidation process to proceed.

We have reported the successful photodissociation of water in an unbiased p/n assembly consisting of doped iron oxides. In this assembly, a Mg-doped and a Si-doped iron oxide electrode acted as a photocathode and photoanode, respectively, for the reduction and oxidation of water. The spontaneous occurrence of these two processes under illumination is thermodynamically feasible only with the proper positioning of the conduction and valence band edges with respect to the redox couples in the electrolyte solution. The reduction of hydronium ions to hydrogen molecules is mediated by electrons from the conduction band of the photocathode. Therefore, a necessary condition for hydrogen production is that the conduction band edge of the Mg-doped iron oxide must lie at a potential more

negative than the hydrogen redox couple (0 V, RHE). Concomitantly, electron vacancies oxidizing hydroxyl ions move spontaneously toward lower potentials. Thus, for water oxidation to occur, the valence band edge for the n-type semiconductor must be more positive than the standard potential for water oxidation (1.23 V, RHE). Locations of the band edges for the Mg-doped and Si-doped iron oxide electrodes were determined in order to check that these criteria were satisfied in our iron oxide based system.

Depletion Layer Capacitance Measurements

Depletion layer capacitance measurements were made to determine the band edge locations of both electrodes with respect to the solution redox couples and to each other. The capacitance of the semiconductor space charge layer (C_{sc}) changes with applied potential (V_s) according to the Mott-Schottky relation (REF 4.1,4.2)

$$1/C_{sc}^2 = 2(q\epsilon\epsilon_0 A^2 N)^{-1}(V_s - V_{fo})$$

where ϵ is the semiconductor dielectric constant, A is the electrode surface area, N is the donor or acceptor density, and V_{fo} is the position of the Fermi level when there is no band bending.

Capacitances were determined independently for the Mg-doped and the Si-doped iron oxide electrodes in 0.01 N NaOH solution against a Pt counterelectrode. Measurements were made at a frequency of 1.5 kHz using a Pine RDE potentiostat. PAR model 124A lock-in amplifier, and a mercury oxide reference electrode. In Figure 4.1, the inverse square of the space charge capacitance ($1/C_{sc}^2$) is plotted against the applied voltage (V_s) with respect to the

reversible hydrogen electrode (RHE) for each of the electrodes. For heavily doped n-type semiconductors, the flatband is nearly coincident with the conduction band edge ($E_c \sim V_{fb} = 200$ mV, RHE). Conversely, for a heavily doped p-type semiconductor the flatband lies very close to the valence band edge ($E_v \sim V_{fb} = 2300$ mV, RHE). By using a known value for the Fe_2O_3 bandgap (2.3 eV) and flatband potentials from the Mott-Schottky measurements, one can construct an energy level diagram for the short-circuited doped iron oxide assembly. This is shown in Figure 4.2.

Separate measurements in which the Fermi level of the electrode assembly was measured against a mercury oxide reference electrode using a high impedance voltmeter have shown that the operating potential of the short circuited assembly with respect to a reversible hydrogen electrode is 750 ± 50 mV. Combining the band edge location and the operating potential of the assembly the amount of band bending of the assembly is also known. This information has been included in Figure 4.2.

From Figure 4.2, the operating details of the short-circuited p/n assembly are evident. Upon illumination of both electrodes by bandgap radiation ($h\nu > 2.3$ eV), electron-hole pairs are produced in both the n-type and p-type electrodes. In the n-type material, holes driven toward the electrode/electrolyte interface mediate the conversion of OH^- ions in solution to O_2 gas. Electrons driven toward the surface of the p-type electrode reduce H^+ ions to H_2 gas. At both electrodes, majority carriers diffuse away from the surface to contribute to the observed

photocurrents.

The valence band of the Mg-doped electrode and the conduction band of the Si-doped electrode with respect to the redox couples in solution (H^+/H_2 and O_2/OH^-) are positioned at energies such that the simultaneous evolution of H_2 and O_2 is thermodynamically feasible. By meeting these basic thermodynamic criteria, it is evident that an illuminated short circuited iron oxide assembly can photodissociate water without an external bias. It is particularly interesting that the conduction band of the Mg-doped iron oxide appears to be shifted cathodically with respect to the n-type electrode. It has been known for some time that iron oxides could be used for the oxidation of water (REF 4.3 - 4.5), however, the reduction of hydronium ions using iron oxide has not been reported in the past.

The cathodic shift of the conduction and valence band edges of the p-type iron oxide relative to the n-type electrode may be due to the effect of substituting Mg for iron in the iron oxide lattice, or by the presence of Fe_3O_4 in the lattice. A conduction band edge shift with the substitution of Mg^{2+} for Fe^{3+} can be explained using the following arguments of Butler and Ginley (REF 4.6). Butler and Ginley have proposed a model from experimental data conducted on ternary iron oxide systems in which the electron affinity of a composite system was calculated using the geometric mean of the electron affinities of the constituent atoms. Thus substitution of Mg dopant atoms (E.A. = 1.2 eV) with an electron affinity less than that of the iron atoms (E.A. = 1.7 eV) in the iron oxide lattice would lower the effective electron affinity of

the semiconductor (Figure 4.3) and shift the band edges toward more cathodic potentials. Doping with Si should shift the band edges of Fe_2O_3 in the opposite direction, if at all, since the electron affinity of Si (E.A. = 1.8 eV) is very similar to that of iron. Other factors such as the presence of surface recombination centers (REF 4.7), chemisorption of ions causing changes in the Helmholtz layer (REF 4.8) or the oxidation state of the cation in the semiconductor (REF 4.9) should be included for a more accurate prediction of the band edge and Fermi level locations.

On the other hand, the role of the Mg may solely be to initiate the formation of the spinel phase at lower temperatures. The existence of the spinel structure in the $\alpha\text{-Fe}_2\text{O}_3$ corundum structure does enhance the photocatalytic reactivity for water photodissociation. Using the band level diagrams shown by Goodenough for $\alpha\text{-Fe}_2\text{O}_3$ (REF 4.10) and Fe_3O_4 (REF 4.11), combined with optical absorption spectra (REF 4.12,4.13) and theoretical calculations (REF 4.14), one can see that the conduction band of Fe_3O_4 lies more cathodic (~ 0.5 eV) than the conduction band of $\alpha\text{-Fe}_2\text{O}_3$, assuming that the valence band (O 2p orbitals) edges of $\alpha\text{-Fe}_2\text{O}_3$ and Fe_3O_4 lie at the same energy when immersed in an aqueous NaOH solution (Figure 4.4). This is a very good assumption (REF 4.15,4.16). Thus, the inclusion of the Fe_3O_4 spinel phase in the $\alpha\text{-Fe}_2\text{O}_3$ corundum structure provides the existence of molecular orbitals at an energy more negative than the hydrogen redox potential on an electrochemical energy scale. The fact that the bandgap of Fe_3O_4 is only 0.1 eV is irrelevant as long as the electron hole pairs are created in the

α -Fe₂O₃ matrix, with the subsequent excitation of the electron from the α -Fe₂O₃ conduction band to the Fe₃O₄ conduction band. This requires 0.5 eV in addition to the bandgap energy of the α -Fe₂O₃ (2.2 eV). Measurements taken of the cathodic photocurrents from the Mg-doped electrodes with different wavelength cutoffs for the illumination source support this argument. In Figure 4.5 the measured cathodic photocurrents as a function of wavelength of the light are shown. There is an obvious increase in the cathodic photocurrents when light up to 2.7 eV is allowed to illuminate the electrode. This is exactly the bandgap energy plus 0.5 eV. The inclusion of Fe₃O₄ in the α -Fe₂O₃ matrix also serves to increase the conductivity of the electrons from the bulk to the surface of the electrode. The intrinsic resistivity of pure α -Fe₂O₃ is 10⁶ Ω cm, while Fe₃O₄ is a semimetal.

The alignment of semiconductor band edges relative to gas evolution redox potentials is critical. Holes at the n-type interface must arrive at a potential anodic of the O₂/OH⁻ half reaction. As seen from Figure 4.2, this energy requirement is satisfied with more than 1.2 eV to spare. Conversely, electrons must arrive at the p-type electrolyte interface at a potential equal to or cathodic of the H⁺/H₂ redox couple. As explained above, the origin of the electric field which drives electrons to the surface of the Mg-doped electrodes is not fully understood. It has been shown that the flatband potentials of the bulky electrodes of α -Fe₂O₃ are more positive than the H⁺/H₂ level (REF 4.17) even in the cases of doped materials (REF 4.18-4.22). From the Mott-Shottky (within the accuracy of our measurements), or the

energetic diagram described above, it appears that electrons do reach the solution from the Mg-doped (Fe_3O_4 containing) electrodes with enough energy to drive the hydrogen reduction reaction, but with scarcely enough energy. Therefore, if there is any activation energy barrier for the reduction process, the electrons coming from the Mg-doped $\alpha\text{-Fe}_2\text{O}_3$ conduction band must tunnel through this barrier. The probabilities for electron tunneling through an energy barrier are very low, which may be a major factor in limiting the output power of this short circuited device.

Once the flatband potentials and the operating voltage of the short circuited assembly have been determined one can also extract many other valuable parameters from the energy level diagram and the Mott-Schottky plots leading to information which will help in evaluating the functional characteristics of the assembly. Since the slope of the Mott-Schottky plots is given by $s = 2(q\epsilon\epsilon_0 A^2 N)^{-1}$ one can extract donor or acceptor concentrations for these semiconductor materials. Using a measured value of $A = 6 \text{ cm}^2$ for the electrodes and the dielectric constant for $\alpha\text{-Fe}_2\text{O}_3$ of $\epsilon = 100$ (REF 4.23), the acceptor density was calculated to be $N_A = 5 \times 10^{16} \text{ cm}^{-3}$ for the Mg-doped samples while the donor density for the Si-doped electrodes is $N_D = 2 \times 10^{18} \text{ cm}^{-3}$. Due to a considerable uncertainty in surface area determinations for these polycrystalline samples, charge carrier densities are reliable within an order of magnitude at best. Using these charge carrier concentrations from the Mott-Schottky plots and band bending values (V_{bb}) from Figure 4.2, depletion layer widths

were also calculated. With $W_0 = (2\epsilon\epsilon_0 V_{bb}/qN)^{1/2}$, the depletion layer widths in an operating p/n assembly for the p-type and n-type electrodes are approximately 500Å and 5000Å respectively. As was discussed in the section on doping, changing the amount of dopant added alters the carrier concentrations and hence the depletion layer widths. The width of the depletion layer is very important. The electrodes are illuminated at the surface and one wants to maximize the number of photons creating electron hole pairs. A small dopant concentration increases the width of the depletion layer and enhances electron-hole separation without wasting any of the incident photons. Maximized utilization of light for different widths of the depletion layer in a doped semiconductor is exemplified in Figure 4.6. Higher dopant levels decrease the space charge layer but also decrease the resistivity of the iron oxide. This is very important since the magnitude of the currents passed in these assemblies is on the order of 10^{-6} A. An additional consideration is the onset potentials of the electrodes. Again, if a photoinduced current is to flow between an n-type and a p-type sample in a short circuit configuration without any applied potential, a necessary condition is that the onset potential of the n-type sample be less (more cathodic) than that of the p-type sample, and that they be separated as much as possible in order to obtain the highest photocurrent between the two electrodes.

The lowest of the two photocurrents at that potential would determine the maximum current which could pass in the short circuited assembly. Therefore it is an advantage to shift the onset potentials of the Si-doped and Mg-doped electrodes to the most

negative and positive potentials, respectively, and to obtain the steepest rising and highest magnitude photocurrent possible in the assembly.

Taking into account the need for a low cell resistivity and using the data for the onset potentials of Mg-doped and Si-doped electrodes as well as considering light absorption, it is obvious that some intermediate dopant level should be used to satisfy all of these criteria as well as possible. These arguments support our finding of higher photocurrents in a short circuited assembly for samples doped with 5 and 10 atomic percent Mg than for samples doped with 1 and 20 atomic percent Mg against the same two percent Si doped sample (Table 1.1).

The results from the Mott-Schottky data and the energy level diagram are tabulated in Table 4.1 along with a summary of flatband potentials, charge carrier concentrations, and band edge locations for both the Mg-doped and Si-doped electrodes. The results for the Mg-doped electrode should be considered carefully. A Mott-Schottky plot is only valid when the data are accumulated during a static measurement, not a dynamic one. However, in this system, the Mg-doped electrodes contain Fe_3O_4 which permits the flow of electrons across the electrode/electrolyte interface as the potential on the electrode is varied. This causes a depletion of the charge in the capacitance layer of the electrode. The Mott-Schottky plot which is given as a figure is one of the few plots obtained from the Mg-doped materials which contained a reasonably linear region and which did not have a slope indicative of an n-type electrode.

TABLE 4.1

	<u>p-type iron oxide</u>	<u>n-type iron oxide</u>
Conduction band edge	~ 0 mV	~ 200 mV
Valence band edge	~ 2300 mV	~ 2500 mV
Band bending	~ 1550 mV	~ 550 mV
Majority carrier concentration	~ $5 \times 10^{16} \text{ cm}^{-3}$	~ $2 \times 10^{18} \text{ cm}^{-3}$
Depletion layer width	~ 5000 Å	~ 500 Å

The Production of H₂ and O₂ Gases From the Short Circuited Assembly.

Both hydrogen and oxygen gases have been detected from a short circuited assembly consisting of a 5% Mg-doped and a 2% Si-doped iron oxide electrode. The photocurrents measured from assemblies containing identically prepared electrodes varies from 2-15 μ A. Table 1.1 shows the photocurrent and measured hydrogen production from these assemblies. The best results were obtained from the Mg-doped samples with intermediate dopant concentrations. The most important fact contained in Table 1.1 is that illumination of both the p-type and the n-type electrode produces photocurrents which are greater in magnitude than the sum of the photocurrents obtained by illuminating the electrodes individually. Using the energy level diagram (Figure 4.2) one can see that the simultaneous photogeneration of electron/hole pairs in both of the semiconductors should be required for the photoelectrochemical oxidation and reduction processes to occur.

Hydrogen was measured from the assemblies by two methods. Originally the solutions were injected with H₂ to saturate the solution with hydrogen. With the low production rates of H₂ from the assembly, the time required to saturate the amount of solution used in the experiment with H₂ would have made the experiment impossible. Gas samples were taken from the system and analyzed in a gas chromatograph with attempts made to subtract the background from the injected H₂ gas which slowly diffused out of the solution. The background H₂ curve is shown in Figure 4.7. The amount of hydrogen produced from the short circuited assembly was so

small compared to the magnitude of the background that the original measurements contain a large amount of error. Thus, the originally reported one to one correlation of integrated photocurrents and detected hydrogen are not accurate.

Subsequently, a gas cell was designed with a much smaller volume of water so that the calculated time required to saturate the solution was very short. For these experiments the water solution was deaerated by bubbling the solution with nitrogen. A gas loop above the sample cell was filled with N_2 at the onset of the experiment and then closed off and circulated with a small mechanical pump fitted with teflon gears. The results of this experiment are shown in Figure 4.8 as a plot of the H_2 gas detected with time. The photocurrent was $8\mu A$ throughout the entire experiment. After two days of irradiation the first evidence of hydrogen production was seen. For the next 30 hours the hydrogen production rate continued to rise, at which point it began to decline. The photocurrents continued to be constant. Since the oxygen peak appears just after the hydrogen peak with a molecular sieve 5A column it was also noted that the oxygen peak had grown with time and had reached saturation after 30 hours. This experiment was repeated a number of times with very reproducible results. One possible explanation of this phenomenon is that the back reaction of oxygen reduction to form OH^- groups is occurring. Due to leaks in the system, the pure nitrogen in the circulation loop is slowly replaced by air. As the solution becomes concentrated with oxygen the reduction of O_2 becomes favored over the reduction of hydronium ions. Another feasible alternative

reaction occurring in the cell is the production of ammonia. Water may initially be split to form hydrogen and oxygen gases until the concentration of hydrogen in the solution is high enough to provide an H_2/N_2 ratio large enough for ammonia synthesis to ensue. It is well known that in the gas phase high pressure ammonia synthesis reactions a ratio of H_2/N_2 of $\gg 1$ is required to initiate the production of ammonia from H_2 and N_2 (REF 4.24). Iron also readily dissociates N_2 by a structure sensitive reaction (REF 4.25). Chemical analysis of the NaOH / H_2O solution after running a short circuited assembly with $16\mu A$ for several days showed the presence of NH_3 (REF 4.26). No quantitative measurements of the NH_3 were made so that the oxygen oxidation/reduction reaction could also still be occurring. In any case, since the photocurrents do not change with time, the number of electrons flowing across the electrode/electrolyte interface is the same whether O_2 or H^+ is being reduced.

As was discussed earlier, purging the solution with oxygen gas dramatically increases the photocurrents in a three electrode cell containing the Mg-doped iron oxide as the working electrode. When the oxygen purging was discontinued the photocurrents returned to their original value. This indicates that the currents were not due to a corrosion process or a reaction of the electrode with the oxygen, but rather an electrochemical reaction of only the oxygen and/or the oxygen and the electrolyte solution.

Obviously, the simultaneous detection of hydrogen and oxygen from the assembly when the solution was being purged with oxygen to prove that the hydrogen evolution decreases with increasing oxygen

content in the solution would be a valuable experiment. However, in the system used the hydrogen peak will not be separated from such an enormous oxygen signal in the gas chromatograph without increasing the length of the column and/or lowering the column temperature and hence the flow rate through the column. At that point the hydrogen signal would be too broad and thus very low in intensity and would not be discernible.

In order to show that oxygen gas (O_2) was being produced from the water, experiments were performed to monitor oxygen production from an assembly with a 5% Mg-doped iron oxide pellet in ohmic contact with a 10% Si-doped sample. Measurements were made in 0.01 N NaOH, using water isotopically labeled with 6% $H_2^{18}O$. Gas samples were collected over an assembly illuminated in this solution. Mass spectrometry was used to verify the production of $^{34}O_2$ giving direct evidence that water molecules were dissociating to form oxygen gas.

Oxygen has a high solubility in water ($3.16 \text{ cm}^3/100 \text{ cm}^3 \text{ H}_2\text{O}$) (REF 4.27), therefore much of the oxygen produced in this test remained dissolved in solution. In addition, leaks from the system prevented a direct comparison of oxygen production and integrated photocurrents. Instead, correspondence between oxygen yield and photocurrent was determined by the ratio of $^{34}O_2$ to $^{32}O_2$. Calculation of the relative oxygen ($^{34}O_2$ and $^{32}O_2$) yields involved two assumptions. First, no spontaneous water dissociation occurred, so that the oxygen initially dissolved in solution consisted only of $^{32}O_2$ and no $^{34}O_2$. Secondly, under equilibrium conditions, the ratio of $^{34}O_2/^{32}O_2$ in the

gas phase above the electrolyte solution was equal to that in solution. This equilibrium was assumed to be established rapidly as compared to sampling frequency (once every 24 hours). The relative amounts of $^{34}\text{O}_2$ and $^{32}\text{O}_2$ produced, depended on the relative probabilities of $^{16}\text{OH}^-$ and $^{18}\text{OH}^-$ oxidation at the anode. From a solution containing 6% isotopically labelled H_2^{18}O , the detectable concentrations of oxygen isotopes present at H_2 any time (t) were

$$[^{32}\text{O}_2] = C_0 + 0.88 \text{ rt, and } [^{34}\text{O}_2] = 0.12 \text{ rt.}$$

where r is the rate of oxygen production for all isotopes. The concentration of $^{32}\text{O}_2$ initially saturating the solution, C_0 , was calculated from Henry's Law to be 4×10^{18} molecules in 15 ml H_2O . With these calculations, the observed total oxygen production showed good correspondence (within 20%) with the predicted value. After 340 hours of intermittent gas production, the predicted value for the ratio of $^{34}\text{O}_2/^{32}\text{O}_2$ was 0.059. The measured value was $^{34}\text{O}_2/^{32}\text{O}_2 = 0.047$.

However, one should again consider the possibility of oxidizing and reducing only oxygen in the cell. If water is being oxidized to form oxygen gas and this oxygen gas is reduced on the opposite electrode to form OH^- ions again, a statistical distribution of $^{32}\text{O}_2$, $^{34}\text{O}_2$, and $^{36}\text{O}_2$ would still be observed which is identical to that which was observed in the last experiment. Although this experiment does conclusively show that O_2 is being produced from the water it does not exclude the possibility of reactions other than the production of H_2 and O_2 from H_2O occurring in the cell.

Long Term Stability of the Short Circuited Assembly

In some cases the p/n assemblies have run for hundreds of hours with no diminution of the photocurrents (Figure 4.9) and with no detectable corrosion of the electrode surfaces when examined by XPS and AES. As seen in Figure 4.9 the photocurrents measured from this short circuited assembly consisting of a 5% Mg-doped sample and a 2% Si-doped sample showed excellent long term stability. At first exposure to solution, the photoactivity was low ($I_{ph} = 3 \mu A$). However, the photocurrents steadily increased over an 80 hour period to a stable value of 15 μA . Once steady state behavior was established, the photocurrents persisted undiminished throughout 320 hours of continuous illumination. This type of induction period was observed in many of the short circuited assemblies studied. The cause of the initial rise in photocurrents was not determined; the electrodes showed no detectable changes during this period. Visually the electrodes did not suffer any color changes or topographical changes. Monitoring the oxidation state of the Fe before and after these experiments proved to be quite difficult (impossible). For chemical state analysis iron (III) can appropriately be labelled a black sheep in the periodic table of the elements. Predominantly, one sees a single photoelectron peak at an energy corresponding to the difference in energy between the initial and final states of an atom. Interactions of the exiting core level electron upon photoionization with unpaired electrons in the valence shell increases the number of possible final states of the atom. This is evidenced by a broadening of the observed XPS peaks. Due to the five unpaired d-electrons left when Fe(III) is ionized to Fe(IV)

the Fe (2p) lines are extremely broad. The broadening is further complicated by configuration interactions which lead to satellite structures. The Fe $2p_{3/2}$'s satellites fall between the Fe $2p_{3/2}$'s and Fe $2p_{1/2}$ peaks (Figure 4.10).

Dark currents in the short circuit assemblies were always less than one microamp and usually became even smaller with continued operation of the cell. This is a strong indication that the photocurrents are not due to corrosion processes, since then the dark currents would most likely also be high. These results are consistent with the findings of other investigators (REF 4.28) who have found iron oxide to be extremely stable in aqueous solution over a wide range of pH.

The data obtained for the short circuited assemblies is somewhat controversial. While many of the assemblies exhibited behavior like that in Figure 4.2 other short circuited assemblies were operated for short periods of time during which the photocurrent slowly diminished and eventually ceased. These electrodes also showed no visible corrosion and appeared to be similar to the functional electrodes when examined with XPS and AES, i.e. no noticeable reduction or oxidation of the electrodes occurred and no chemical impurities were present.

Reproducibility

One of the major concerns in this project has been the reproducibility of the photocurrents in the short circuited diode assembly. Although hydrogen has been produced regularly, the quantity of hydrogen detected compared with the integrated photocurrents does not show a one to one correspondence. The ratio

of the measured to expected hydrogen amounts varied, but was always less than 0.40. Some of this irreproducibility can be attributed to the inhomogeneity of the material. It is obvious that these polycrystalline materials are inhomogeneous. Some of the inhomogeneities can be minimized by mixing the MgO and Fe₂O₃ powders in small quantities so that each disc is assured of having the same MgO/Fe₂O₃ ratio. This does not insure the same distribution of Mg in the final sintered product, however, and this inhomogeneous distribution cannot be improved upon using this preparation procedure. In addition, sintering the pellets at high temperatures in an air atmosphere clearly reduces the material preferentially at the surface. This reduction leaves an oxygen deficient α -Fe₂O₃ phase at the surface and grains of inhomogeneously mixed Fe₂O₃ and Fe₃O₄ phases. If the Mg is an important element for the successful operation of these electrodes in a short circuited assembly, then this problem will be difficult to overcome.

On the other hand, the role of the Mg may solely be to initiate the formation of the spinel phase at lower temperatures. Attempts were made to grow single crystals of Fe₂O₃ doped with Mg²⁺ or Pb²⁺, but produced very high resistance materials. This indicates that perhaps the Mg²⁺ does not substitute for Fe³⁺ in the Fe₂O₃ structure (REF 4.29). However, sintering the pellets (>1350°C) may incorporate Mg into the spinel and/or corundum phases. If Fe₃O₄ alone is the crucial element in producing an operating short circuit assembly, then powders of Fe₃O₄ and Fe₂O₃ sintered at low temperatures should give the same results

as the Mg-doped and Si-doped assemblies when used in the short circuit assemblies.

Studies of the Electrode Surface

Photochemical techniques as well as ultra high vacuum spectroscopies have been used to show that the inhomogeneities of these materials in the near surface region can be related to the photoelectrochemical properties of the magnesium substituted iron oxide samples. It has been shown that iron oxide can exist in the form of very stable reduced states which are more active than the fully oxidized counterpart. This is discussed in detail in Chapter 5.

AC Photoelectrochemical Measurements

AC experiments were carried out in order to study the photocurrent response of our samples as a function of the depth of penetration of the light. In an AC photoelectrochemical experiment, photocurrents are separated from the dark currents, since only the light is modulated by the tuning fork. Furthermore, the use of monochromatic light allows the examination of a particular region of the space-charge layer because the absorption coefficient of a semiconductor is inversely proportional to the depth of light penetration.

The AC photoresponse as a function of applied potential at several different wavelengths is presented in Figure 4.11. The AC photocurrents were measured between -0.075 and 1.526 V RHE at wavelengths of 300, 400, 500, and 550 nm. The plots display both photoanodic as well as photocathodic currents and have been normalized to a constant photocurrent value at 1.526 V. RHE. The

Mg-doped electrodes generate (p-type) photocathodic currents when shorter wavelength irradiation is employed while photoanodic n-type behavior is observed upon illumination with longer wavelength light. A qualitative comparison of the curves shows that there is considerable inhomogeneity in the magnesium substituted iron oxide electrodes.

It appears that a surface region is present in the sintered disc electrodes which gives photocathodic currents under illumination. From the viewpoint of photoelectrolysis these results are remarkable because, despite the observation of an n-type Seebeck coefficient, the electrode behaves under illumination as if the space-charge layer potential gradients in the near surface region were similar to a true p-type semiconductor. Undoubtedly this behavior is related to the inhomogeneity of the ceramic material itself, as the disc contains multiple phases. If a surface inhomogeneity were present, it could in principle be abraded from the surface resulting in different electrochemical behavior.

Following the hypothesis that the near surface region is different from the bulk of the disc, the electrodes were sandblasted to remove the first 100 microns of the outer layer. The AC photoresponse of the abraded electrode is shown in Figure 4.12. It is clear that removal of the near surface region resulted in a complete reversal of the previously observed photocathodic currents. After abrasion, only photoanodic currents are observed. The results of this experiment indicate that, indeed, the near surface region of the discs has a different chemical character than the bulk. It should be noted, however, that in light of the high

temperatures of the preparation of the sintered discs, such inhomogeneities between the surface and the bulk are not surprising. The temperatures of preparation, 1200-1400°C are high enough to result in reduction of the surface. This is consistent with the observed instability of the electrodes during the cyclic voltammetry experiments.

In an attempt to identify the chemical nature of the near surface region of the discs, the surfaces of the ceramic discs were removed with a jeweler's file. X-ray powder diffraction of the surface powder showed no evidence for phases other than the corundum α -Fe₂O₃ and spinel Fe₃O₄ phases. However, the x-ray patterns were not of sufficient quality to provide a measurement of the relative quantities of the two phases as was presented previously. Photoelectron spectroscopy studies were used to determine the oxidation states of iron in the near surface region, and to determine the surface composition more accurately. The Fe (2p) peaks located at higher binding energy (706-710 eV) are too broad to obtain quantitative XPS measurements of Fe²⁺ and Fe³⁺ concentrations in iron oxide compounds (REF 4.30,4.31). Oku and Hirokawa have shown that the lower binding energy Fe (3p) peaks exhibit satellite characteristics for Fe²⁺ ions which are easily discernible from the Fe³⁺ satellite structures (Figure 4.13) (REF 4.32). Using this data, analysis of the XPS spectrum taken from a Mg-doped α -Fe₂O₃ pellet suggests that the ratio of Fe²⁺/Fe³⁺ at the surface is roughly 0.5. Bulk x-ray analysis of the same sample showed that the ratio of Fe₃O₄ to Fe₂O₃ was 0.25 or Fe²⁺/Fe³⁺ = 0.1 for the bulk, combining the results from

the AC photocurrent measurements and the XPS spectra it is clear that the near surface region of the pellets plays a crucial role in the photodissociation process. The AC depth profile (Figure 4.11) shows that the p-type behavior is present only near the electrode surface (within 1000Å) where there is an enhancement of F^{2+} valence states (XPS, Figure 4.14).

The next logical step, knowing the importance of the electrode surface and the presence of reduced states of the iron, was to study the electrode surface more carefully under controlled conditions in the UHV chamber.

Figure Captions

- Figure 4.1. Mott-Schottky plots of the inverse square of space charge capacitance $(1/C_{sc})^2$ versus applied potential (V_a) for A) 10% Si in Fe_2O_3 and B) 5% Mg Fe_2O_3 electrodes. Performed at 1500 Hz frequency in 0.01 N NaOH against a Pt counterelectrode.
- Figure 4.2. Proposed energy level diagram for an operating short circuited iron oxide assembly.
- Figure 4.3. Pictorial representation of the work function, electron affinity, Fermi level in relation to both the electrochemical and spectroscopic energy scales.
- Figure 4.4. Alignment of Fe_2O_3 and Fe_3O_4 valence and conduction bands when immersed in an aqueous solution.
- Figure 4.5. Photocurrent with applied voltage for different wavelengths.
- Figure 4.6. Utilization of light for different widths of the depletion layer in a doped semiconductor.
- Figure 4.7. H_2 detected over time after hydrogen injection from a syringe from a cell containing no sample.
- Figure 4.8. Hydrogen evolution from a small volume cell (10 ml)

containing a short circuited iron oxide assembly. No hydrogen was initially introduced into the cell. Time 0 = after 2 days irradiation.

Figure 4.9. Photocurrent as a function of time for a short circuited assembly during the first immersion in solution.

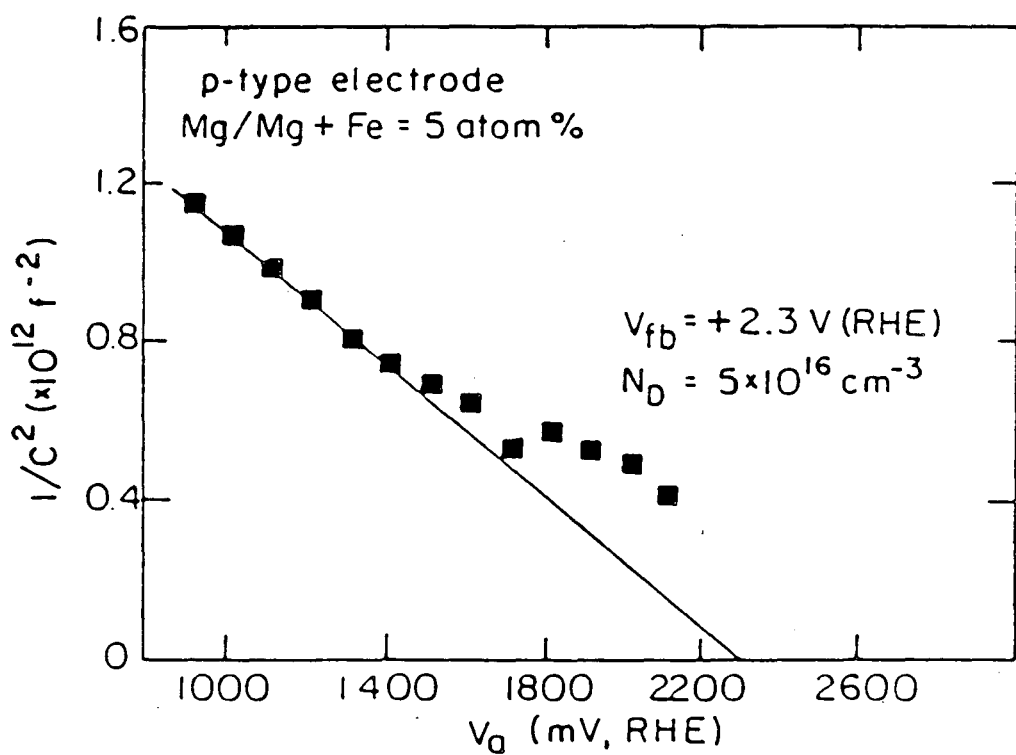
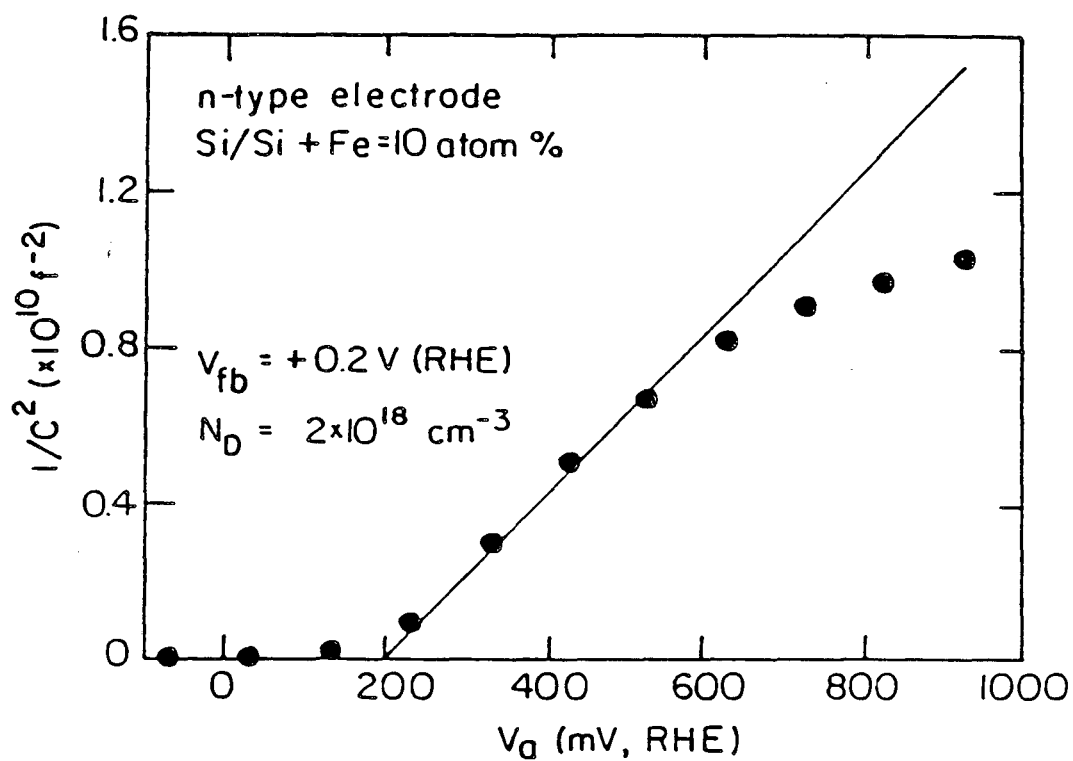
Figure 4.10. XPS spectrum of clean, pure α -Fe₂O₃, Fe(III) in comparison with the XPS spectrum from a Mg-doped pellet.

Figure 4.11. AC photoresponse of a Mg-Fe₂O₃ electrode as a function of applied potential at several different wavelengths. All data were normalized to have equal intensity at 1350nm wavelength.

Figure 4.12. AC photoresponse of an abraded Mg-doped iron oxide electrode.

Figure 4.13. XPS satellite structure for the Fe (3p) photoemission lines. (REF 4.32).

Figure 4.14. Deconvoluted Fe (3p) photoemission lines for a Mg-doped iron oxide electrode.



XBL83I-S155A

Figure 4.1.

ENERGETICS OF CONNECTED P-TYPE AND N-TYPE IRON OXIDES

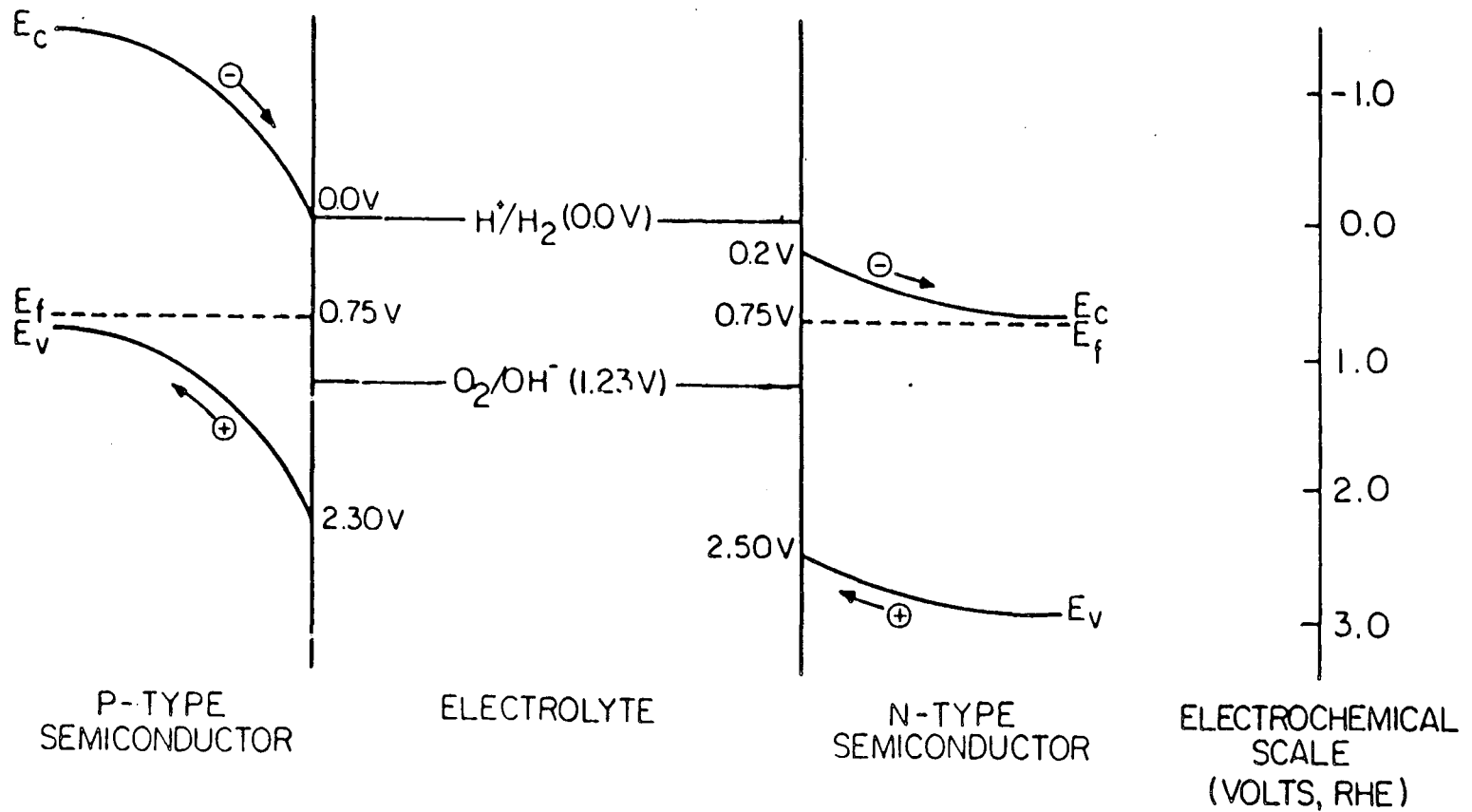
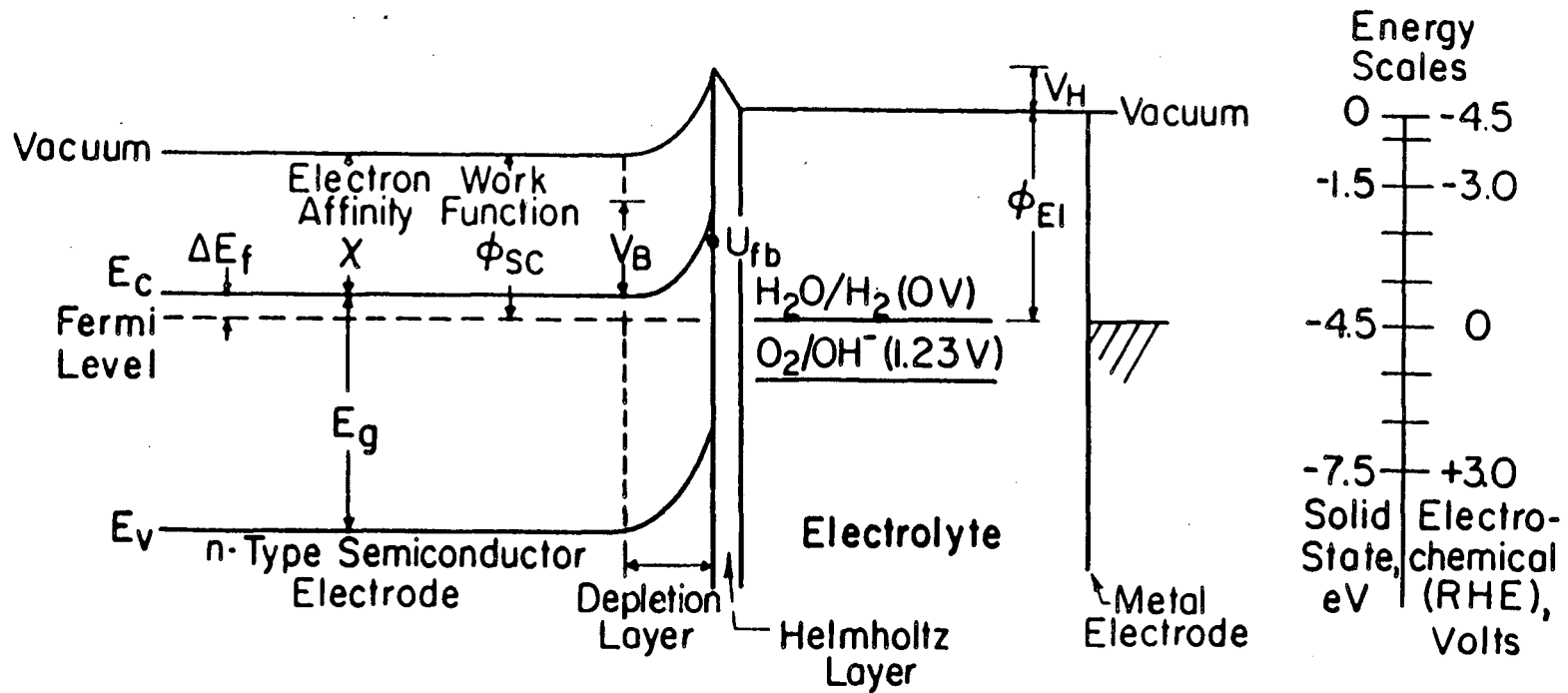


Figure 4.2.

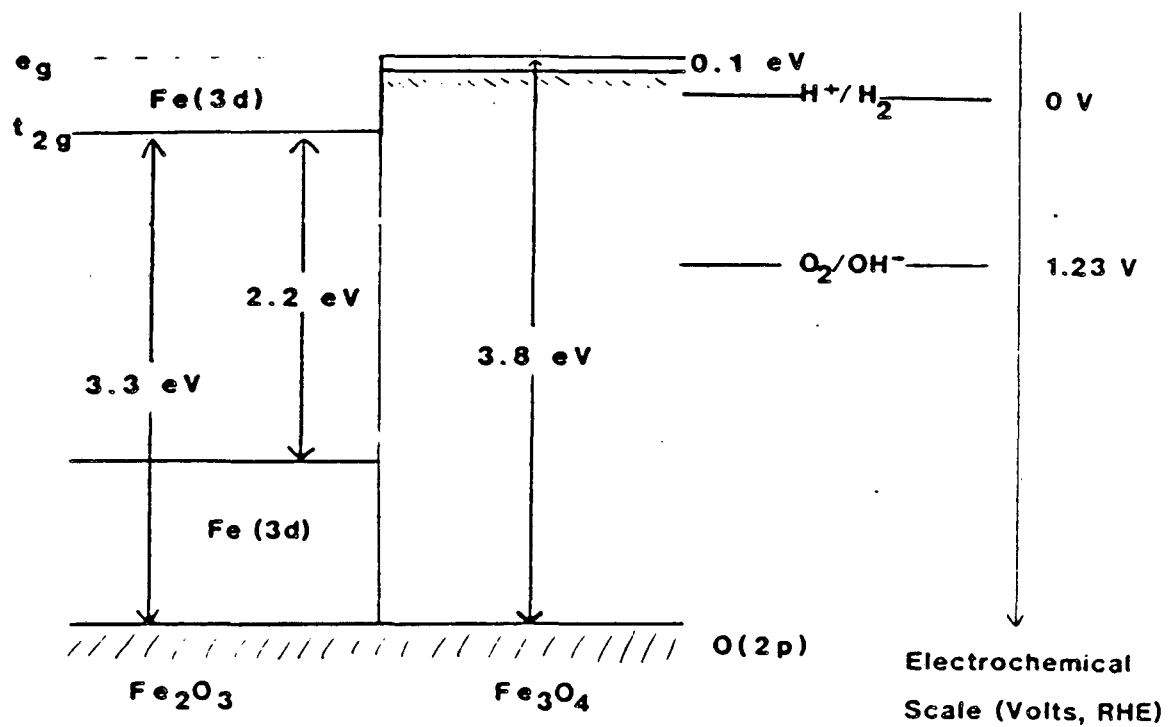
Figure 4.3.



XBL849-7369



Energy levels in solution



XBL 852-1404

Figure 4.4.

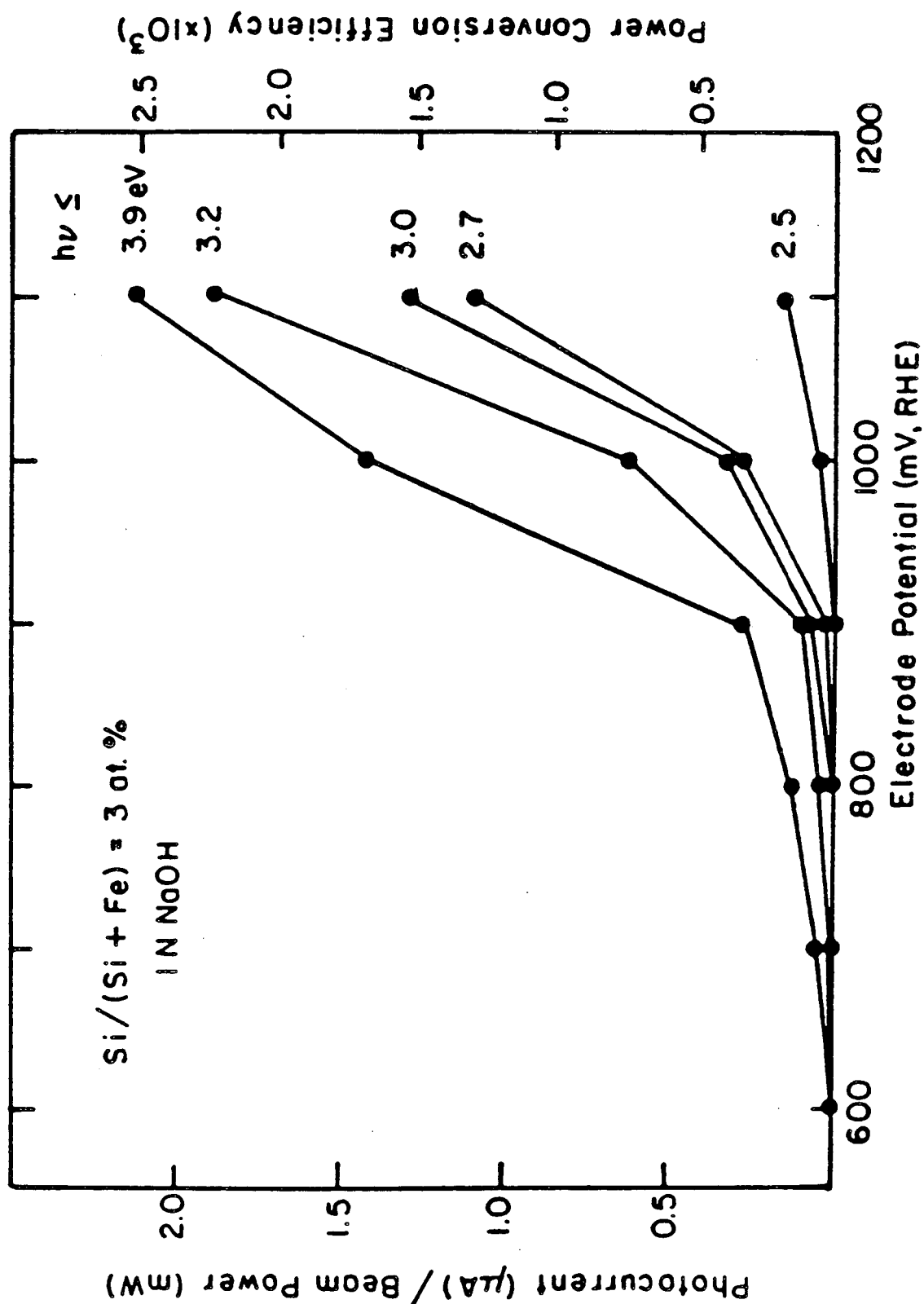
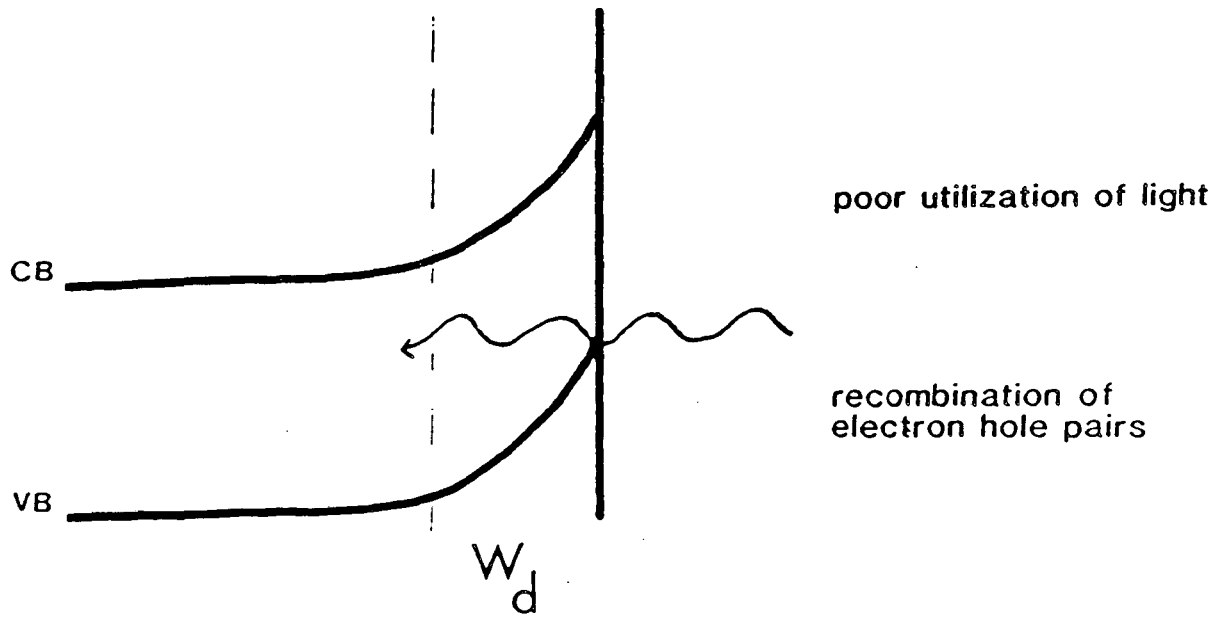


Figure 4.5.

Narrow depletion layer and/or
Light penetration beyond depletion layer



Wider depletion layer and/or
Light penetration within depletion layer

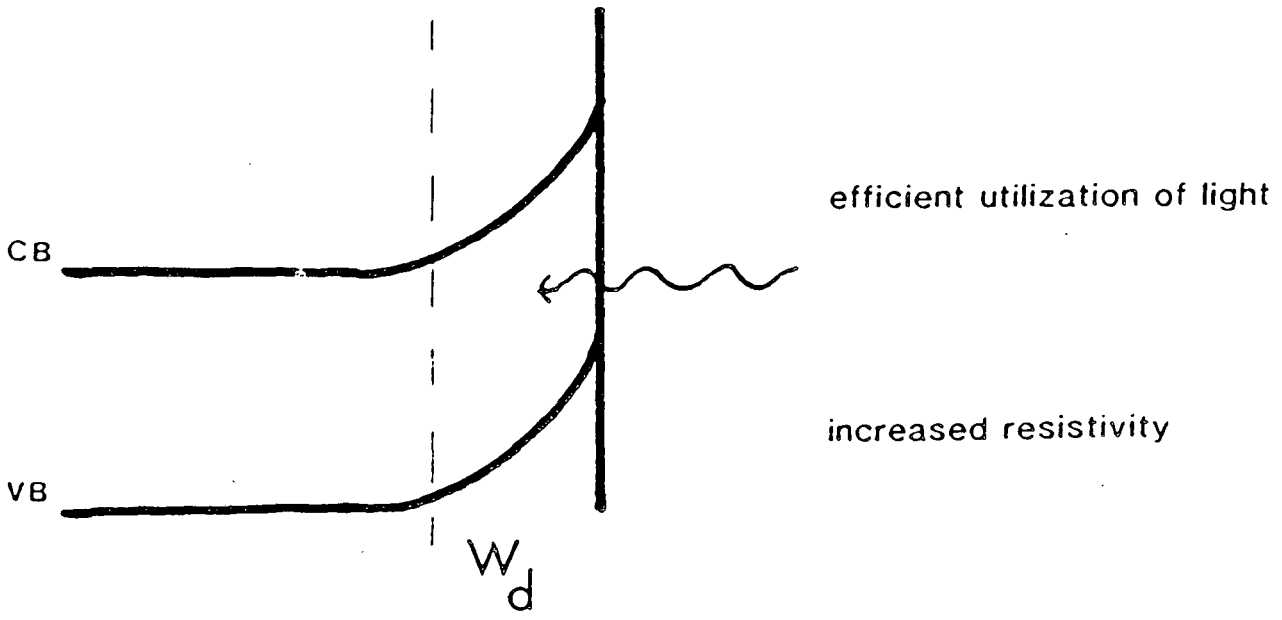


Figure 4.6.

Background Hydrogen Detected From a Short Circuited Assembly After H₂ Injection

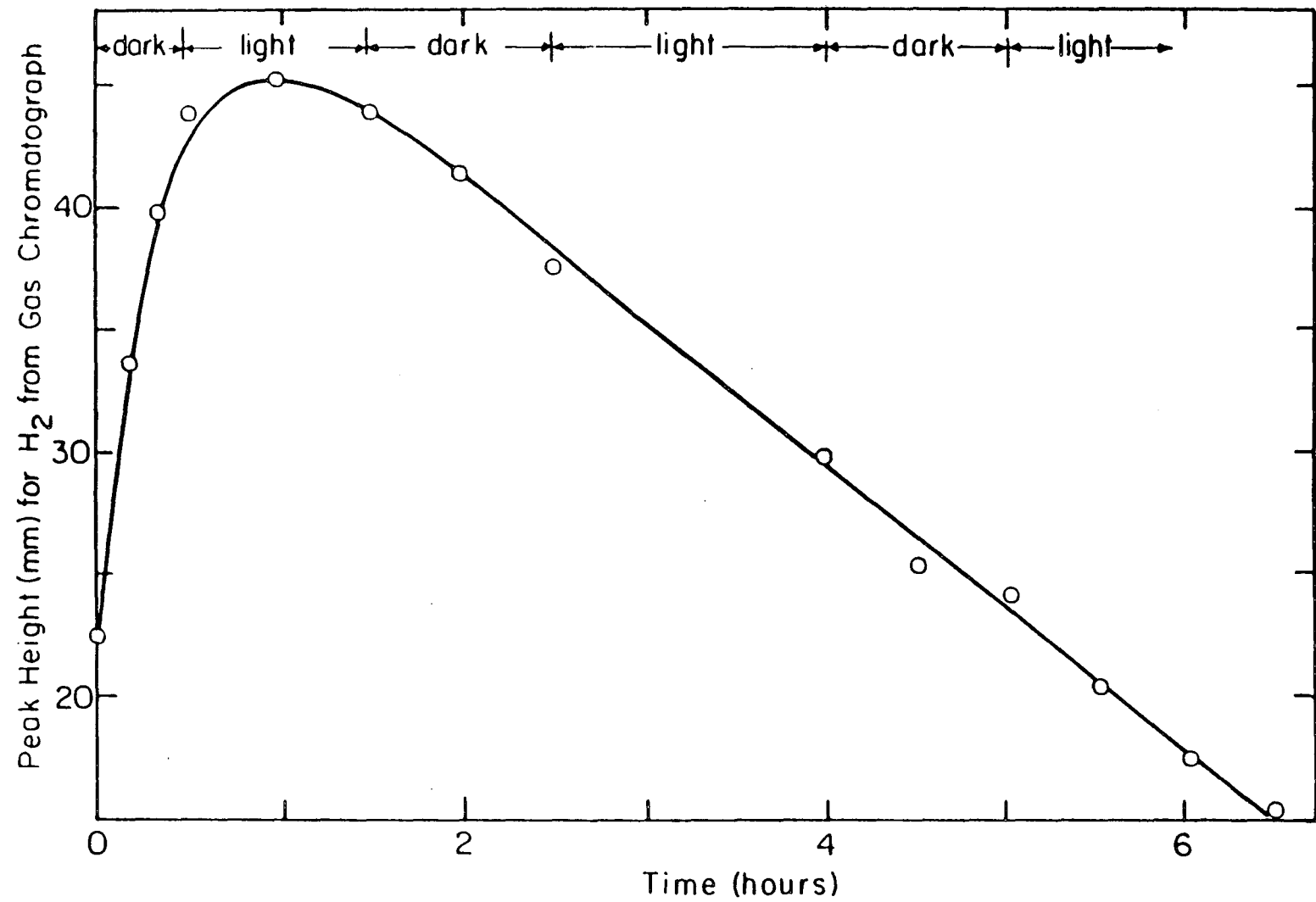
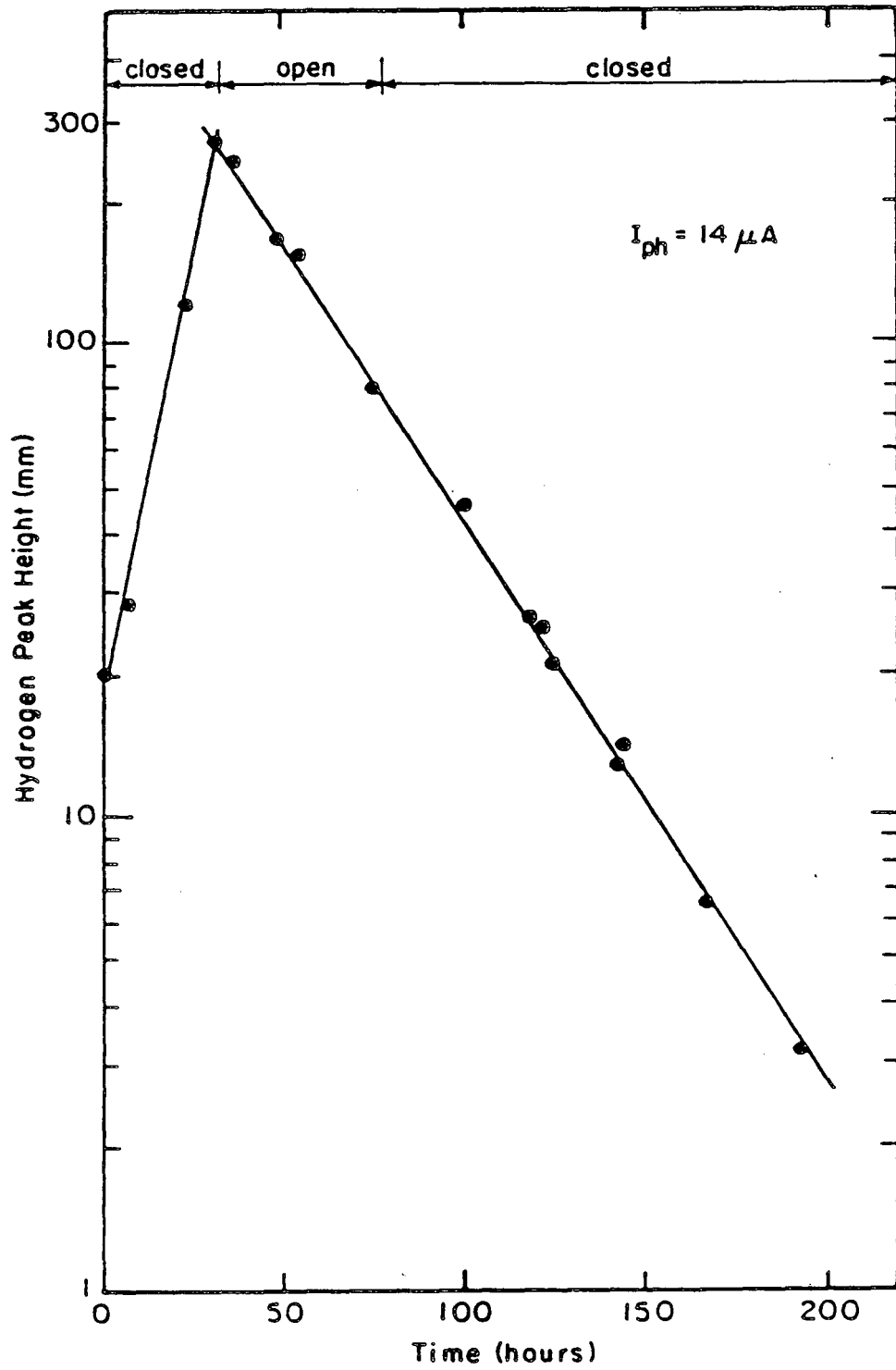


Figure 4.7.

XBL 855-6260

Hydrogen Production From a Short Circuited Assembly



XBL 855-6268

Figure 4.8.

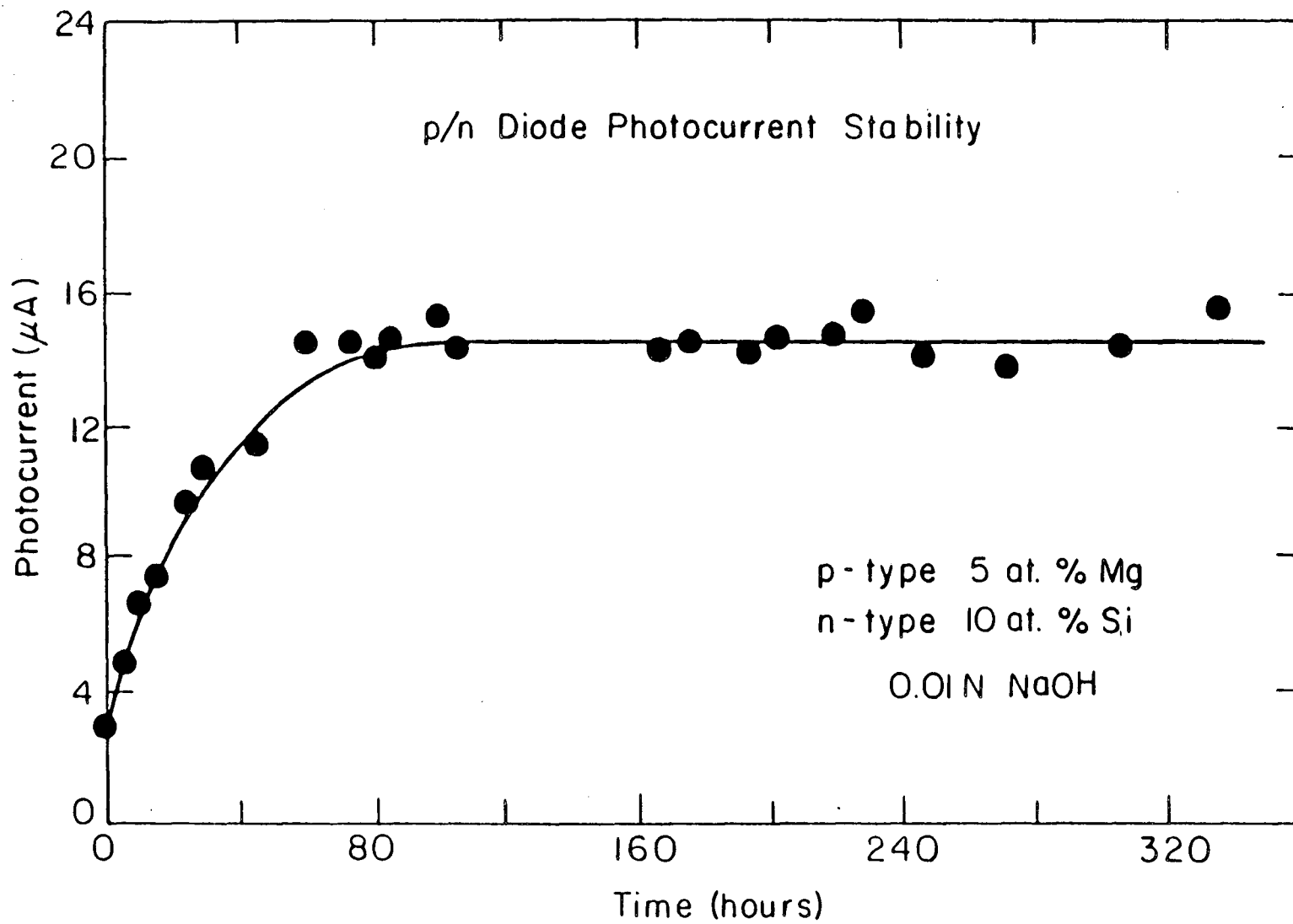


Figure 4.9.

X-ray electron Emission

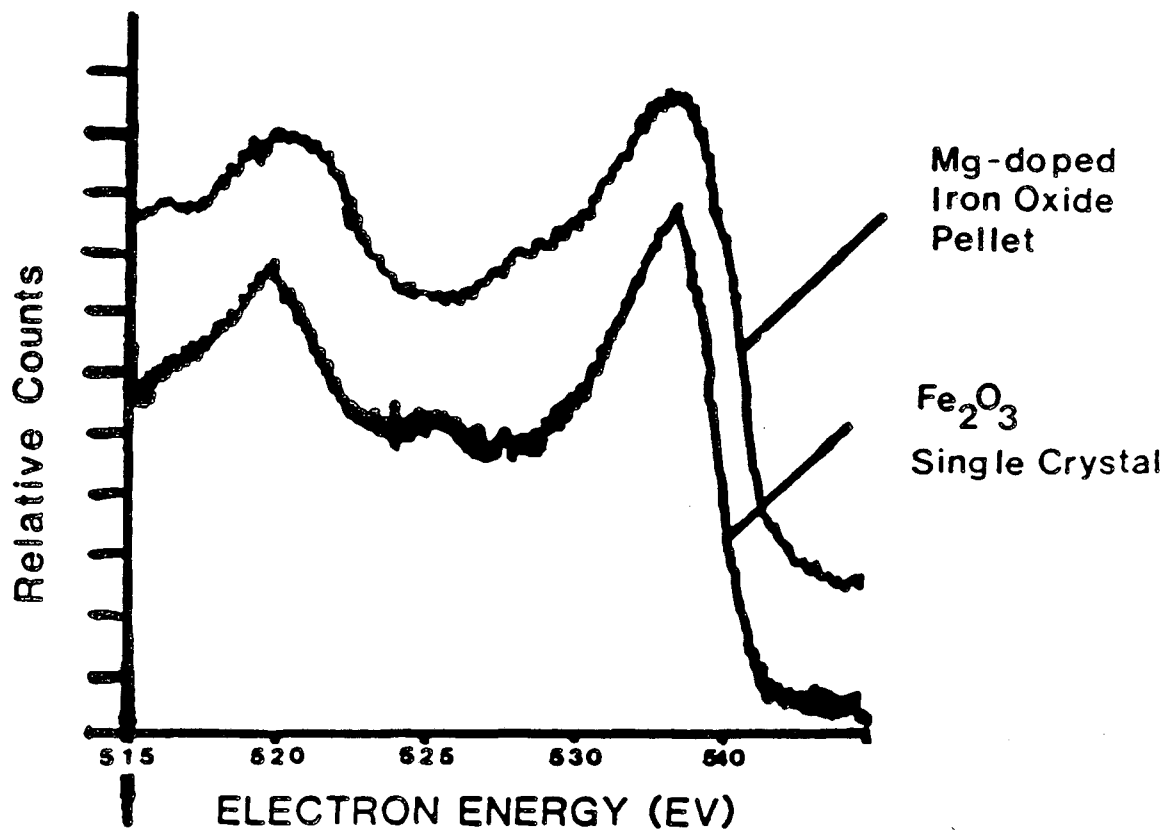
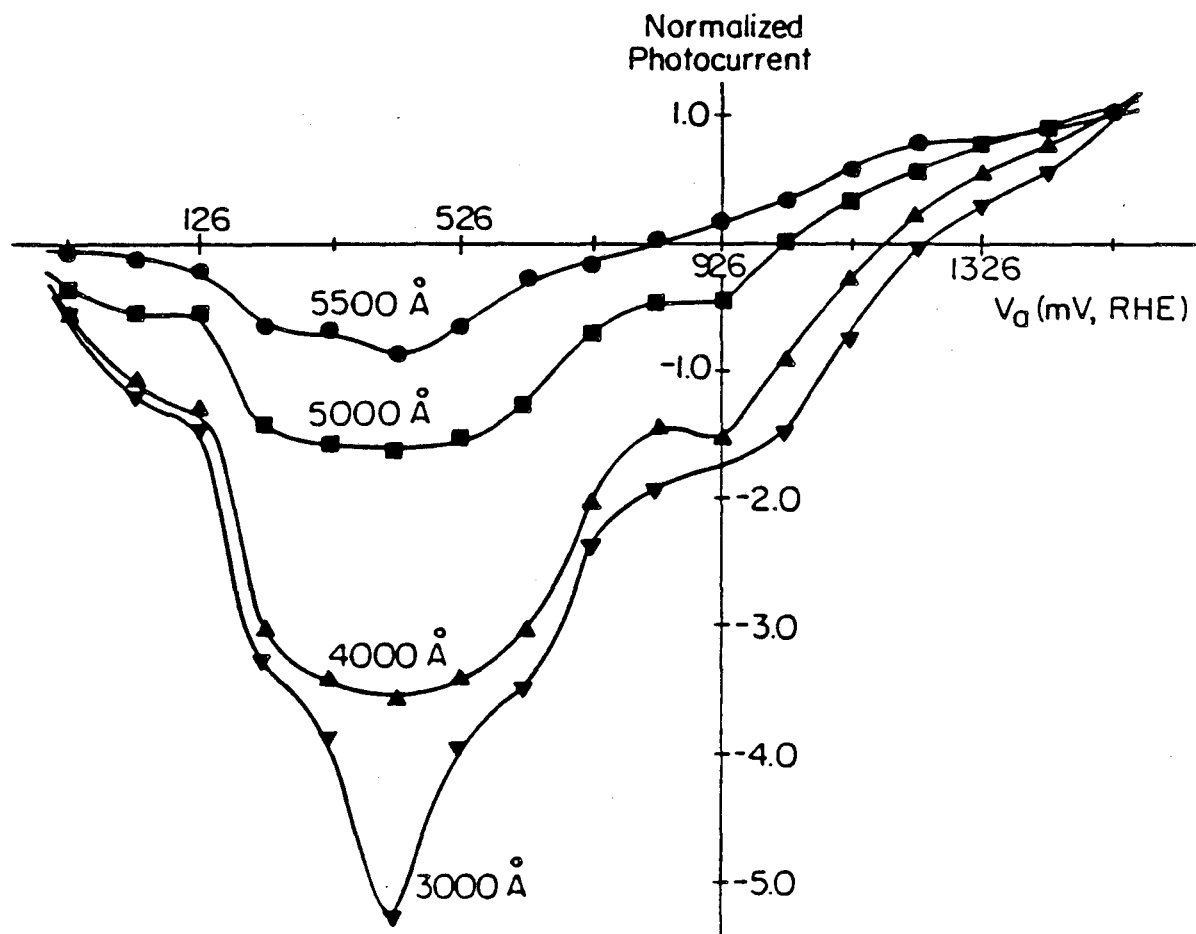


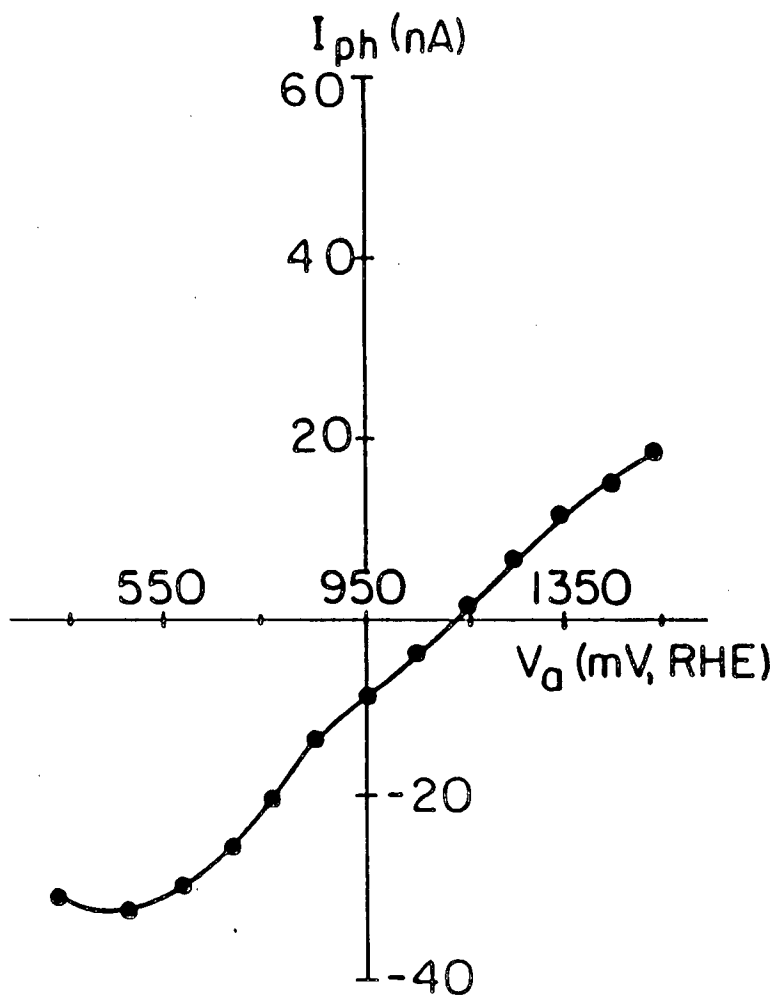
Figure 4.10.



XBL 842-6665A

Figure 4.11.

Before Surface Abrasion



After Surface Abrasion

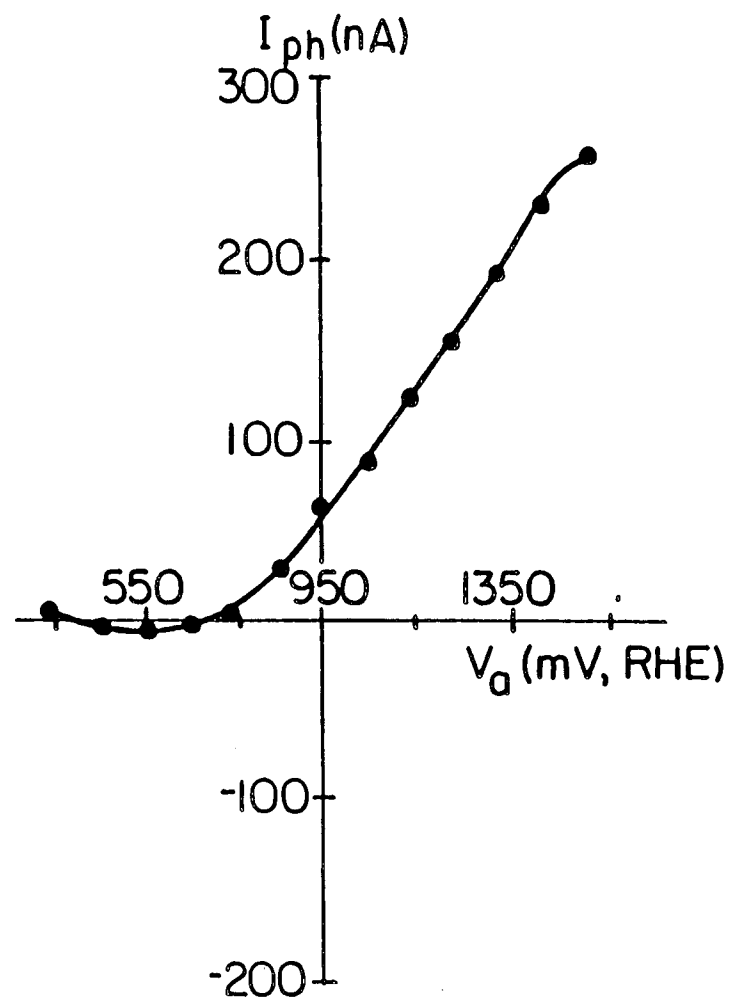


Figure 4.12.

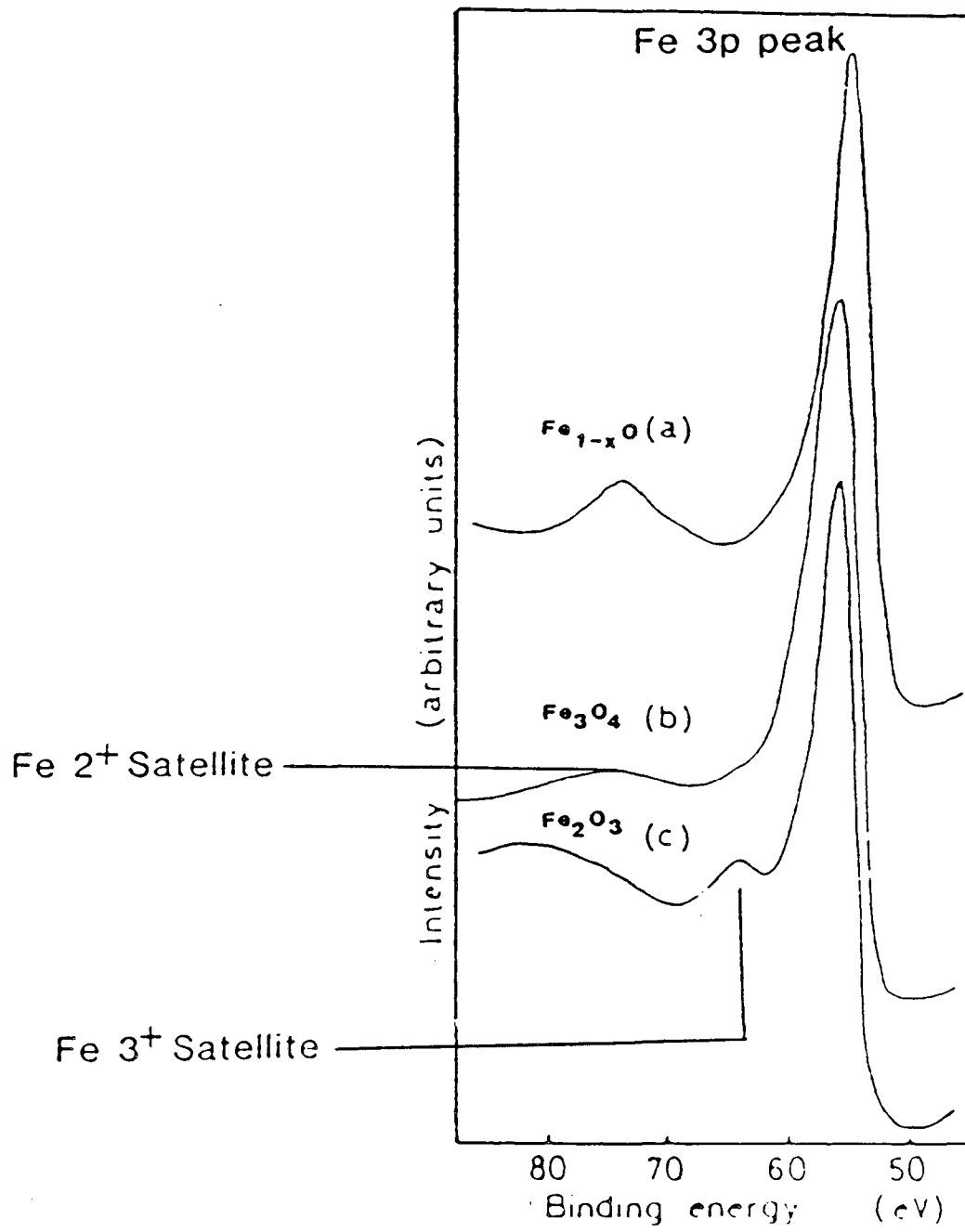
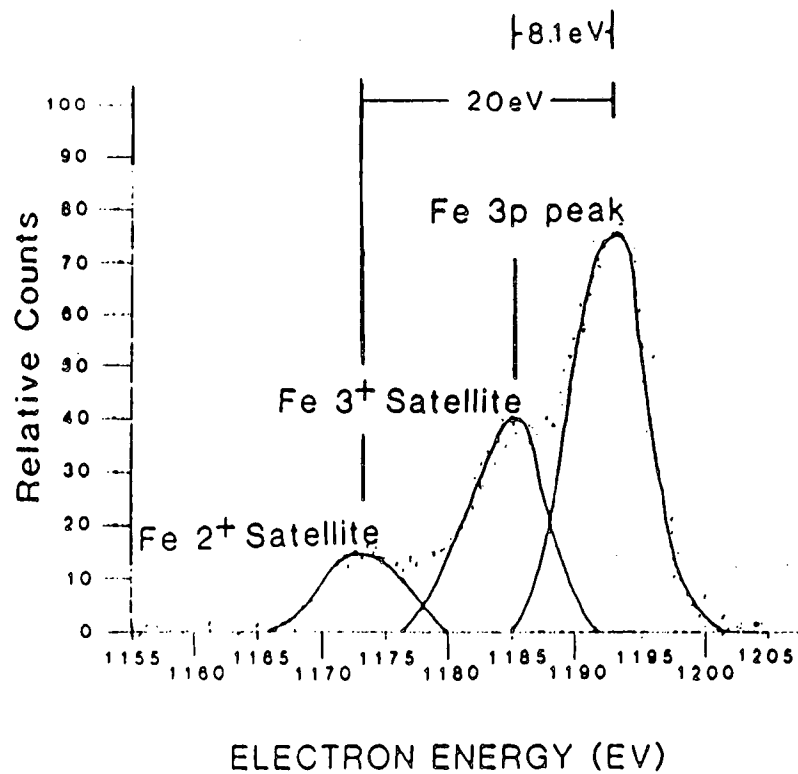
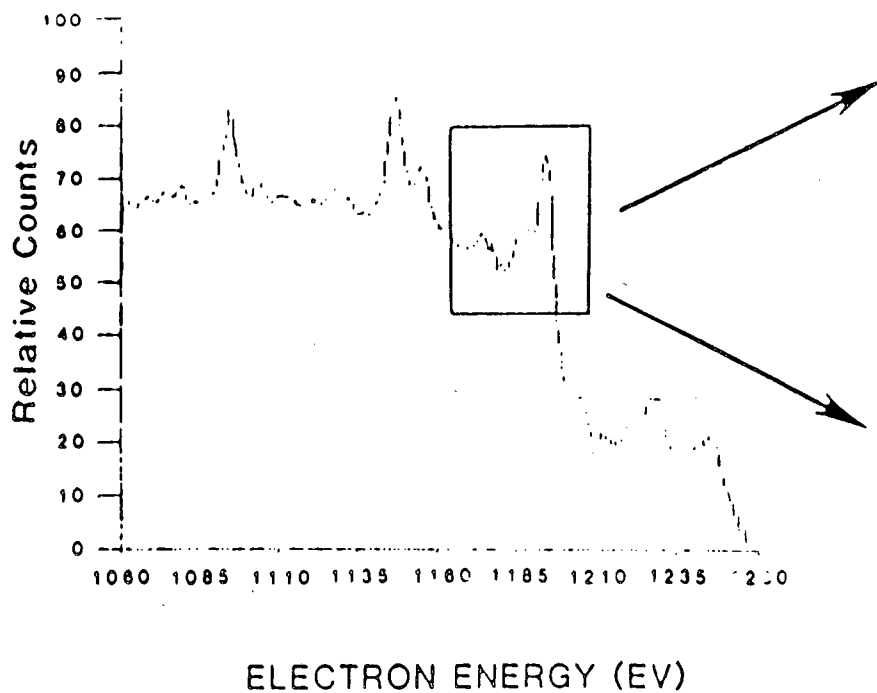


Figure 4.13.

Figure 4.14.



References

- 4.1. N.F. Mott, Proc. Roy. Soc., A171, 27 (1939).
- 4.2. W. Schottky, Z. Phys., 113, 367 (1939); 118, 539 (1942).
- 4.3. R. Shinar, J.H. Kennedy, J. Electrochem. Soc., 130, 392 (1983).
- 4.4. P. Iwanski, J.S. Curran, W. Gissler, R. Memming, J. Electrochem. Soc. 128, 2128 (1981).
- 4.5. K.G. McGregor, M. Clavin, J.W. Otvos, J. Appl. Phys., 50, 369 (1979).
- 4.6. M.A. Butler, D.S. Ginley, Chem. Phys. Letters, 47, 319 (1977).
- 4.7. R.H. Wilson, J. Appl. Phys., 48, 4292 (1977).
- 4.8. J.R. Wilson, J. Electrochem. Soc., 128, 2369 (1981).
- 4.9. C.N. Sayers, N.R. Armstrong, Surf. Sci., 77, 301 (1978).
- 4.10. J.B. Goodenough, Metallic Oxides, in Progress in Solid State Chemistry, ed. by H. Reiss (Pergammon Press, N.Y. 1971) 1981.
- 4.11. C.M. Srivastava, Bull. Mat. Sci., 5 247 (1983).
- 4.12. P. Merchant, R. Collins, K. Dwight, A. Wold, J. Sol. St. Chem., 27, 307 (1979).
- 4.13. L.a. Marusak, R. Messier, W.B. White, J. Phys. Chem. Solids, 41, 981 (1980).
- 4.14. J.A. Tossell, D.J. Vaughan, Nature, 246, 42 (1973).
- 4.15. D.E. Scaife, Solar Energy, 25, 41 (1980).
- 4.16. "Photoelectrochemistry, Photocatalysis and Photoreactors", NATO Advanced Science Study Institute, series C, ed. M. Schiavello, Erice, Trapani, Italy, 1984, pp. 39, 107, 155.
- 4.17. K.D. Sieber, C. Sanchez, J.E. Turner, G.A. Somorjai, J. Chem. Soc., Faraday Trans. I, 81, 1263 (1985).

- 4.18. C. Sanchez, M. Hendewerk, K.D. Sieber, G.A. Somorjai, J. Solid State Chem. 61, 3377 (1986).
- 4.19. K.G. McGregor, M. Calvin, J.W. Otvos, J. Appl. Phys., 50, 369 (1979).
- 4.20. P. Iwanski, J.S. Curran, W. Gissler, R. Memming, J. Electrochem. Soc., 128, 2128 (1981).
- 4.21. R. Shinar, J.H. Kennedy, J. Electrochem. Soc., 130, 392 (1983).
- 4.22. J.H. Kennedy, K.W. Frese, Jr., J. Electrochem. Soc., 125, 723 (1978).
- 4.23. S.M. Wilhelm, K.S. Yun, L.W. Ballenger, N. Hackerman, J. Electrochem. Soc., 126, 419 (1979).
- 4.24. Advances in Catalysis, Vol V, Academic Press, N.Y.,N.Y. (1953) p. 30.
- 4.25. N.D. Spencer, R.C. Schoonmaker, G A.Somorjai, J. Cat., 74, 129 (1982).
- 4.26. M. Khudar, personal communication. Preliminary results from reduced powder iron oxides indicate that the presence of a small amount of Fe° is necessary for the production of ammonia from nitrogen and water. It is also thought that the iron is not oxidized in the process (bulk x-ray diffraction spectra of powder were taken before and after the reaction).
- 4.27. R.C. Weast, ed., CRC Handbook of Chemistry and Physics, 51st ed. (CRC Press, Cleveland, 1970-71) p. B-116.
- 4.28. L. Yeh, N. Hackerman, J. Electrochem. Soc., 124, 833 (1977).
- 4.29. K. Sieber, private communication. Doping single crystals with Mg gave crystals with the resistivity of pure Fe_2O_3 .

- 4.30. T.A. Carlson, Photoelectron and Auger Spectroscopy, Plenum Press, N.Y. and London, 1975.
- 4.31. P.F. Kane, G.B. Larrabee, Characterization of Solid Surfaces, Plenum Press, N.Y. 1974.
- 4.32. M. Oku, K. Hirokawa, J. Solid State Chem., 30, 45 (1979).

Chapter Five

An XPS, UPS, TDS Study of Water and K on Ge-doped Single Crystals

There have been theoretical (REF 5.1,5.2) and experimental (REF 5.3-5.5) studies of water adsorbed on iron and its oxides by photoelectron methods. As a supplement to these studies and as a correlation to water photodissociation, experiments have been performed using iron oxide electrodes and several ultrahigh vacuum techniques (thermal desorption spectroscopy, ultraviolet photoelectron spectroscopy and x-ray photoelectron spectroscopy) to study the reaction of H_2O with stoichiometric and reduced iron oxide crystals. K has been added to the system to simulate the presence of alkali metals in the electrolyte solutions used for the water photodissociation process.

Experimental

All of the UHV experiments were conducted on Ge-doped $\alpha-Fe_2O_3$ crystals grown by CVD as described in the experimental section. The crystal orientation is the (001) basal plane of the corundum hexagonal unit cell. The crystals show very nice hexagonal LEED patterns without sputtering or annealing them beforehand (Figure 5.1). These Ge-doped crystals have been extremely well characterized and have been shown to be identical in nature to pure $\alpha-Fe_2O_3$ in all respects, including the bandgap, and electrochemical properties (REF 5.6). The only exception is that the conductivity of the Ge-doped crystals is much higher (1 Ωcm) than for pure $\alpha-Fe_2O_3$ ($10^6 \Omega cm$) which is advantageous for studies with electron spectroscopies.

Ultra High Vacuum Surface Analysis

In the ultra high vacuum chamber spectroscopic techniques are used to study only the outermost (10-100 Å) layers of the surface. These spectroscopies involve the detection of low energy electrons which are ideally suited for surface studies because the mean free path of an electron penetrating through solids is only a few layers. Figure 5.2 shows the dependence of the electrons mean free path as a function of their kinetic energy. Electrons with energies between 10 and 1000 eV are used for surface analysis via many different techniques, including x-ray photoelectron spectroscopy, ultraviolet photoelectron spectroscopy, Auger electron spectroscopy, and low energy electron diffraction. Temperature programmed mass spectrometry was also used.

Surface analytical experiments were carried out in a homemade ultra high vacuum chamber (Figure 5.3) pumped by a high speed oil diffusion pump using Santovac 5 oil (vapor pressure less than 10^{-10} torr at room temperature) and equipped with a liquid nitrogen cold trap to facilitate pumping H_2O , CO , and CO_2 . The base pressure of the chamber was 2×10^{-10} torr after heating the walls of the chamber to $230^\circ C$ for 24 hours. A typical mass spectrum of the residual gases in the chamber after a bakeout ($P = 10^{-10}$ torr) (Figure 5.4) shows that the gases are primarily H_2O , CO , and CO_2 .

The chamber is equipped with instruments for low energy electron diffraction (LEED), (Physical Electronics Model 11-020), x-ray photoelectron spectroscopy (XPS), (Physical Electronics Models 20-095, 04-151), ultra violet photoelectron spectroscopy (UPS),

(GCA/McPherson Model 630), Auger electron spectroscopy (AES), (Physical Electronics Models 11-010, 11-500M, 20805), quadrupole mass spectrometry, (UTI Model 100C) and argon ion bombardment, (Physical Electronics Model 20-045). The electron detector used was a Physical Electronics Model 15-25G double pass cylindrical mirror analyzer.

The chamber is also equipped with a separate small chamber which was capable of functioning either as an electrochemical cell or as a means of transferring samples to the UHV chamber without letting the system up to air. The cell was pumped to 1×10^{-7} torr with a small diffusion pump backed by a mechanical pump. The transfer mechanism was unique (designed by Keith Franck) and was leak tight to 1×10^{-9} torr. Samples transferred into the UHV system were heated by a tungsten button heater mounted on the manipulator. Although the electrochemical cell on the UHV system was never used as such, it could provide the doorway to a new frontier in which the fields of electrochemistry and surface science would be tightly interwoven.

X-ray Photoelectron Spectroscopy

X-ray photoelectron spectroscopy (XPS) is used to study the composition of the near surface region ($<100\text{\AA}$) and more importantly to obtain information concerning the oxidation states of the atoms comprising this surface region. The principle of XPS is the excitation of electrons from the core levels of atoms into vacuum by means of x-ray irradiation as shown schematically in Figure 5.5. Peak positions were determined by calibrating the entire spectra with respect to the C(1s) peak. It has been

experimentally determined that the XPS peak binding energy for adventitious carbon is 284.5 eV (REF 5.7). All of the XPS data reported here were obtained using the Mg $K\alpha$ x-ray line of 1256.3 eV energy. The x-ray source consisted of a water cooled copper anode coated with magnesium. The anode is bombarded with electrons emitted from the source cathode which excite the Mg atoms on the anode surface. Radiative relaxation of the metal atoms produces the characteristic x-rays used to ionize a sample for XPS analysis. The x-ray power supply was operated at 400 Watts (10 keV, 40 mA).

The ejected photoelectrons have a kinetic energy of

$$E_{kin} = h\nu - E_B - \phi_{spec}$$

where $h\nu$ is the energy of the incident x-rays and E_B is the binding energy of the ejected electron, and ϕ_{spec} , the spectrometer work function, is a constant (~4eV). These electrons are detected via a double pass cylindrical mirror electron energy analyzer (Figure 5.6). The electrons are retarded to a constant energy (pass energy) by a variable potential applied to the grid at the front of the detector. This allows only electrons of a determined energy to be filtered and focussed into the electron multiplier (a channeltron) so that the detection resolution is constant throughout the kinetic energy range of the incoming electrons. The resolution is determined by the pass energy such that

$$\Delta E/E = \text{constant} = 0.007$$

where E is the kinetic energy of the electrons entering the spectrometer ($E = E_{pass} = \text{constant}$) and ΔE is the resolution. The resolution (full width half maximum of the peak detected) for different pass energies is shown in Table 5.1.

TABLE 5.1

<u>ΔE (resolution)</u>	<u>Pass Energy</u>
0.07	10
0.14	20
0.35	50
0.70	100
1.40	200

Ultraviolet Photoelectron Spectroscopy

Ultraviolet photoelectron spectroscopy is used to study the density of states and the valence structure in materials. The principles of ultraviolet photoelectron spectroscopy (UPS) differ from those described above for XPS only in that the excitation source is a He lamp which gives off ultraviolet radiation of 21.2 eV energy. Since the excitation source energy is now much smaller, the electron vacancies which are created in the atoms are valence shell electron vacancies as opposed to core level vacancies produced by x-rays. In the UV lamp, bound atomic electrons of He are excited by electric discharge in a continually flowing gas stream. The photoemission spectrum of the He vacuum-UV light source is then the result of the deexcitation of those excited atoms or ions.

One important parameter which can be studied with UPS is the work function of a material. The work function of a solid changes quite noticeably when the surface dipole is changed either by adsorbing dipolar molecules on the surface or by removing elements from the bulk of a composite material. The extraction of a work function from a UPS spectrum is shown schematically in Figure 5.7. The work function is defined as the potential that an electron at the Fermi level must overcome to reach the level of zero kinetic energy in the vacuum. It can be expressed, then, as the difference between the vacuum level and the Fermi level of the sample

$$e\phi = E_{vac} - E_f.$$

For semiconductors the onset of emission in the UPS spectrum corresponds to the valence band edge and not the Fermi level. Figure 5.8 gives an energy level diagram for photoelectron

spectroscopy (REF 5.8). Using this figure it is easy to see that

$$h\nu = E_{kin} + E_B + e\phi_{spec}.$$

One can also see that when the binding energy, E_B , is zero that

$$h\nu = E_{kin} + e\phi_{spec}$$

so that the kinetic energy is maximized when an electron is being removed from the Fermi level. Therefore the difference between the photon energy and the Fermi level (since $E_F = E_{kin}$ (maximum) when E_B is zero) is the work function of the spectrometer. The work function of the sample is obtained by looking at the onset of the secondary electron emission. Figure 5.7 depicts a schematic density of states for a sample and the distribution of secondary electrons (electrons which have undergone multiple inelastic scattering processes). An electron with just enough energy to leave the sample and reach the vacuum level has zero kinetic energy. If however, there is an additional potential at the surface which the electron must overcome to escape the sample (the work function) then the onset of emission of electrons from the sample will begin at a higher energy and the secondary electron distribution, as shown in Figure 5.7, will be cut off. Therefore changes in the work function of a sample can be measured by measuring the change in the onset of the zero kinetic energy secondary electron emission.

The crystal was biased with -11.0 V during the UPS scans in order to observe the onset of the secondary electron emission. The work function of the spectrometer was assumed to be constant, so that changes in the work function of the sample were obtained from the shift in the onset of the secondary electron emission. Since the Fermi level of a semiconductor does not coincide with the energy

of the highest occupied level of the material, the binding energy scale has been chosen so that zero binding energy is at the top of the valence band. The valence band energy was assumed to be constant throughout these experiments.

Auger Electron Spectroscopy (AES)

Auger electron spectroscopy is most suitable for studying the chemical composition of surfaces and to estimate absolute coverages of adsorbants. Auger electron emission occurs after the production of an electron vacancy in the core level of an atom either by x-rays (as in XPS) or electrons ranging in energy from 1-5 keV. This electron vacancy is filled by deexcitation of electrons from the outer shells, as shown in Figure 5.5. The energy released in the deexcitation is transferred by electrostatic interaction to an electron in the same atom or in a different atom. If this electron has a binding energy that is less than the energy transferred to it from the deexcitation process then it will be ejected into the vacuum leaving behind a doubly ionized atom. The ejected electron is called an Auger electron. The energy of Auger electrons is independent of the energy of the incident beam of x-rays or electrons, contrary to the electrons detected in XPS or UPS, and can be written as

$$E_{\text{Auger}} = (E_2 - E_1) - E_b - e\phi_s$$

where $E_2 - E_1$ is the energy difference between the two electronic energy levels involved in the deexcitation process and E_b is the binding energy of the ejected Auger electron.

For these experiments Auger analysis was performed using an incident electron beam of 2 keV energy and 0.2 mA emission current.

The channeltron was operated at a bias of 1.9 keV. The signal was passed through a PAR (Model HR-8) lock-in amplifier in order to obtain the derivative of the signal $dN(E)/dE$. The number of Auger electrons is small compared to the number of electrons which have undergone secondary scattering processes (Figure 5.9), so that taking the derivative of the signal enables the detection of the small Auger electron signal on top of the much larger secondary electron signal.

Argon Ion Bombardment

Because XPS, UPS, and Auger are used to investigate the outermost surface layers of a sample it is important that the surface not be covered with carbon, water, or other impurities. Ar ion bombardment was used to clean the sample surface and also to sputter off layers of the material to monitor changes as a function of depth into the sample (depth profiling). During the argon ion sputtering the argon gas pressure was maintained between 1×10^{-4} and 5×10^{-5} torr and the ion gun operated between 0.5-2 keV and 10-20 mA. When sputtering a compound, such as iron oxide, consisting of different elements, lighter elements are preferentially sputtered and metal cations are generally reduced in the process.

Low Energy Electron Diffraction

Low energy electron diffraction (LEED) yields information about the geometry of the topmost layers of solids. The technique is based on the wave nature of electrons. According to the de Broglie relationship, electrons have associated with them a wavelength λ , given by the expression

$$\lambda = h/(mv) = \sqrt{150/V}$$

h being Planck's constant, m the rest mass of an electron, v its velocity, and mv its kinetic energy. Hence, when an electron beam impinges on a crystal surface, a fraction of these electrons are elastically scattered by the atomic core potentials which may constructively or destructively interfere depending on the atomic positions, analogous to x-ray diffraction experiments (REF 5.8). Constructive scattering will occur at certain angles ϕ , which can be calculated using Bragg's equation. For normal electron beam incidence

$$\sin\phi = n\lambda/d_{h,k} = n/d_{h,k} \sqrt{150/V}$$

where n is an integer denoting the order of diffraction and $d_{h,k}$ is the distance between parallel rows of scatterers in the $[h,k]$ direction. Information about the shape and dimensions of the unit cell of adsorbates may thus easily be determined and compared with the substrate (if periodicity is present). For instance, a (2×2) adsorbate overlayer means that the chemisorbed species order on the solid surface in such a way that its unit cell has the same shape as that of the substrate, but is twice as long in both directions.

The translation of a crystal lattice structure to the fluorescent screen is shown in Figure 5.10. A monochromatic electron beam impinges on the surface at close to normal incidence, and the elastically scattered electrons are filtered using a retarding field analyzer and accelerated into the phosphorescent screen. The patterns can then be photographed through the UHV chamber viewport with a polavoid camera and appropriately identified.

Thermal Desorption Spectroscopy

Thermal desorption spectra were taken with the mass spectrometer encapsulated except for a protruding 1 mm aperture in order to localize the detection of gases to those desorbing from the sample surface rather than the sample mount. The single crystals as grown by CVD were very thin platelets which enabled us to mount them so that the temperature of the crystals could be measured very accurately during the heating cycles. The platelets were mounted on a tantalum foil smaller than the crystal size by melting a very small amount of pure indium (melting point 156°C) on the foil and placing the crystal on top of the In. All of the supports and backing were covered with Au foil, since Au is the least reactive of the metals. Although the melting point of indium is low the surface tension of the liquid is very high. Even at 1000 K the crystal, which was mounted vertically, did not fall from the Ta foil. Temperatures were recorded with a chromel-alumel thermocouple spot welded directly to the tantalum foil. Because the platelets were very thin (<1 mm) the temperature of the foil and the crystal can be assumed to be identical. An AC power supply was used to ramp the temperature of the crystal. The heating rate used for the thermal desorption experiments was 10-50 K/sec. Single thermal desorption peak spectra were recorded on an x-y recorder while multiple mass detection was accomplished using an LSI-11 computer interfaced with the UTI mass spectrometer (REF 5.9).

The phase transition of iron oxide from $\alpha\text{-Fe}_2\text{O}_3$ to Fe_3O_4 occurs at 1350 K (Figure 3.6) so that no attempts were made to heat higher than 1000 K. No In was seen by Auger or XPS to

have diffused to the front surface of the crystal even after heating to 1000 K, although we were careful to avoid such high temperatures for more than a few seconds at a time. The sample was cooled by thermal transport from the tantalum supports to a liquid nitrogen reservoir. The sample was routinely cooled to 120 K.

Gas exposures were measured using mass spectral intensities rather than ionization gauge pressure increases in some cases because of contamination of the gas inlet lines with CO. Iron oxide is almost completely inert to CO even at 130 K so that the CO did not interfere with the adsorption of other gases on the crystal surface. No attempts were made to calibrate the signal of the mass spectrometer to absolute coverages or pressures. The technique for this calibration is well described elsewhere (REF 5.10).

The desorption rate $r(t)$ from a sample of area A , is related to the partial pressure obtained using a mass spectrometer by the expression

$$r(t) = (k \times S)\Delta p$$

where k is a constant, S is the pumping speed of the system (and is assumed to be much faster than the desorption rates), and Δp is the pressure change due to the desorption. This desorption rate can also be expressed as an Arrhenius expression,

$$r(t) = \nu_n f(\theta) \exp(-E_{des}/RT)$$

where ν is the preexponential factor, n is the desorption order, $f(\theta)$ is an adsorbate coverage dependent function, and E_{des} is the activation energy for the desorption process.

If it is assumed that the temperature varies linearly with time ($T = T_0 + \beta t$), and if ν_n and E_{des} are coverage

independent, Redhead has shown that (REF 5.11)

$$E_{d_{e_s}}/(RT_p^2) = (\nu_1/\beta)\exp(-E_{d_{e_s}}/RT_p) \quad \text{1st order}$$

$$E_{d_{e_s}}/(RT_p^2) = (\nu_2/\beta)\theta\exp(E_{d_{e_s}}/RT_p) \quad \text{2nd order}$$

where T_p is the temperature of maximum desorption, β is the heating rate, and θ_0 is the initial coverage. According to this model, T_p is independent of the initial coverage for first order desorption, but it decreases with increasing θ_0 for the second order process. Therefore, the nature of the desorption process can be inferred from a T_p vs. θ_0 plot.

Data Treatment

Data for XPS, AES, and TDS was collected on a PET model 2001 Commodore computer through a home built digital/analog converting interface. Subsequent data analysis was performed either on the Pet commodore or an LSI 11. The software programs will not be described in detail here.

Oxidized and Reduced Single Crystal Surfaces: Work Function Changes

Work was done on both the stoichiometric and reduced Ge-doped α -Fe₂O₃ iron oxides. Reduced iron oxides were produced by sputtering a stoichiometric oxidized α -Fe₂O₃ crystal with the corundum structure shown in Figure 5.1 using a high Ar ion flux to the crystal. The hexagonal LEED pattern shown in Figure 5.1 was obtained from the oxidized crystal even before the crystal was cleaned and annealed. No LEED patterns were obtained after sputtering, indicating an absence of coherent surface geometrical structure. The degree of reduction was monitored by the change in the work function of the crystal as measured by UPS, and by the intensity of the shoulder observed above the valence band structure

in the same UPS spectra. A series of UPS spectra taken as the sputtering process progressed is shown in Figure 5.11. As the iron oxide crystal becomes reduced a shoulder appears above the valence band structure in the spectra. The shoulder is more easily seen in Figure 5.12 where the pure $\alpha\text{-Fe}_2\text{O}_3$ UPS spectrum has been subtracted from each of the successive plots in Figure 5.11. This peak initially grows with sputtering time and then saturates, as would be expected since Ar^+ sputtering preferentially removes oxygen from the iron oxide lattice. As the Fe concentration at the surface increases, Fe will also be removed in the sputtering process, so that there is a limit to the degree of reduction of the surface which can be achieved. A plot of the decrease in the work function with time with our sputtering arrangement is shown in Figure 5.13. Initially the work function drops rapidly as oxygen is preferentially sputtered from the surface leaving the surface with a dipole moment directed away from the surface. After nine minutes a high density of defect sites is obtained, evidenced by both a high intensity in the shoulder above the valence band in the UPS spectra and a change of almost one electron volt in the work function of the material. Continued sputtering with time does not increase the number of defect sites. When the concentration of Fe atoms at the surface becomes high, since oxygen is removed first, the Fe atoms will also begin to be removed so that a steady state concentration of defect sites is obtained. This is shown by the constant work function at the minimum value measured after nine minutes of sputtering. The crystal was reoxidized to its stoichiometric form at 600 K in 5×10^{-6} torr of oxygen.

A number of different reduced states of the iron oxide could be reproducibly produced by sputtering for 15 minutes and subsequently annealing to different temperatures. As can be seen in Figure 5.14, there is an initial abrupt change in the work function as the crystal is annealed. This initial change is probably due to the rearrangement of the surface atoms to produce an oxidized layer on the surface of the crystal either by diffusion of Fe into the bulk or oxygen out of the bulk. With the crystal held at one temperature for 30 minutes, little or no further changes in the work function were observed with time. This indicates that these reduced oxide species are very stable, which is supported by experiments in which reduced iron oxides are used in aqueous solutions for long periods of time and show no alteration of the iron oxide valence states (REF 5.12 - 5.15).

XPS spectra of the single crystal in the stoichiometric form and the reduced form are compared to an iron foil in Figure 5.15. The relative position of the $2p_{3/2}$ line for Fe^{2+} as found by other authors (REF 5.16 - 5.19) is shown by the vertical lines. The reduced sample was produced by sputtering for several hours with Ar^+ . The data show that the sample contains very little if any Fe^0 so that the small UPS signal near the Fermi level corresponds primarily to Fe^{2+} inclusions in the surface layers of the iron oxide.

Thermal Desorption of Water from Oxidized and Reduced Iron Oxide

Figures 5.16 and 5.17 show two series of TDS spectra for H_2O desorption from a completely oxidized (stoichiometric) and a partially reduced Ge-doped $\alpha-Fe_2O_3$ single crystal. The data

are characterized by a single peak which shifts to higher temperature as the coverage increases. The shift of the single desorption peak to higher temperatures with increasing coverage coupled with the exponential form of the leading edge of the TDS spectrum clearly indicates a zero order desorption process as would be expected for the multilayer growth of physisorbed water.

Assuming that the thermal desorption rate is slower than the pumping speed of the diffusion pump, the intensity of the mass spectral peak can be related to the rate of desorption of the H₂O molecules from the surface. With this, one can use an Arrhenius plot of the mass spectral intensity vs. 1/T to calculate an activation energy for the desorption process (Figure 5.18). The activation energy for the desorption was calculated to be 11.8 kcal/mol which is very close to the sublimation energy of ice (12.2 kcal/mol).

No additional water desorption peaks were observed at higher temperatures indicating that the chemisorption of water does not occur on the basal plane (001) of α -Fe₂O₃ iron oxide. The absence of a monolayer desorption peak and the single peak spectra for the oxidized iron oxide surface are strong indications that lateral interactions between H₂O molecules are comparable to or stronger than H₂O-substrate interactions. At very low coverages two peaks were observed on the sputtered crystal, whereas only a single desorption peak was detected on the fully oxidized crystal. The additional peak seen in the sputtered surface spectrum at low coverages may correspond to a slightly stronger substrate-H₂O interaction due to the underlying reduced Fe species, even though these reduced iron atoms are not exposed to the surface.

Iron oxides are being used as catalysts for many reactions involving both gas and liquid phase water. In fact, often times these iron oxides perform best when the oxide has been prereduced (REF 5.12). It is somewhat hard to believe that these prereduced species indeed react catalytically rather than stoichiometrically in a highly oxidizing environment such as that of a NaOH /H₂O solution at pH = 12. We have shown that many reduced states of iron oxide are quite stable in vacuum even at relatively high temperatures (Figure 5.14).

Direct evidence that only the first few layers of the freshly sputtered surface are oxidized by cleavage of the O-H bond from adsorbed water molecules is given by the H₂ thermal desorption data shown in Figure 5.19, and the UPS data shown in Figure 5.20. H₂ was monitored in the mass spectrometer after the adsorption of multilayers of water on both the sputtered and oxidized crystals. No H₂ desorption was observed for the stoichiometric oxidized crystal between 120 K and 1000 K. The lack of the water recombination peak and an H₂ peak suggests that water only physisorbs molecularly on the fully oxidized surface. In the UPS spectra no peaks corresponding to either H₂O or OH⁻ were present indicating that there was no molecular water or OH⁻ species on the surface above 300K.

On the sputtered surface, however, quite different results were obtained. The initial desorption of water from the surface yielded both a multilayer molecular desorption peak and a H₂ peak. The hydrogen peak is very broad, stretching from 160 K to 600 K. The crystal was subsequently cooled and a second thermal desorption

spectrum was taken under the same conditions and exposure as for the initial run. No H_2 was seen desorbing from the surface of the crystal. Thus, the presence of oxygen vacancies and consequently reduced iron species, initiates dissociative adsorption of water on the iron oxide surface. Only the Fe^{2+} species in the outermost atomic plane can adsorb water dissociatively. Subsurface Fe^{2+} species, although stable, are not contributing to the dissociative chemisorption of H_2O . Subsequent annealing cleaves the O-H bond. The oxygen is incorporated into the iron oxide surface layer and the H atoms recombine to form H_2 gas molecules. In the UPS spectra, the shoulder above the valence band edge which corresponds to reduced Fe species is still present after the surface layer has been oxidized. With the small escape depth of valence level electrons, these species would not be detected had more than the top layer of the reduced oxide been oxidized.

Interactions of Water with Iron Oxide Single Crystals

After adsorption of multilayers of water, UPS spectra were recorded as the temperature of the crystal was stepped through the thermal desorption range from 120 K to 1000 K. The spectra are shown in Figure 5.21, 5.22. For the oxidized crystal (Figure 5.21), it is easy to see that at low temperatures (<180 K) multilayers of water are adsorbed on the surface. The substrate peaks are weakly visible but the predominant features at 7.4, 10.6, and 13.7 eV binding energy correspond to adsorbed multilayers of water. At 120 K, the UPS curves show the presence of water induced features (Figure 5.21, bottom curve). Only the peaks due to the $1b_1$ and $3a_1$ molecular orbitals are observed clearly. The $1b_2$ peak is

obscured by the secondary electron peak. UPS curves after the growth of multilayers of ice show all three of the ice peaks clearly (Figure 5.22, bottom curve). After heating the oxidized crystal to 190 K all of the water features in the UPS spectra disappear. Concomitantly, no water desorption peaks were observed in the thermal desorption experiments above 190 K (Figure 5.23). All of the water desorbed below 190 K.

The spectra for the sputtered crystal are shown in Figure 5.22. These spectra were taken directly after the crystal was sputtered while cooled to 120K. After the sputtering, water was adsorbed and the UPS spectra were taken during the initial heating ramp. The same exposure of water was used as for the oxidized crystal. As can be seen by the water adsorption UPS spectrum (bottom curve, Figure 5.22) more water adsorbs on the sputtered crystal than on the oxidized crystal for the same exposure. All three of the ice peaks can be seen quite clearly. The thickness of the ice film must be at least 20Å to completely suppress the underlying Fe_2O_3 spectrum. Upon heating, the peak at 10.6 eV slowly decreased in intensity. After the desorption of the molecular water at 190 K, this peak shifts to higher binding energy by 0.5 eV. This result seems to indicate that OH species are now present on the surface. Similar shifts in going from H_2O to OH have been observed by other authors (REF 5.20,5.21). The 10 eV peak disappeared completely only above 370 K. Continued heating produced no additional changes. It is also noteworthy to mention that again the Fe^{2+} shoulder near the valence band edge did not appreciably decrease until very high temperatures were reached, in agreement with

previously reported data (REF 5.22).

Water Interactions on a K Covered Surface

K was deposited on the surface of the crystal via a K source heated by a DC power supply. Coverages were monitored by Auger peak to peak ratios of the K(252) to Fe(651) peaks. It was possible to deposit multilayers of K with a K/Fe ratio as high as $K/Fe = 36$. These layers were easily desorbed upon heating to 350 K. The coverage of K (K_{252}/Fe_{651}) as a function of temperature is shown in Figure 5.24. After the initial desorption of the K multilayers at ~350 K the remaining K ($K_{252}/Fe_{651} \sim 6$) could not be removed with heating. This K layer was easily removed by sputtering, however, indicating that the K does not penetrate into the bulk even at very high temperatures. This is an interesting phenomenon and is possibly indicative of the formation of a compound between the K and the iron oxide. K and iron oxide have been known to form a $K_2O \cdot Fe_2O_3$ compound similar to $K_2O \cdot Al_2O_3$ compounds (REF 5.23,5.24).

The coadsorption of water and K on the Ge-doped single crystals of iron oxide was also studied. While at 120 K, the single crystal was first sputtered to produce the oxygen vacancy defect sites, and then the K was adsorbed. A K/Fe ratio of ~1 was used in order to have a submonolayer coverage leaving some of the iron oxide surface area exposed.

H_2 thermal desorption spectra after water adsorption on the crystal with and without K are shown in Figure 5.25. The thermal desorption spectrum showed only one low temperature H_2O peak and two broad H_2 peaks, one at ~260 K and one at ~410 K. The high

temperature peak is equivalent to the H_2 peak observed from the initial thermal desorption of water from the sputtered crystal without K adsorbed on the surface. The low temperature peak can then appropriately be assigned to the desorption of H_2 as the KOH dissociates to form K_2O or $K_2O \cdot Fe_2O_3$ and the H desorbs to the gas phase as H_2 molecules. This is supported by Auger data (Figure 5.25). The K/Fe ratios before and after the thermal desorption are the same. This demonstrates that the K does not desorb or penetrate into the bulk of the iron oxide crystal. The O/K and O/Fe ratios increased which is consistent with the formation of both a potassium oxide and the filling of the oxygen vacancies in the iron oxide lattice.

Again, the appearance of a single multilayer peak is not surprising since one would not expect water to desorb from K, so that there is no monolayer peak either from the iron oxide or from the K. The lack of any additional H_2O desorption peaks with the coadsorption of K is not surprising since the basal plane (001) of $\alpha-Fe_2O_3$ iron oxide is so inert. However, this is not inconsequential since some reaction systems which involve iron oxide catalysts also involve alkali metal hydroxide solutions such as the photodissociation of water with $SrTiO_3$ single crystals (REF 5.25) or with iron oxides (REF 5.26). In the $SrTiO_3$ case it was also shown that the presence of different alkali species played no role in the overall reactivity of the system.

Conclusions

- 1) The basal plane of $\alpha\text{-Fe}_2\text{O}_3$ is extremely inert. Water physisorbs only as ice at low temperatures and desorbs in the range of 175 to 200 K.
- 2) Argon ion sputtering produces oxygen vacancies that expose mostly Fe^{2+} species and lower the work function of the surface.
- 3) Surface Fe^{2+} species are very unstable and disappear into the subsurface layers rapidly upon heating above 375 K. The subsurface Fe^{2+} species are stable at temperatures up to 775 K, for extended periods of time (> 30 minutes).
- 4) Only surface Fe^{2+} species chemisorb H_2O strongly to produce OH species that decompose to give H_2 upon heating.

Figure Captions

- Figure 5.1. A) Model of the corundum (001) structure. Solid circles represent Fe^{3+} ions, Open circles are the first layer of O^{2-} ions, shaded circles are the second layer of O^{2-} ions. B) LEED pattern of Nb-doped Fe_2O_3 single crystals. $E_{\text{beam}} = 102$ eV.
- Figure 5.2. Electron mean free path correlation to electron kinetic energy.
- Figure 5.3. UHV analytical chamber interfaced with sample transfer cell/electrochemical cell.
- Figure 5.4. Mass spectrum showing residual gas content in the UHV system after bakeout.
- Figure 5.5. Auger and XPS photoionization processes.
- Figure 5.6. Schematic diagram of the cylindrical mirror analyzer detector.
- Figure 5.7. Secondary electron emission and sample density of states. Work function measurements from changes in the onset of the secondary electron emission in UPS.
- Figure 5.8. Schematic depiction of the photoionization process.

- Figure 5.9. Energy distribution of Auger electrons and secondary electrons scattered from a sample.
- Figure 5.10. Translation of a crystal lattice structure to a fluorescent screen (Low Energy Electron Diffraction).
- Figure 5.11. UPS spectra taken with successive sputtering of a Ge-doped iron oxide single crystal.
- Figure 5.12. UPS difference spectra (sputtered - fully oxidized) with sputtering time.
- Figure 5.13. Work function changes with time (measured by UPS) as a Ge-doped iron oxide single crystal sputtered with Ar.
- Figure 5.14. Measured changes in work function after sputtering a stoichiometric $\alpha\text{-Fe}_2\text{O}_3$ single crystal for 15 minutes and subsequently annealing to 100, 200, 300, 400 and 500°C in vacuum..
- Figure 5.15. XPS spectra depicting valence states of iron.
- Figure 5.16. A series of thermal desorption spectra of H_2O from an oxidized stoichiometric iron oxide single crystal.
- Figure 5.17. A series of thermal desorption spectra of H_2O from

partially reduced iron oxide single crystal.

Figure 5.18. Arrhenius plot derived from thermal desorption data to obtain the heat of desorption of water from iron oxide.

Figure 5.19. Sequential thermal desorption spectra of H_2 from a partially reduced iron oxide.

Figure 5.20. UPS spectra taken after the desorption of water from a freshly sputtered (reduced) iron oxide.

Figure 5.21. UPS spectra taken after water adsorption on oxidized Ge-doped iron oxide single crystals. The temperature was stepped from 120 K to 760 K.

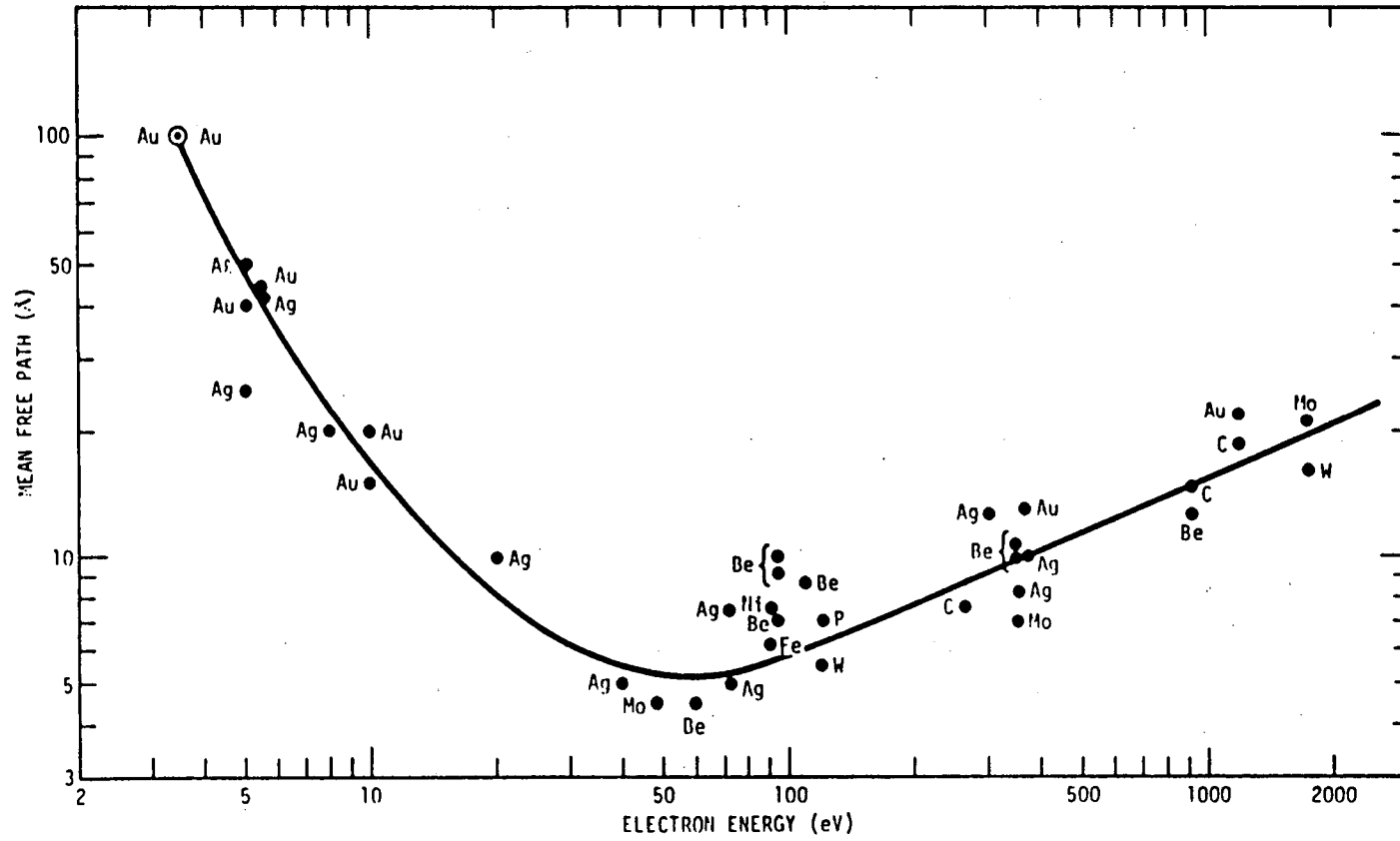
Figure 5.22. UPS spectra taken after water adsorption on sputtered Ge-doped iron oxide single crystals. The temperature was stepped from 120 K to 760 K.

Figure 5.23. Thermal desorption spectrum of H_2O from 150 K to 800 K.

Figure 5.24. H_2 thermal desorption from a Ge-doped iron oxide crystal. — sputtered + K ----- sputtered

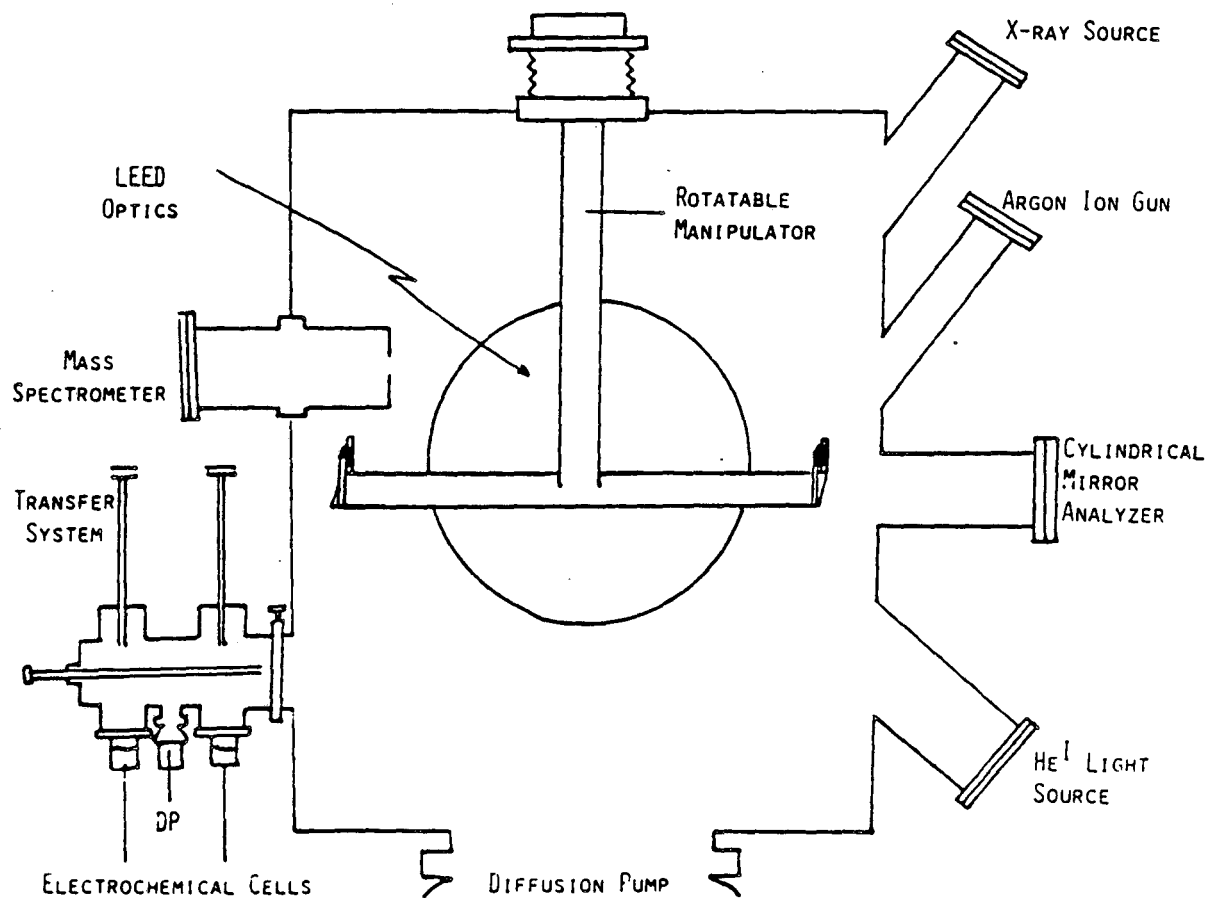
Figure 5.25. Auger peak to peak ratios of the K/Fe ratio as the crystal temperature was ramped from 120 K to 1000 K.

Figure 5.2.



XRI. 733-5917

ULTRA HIGH VACUUM CHAMBER
FOR PHOTOCATALYTIC SURFACE STUDIES



XBL 8410-4124

Figure 5.3.

Mass Spectrum Residual Gases at 1×10^{-9} Torr

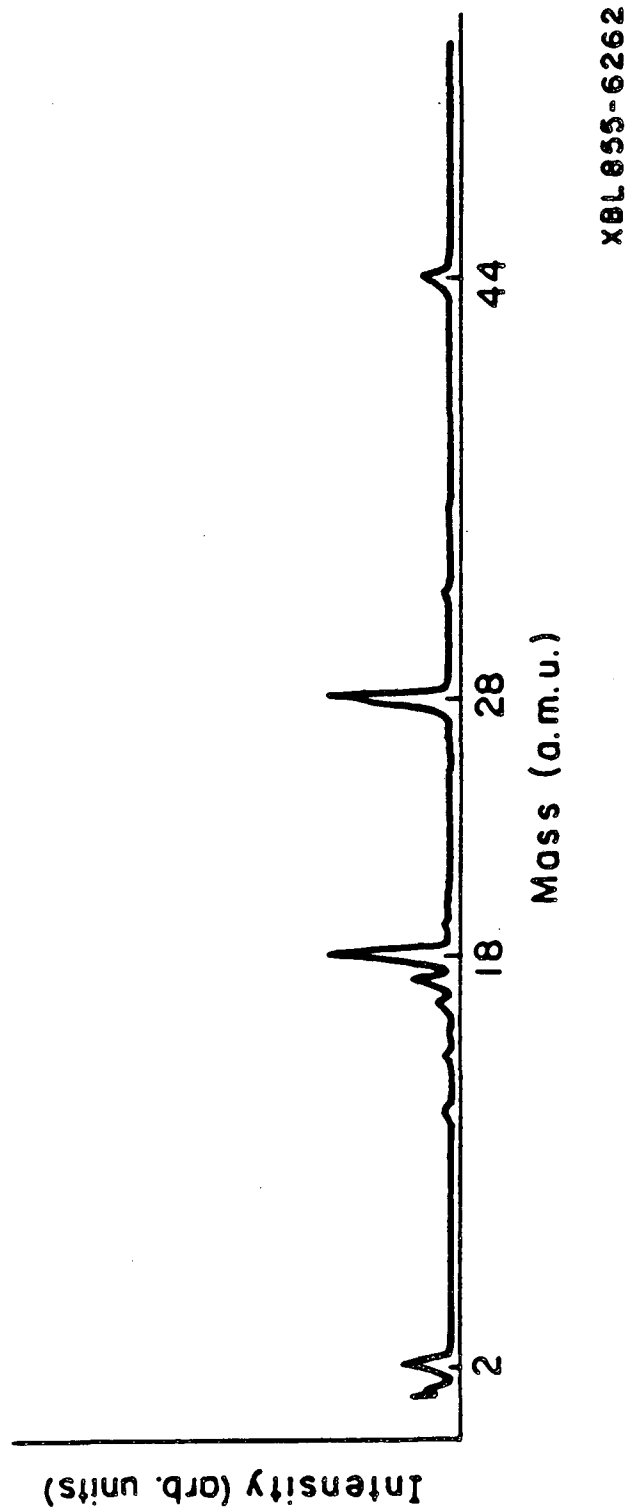
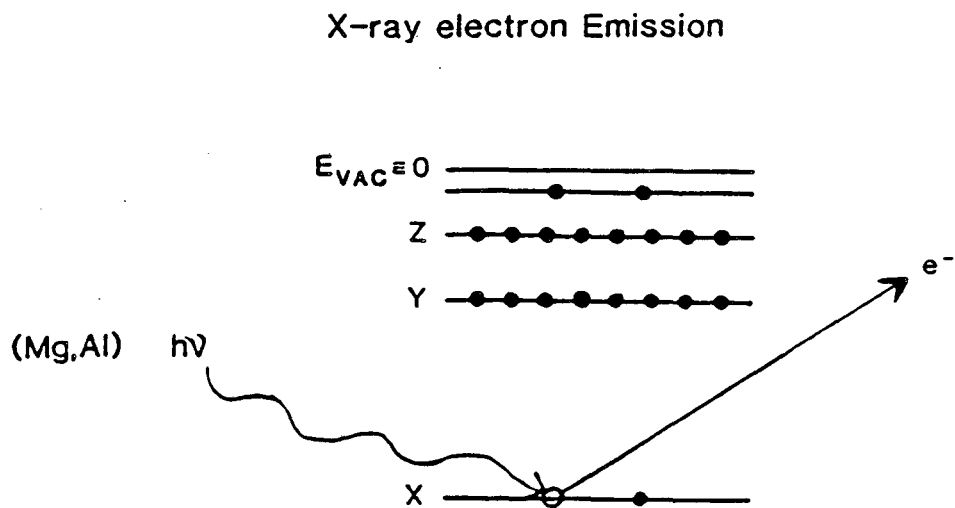
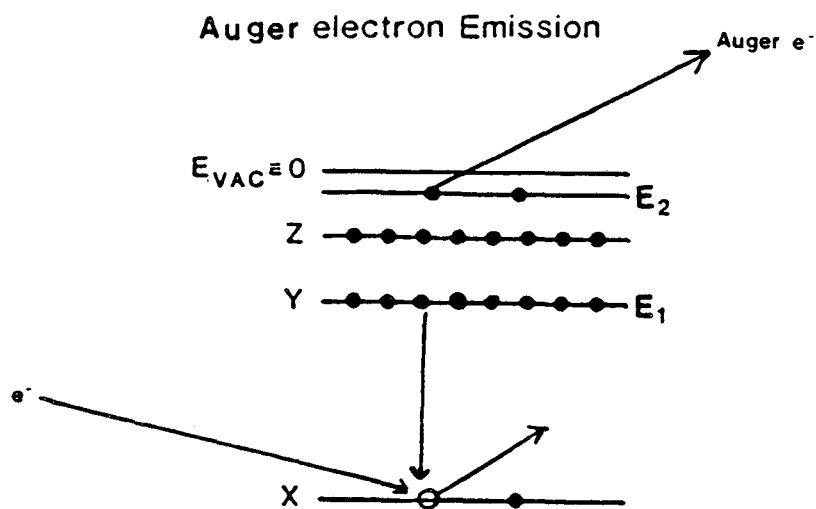


Figure 5.4.



$$h\nu = BE + KE + \Phi_{spec}$$



$$KE = [E_2 - E_1] - BE$$

Figure 5.5.

Double Pass Cylindrical Mirror Analyzer
Retarding Pulse Counting Mode

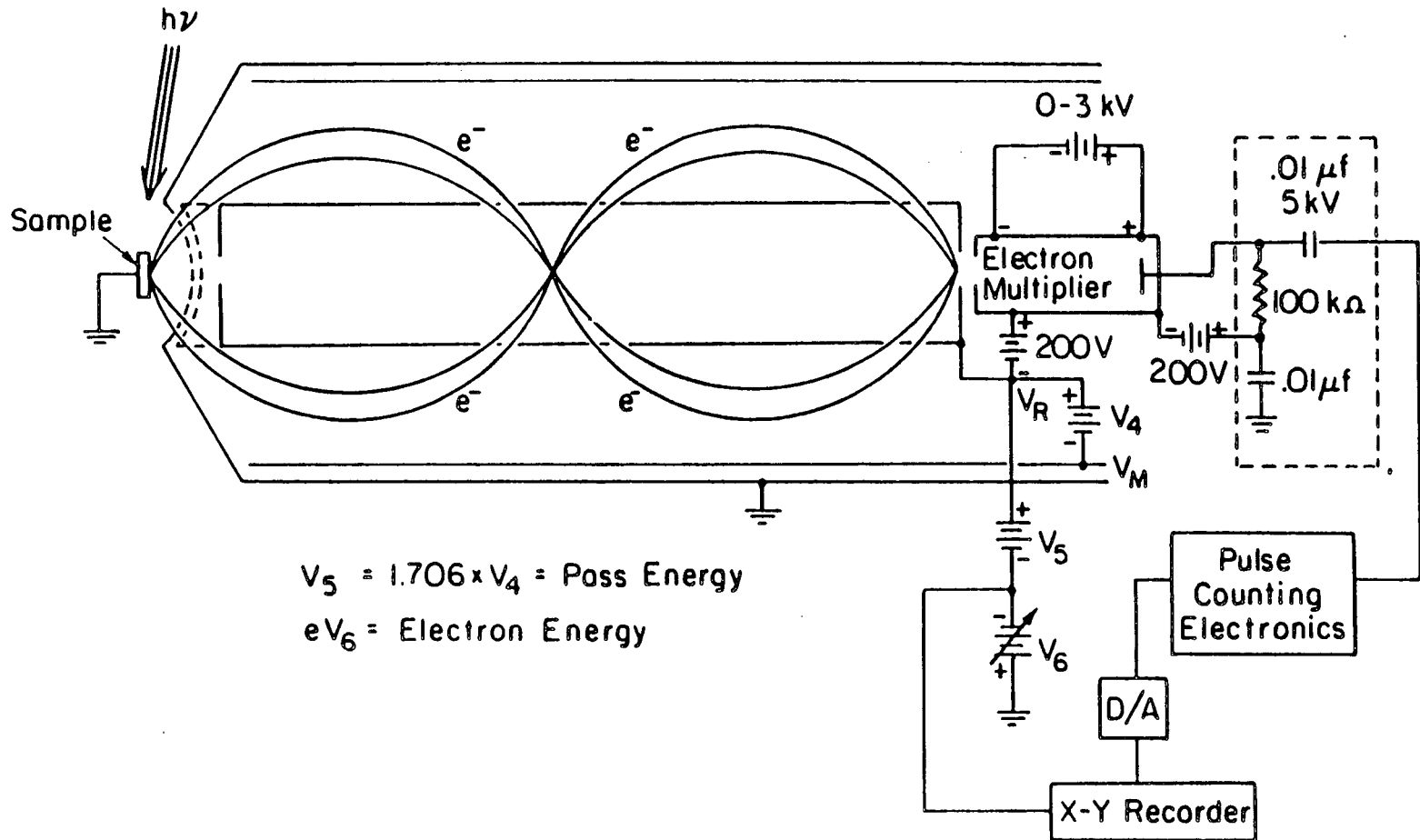


Figure 5.6.

XBL 842-6630

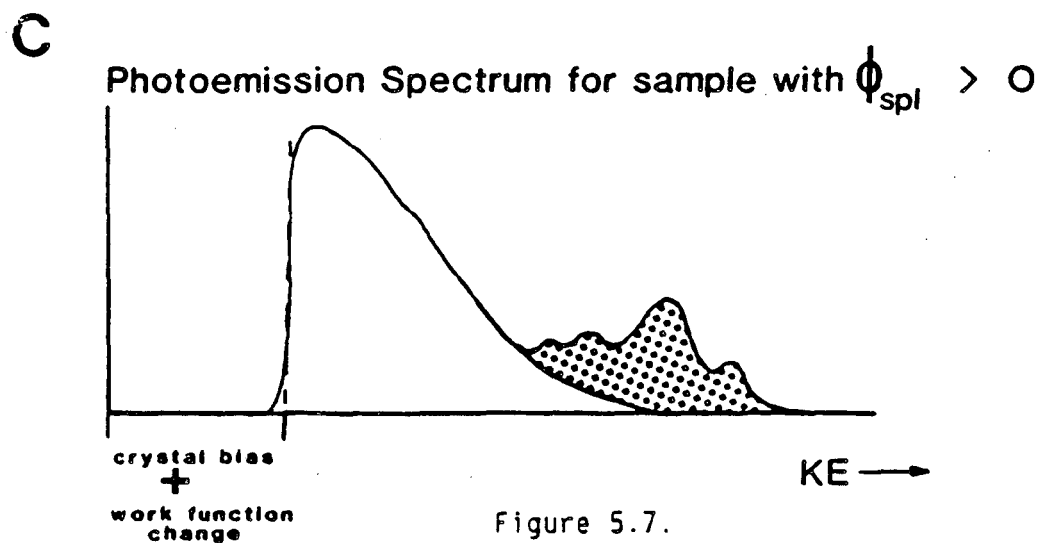
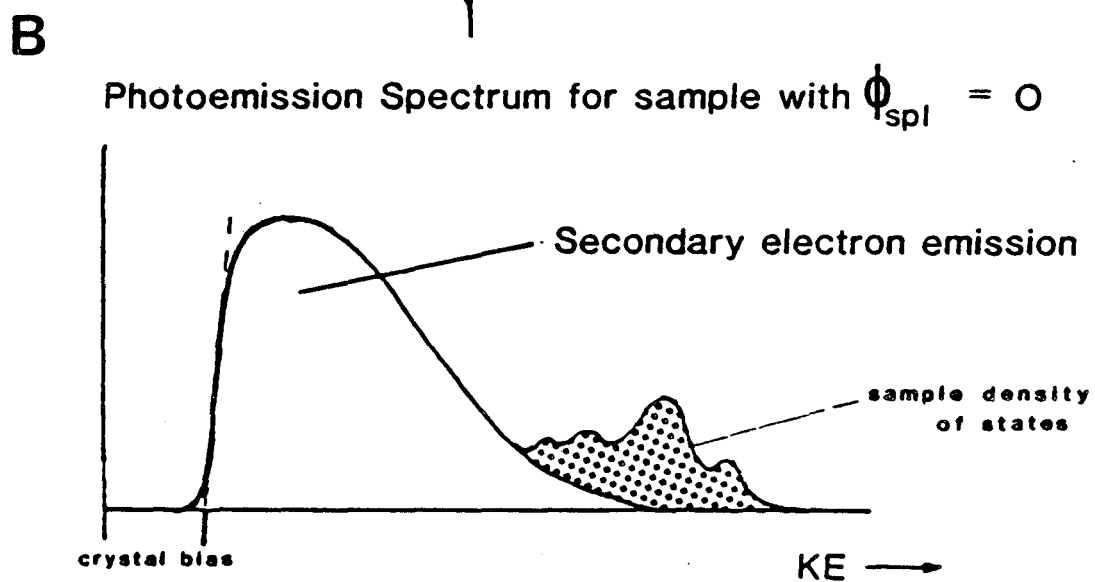
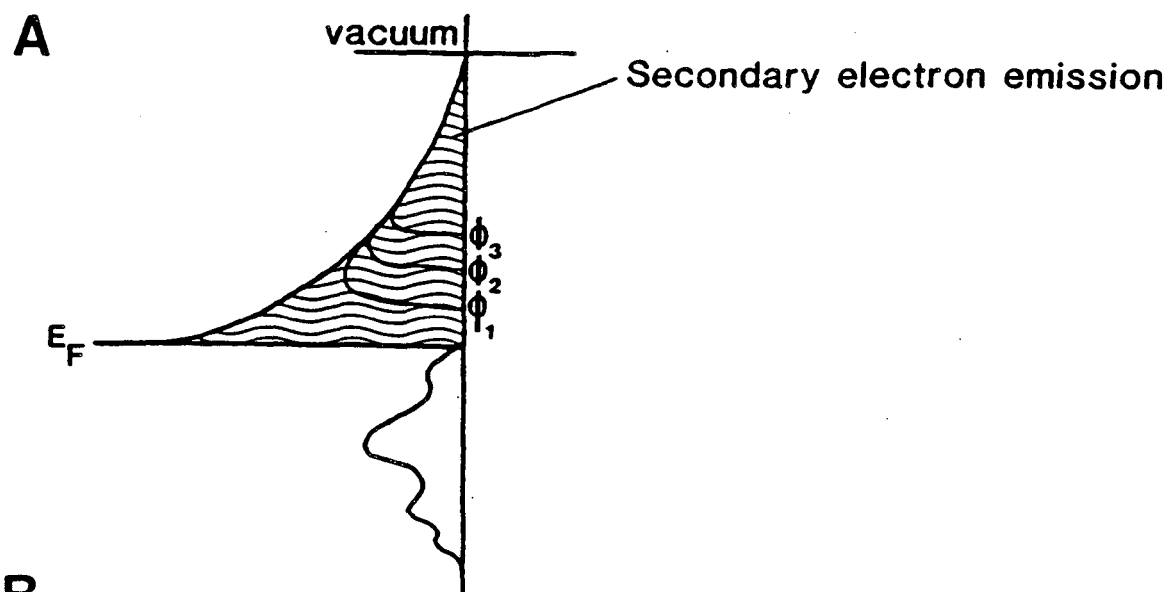
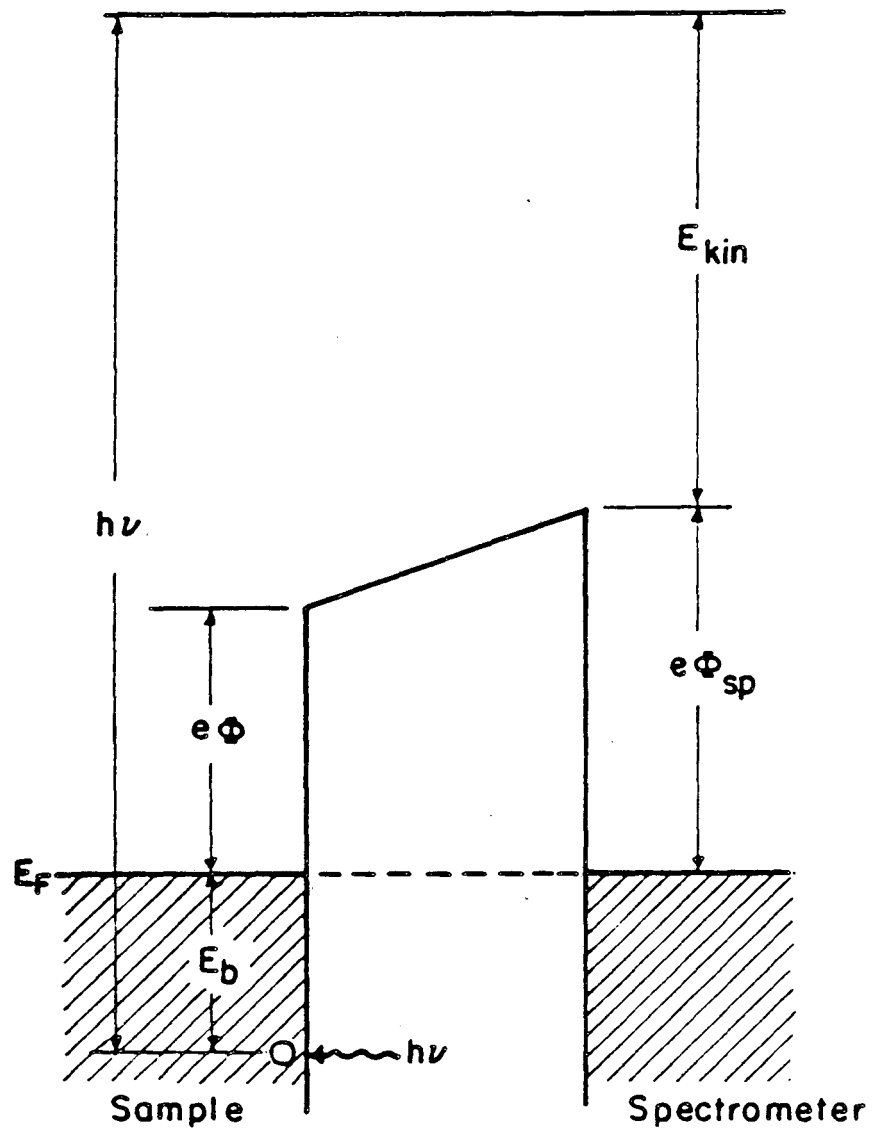


Figure 5.7.

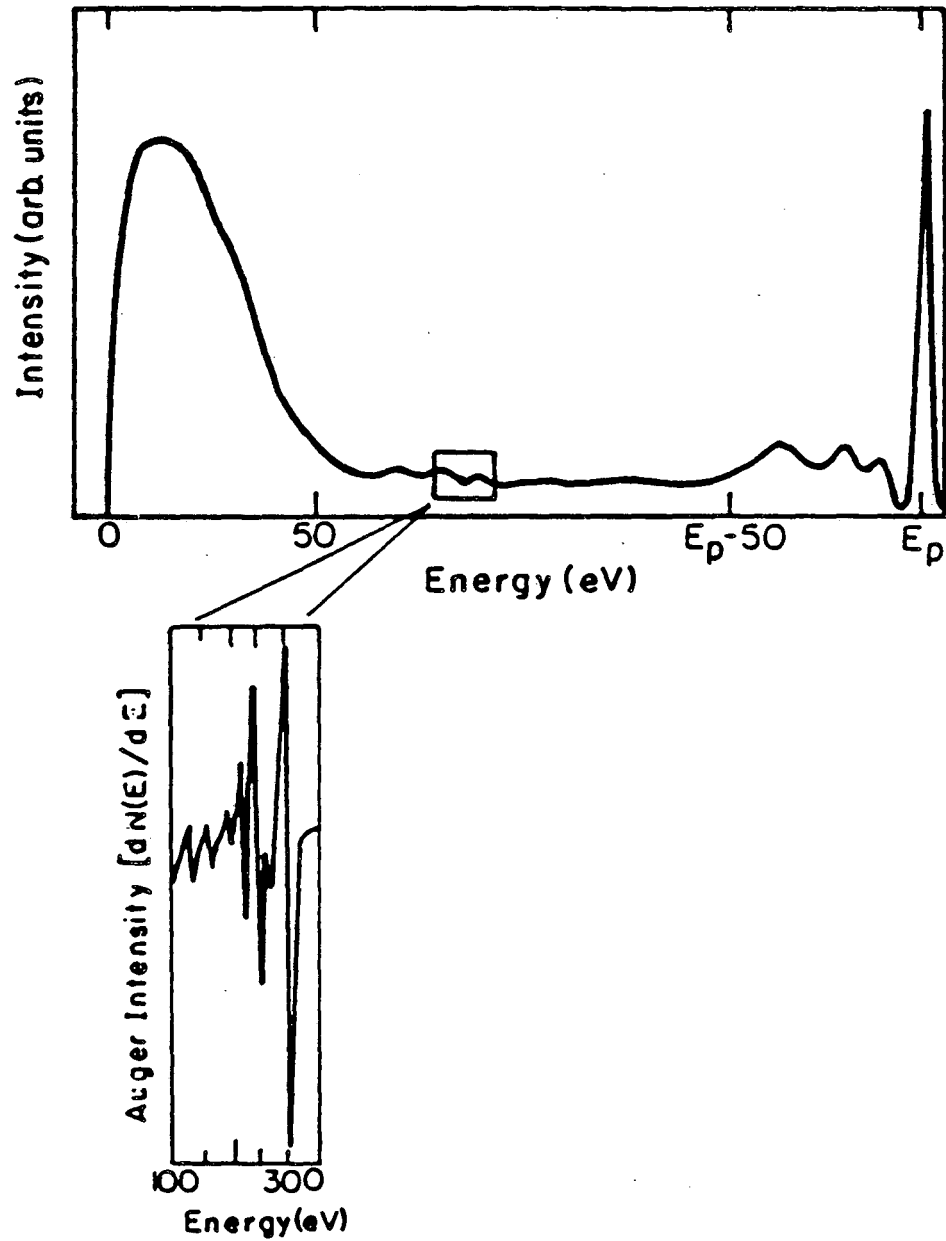
Photoelectron Spectroscopy



XBL 855-6270

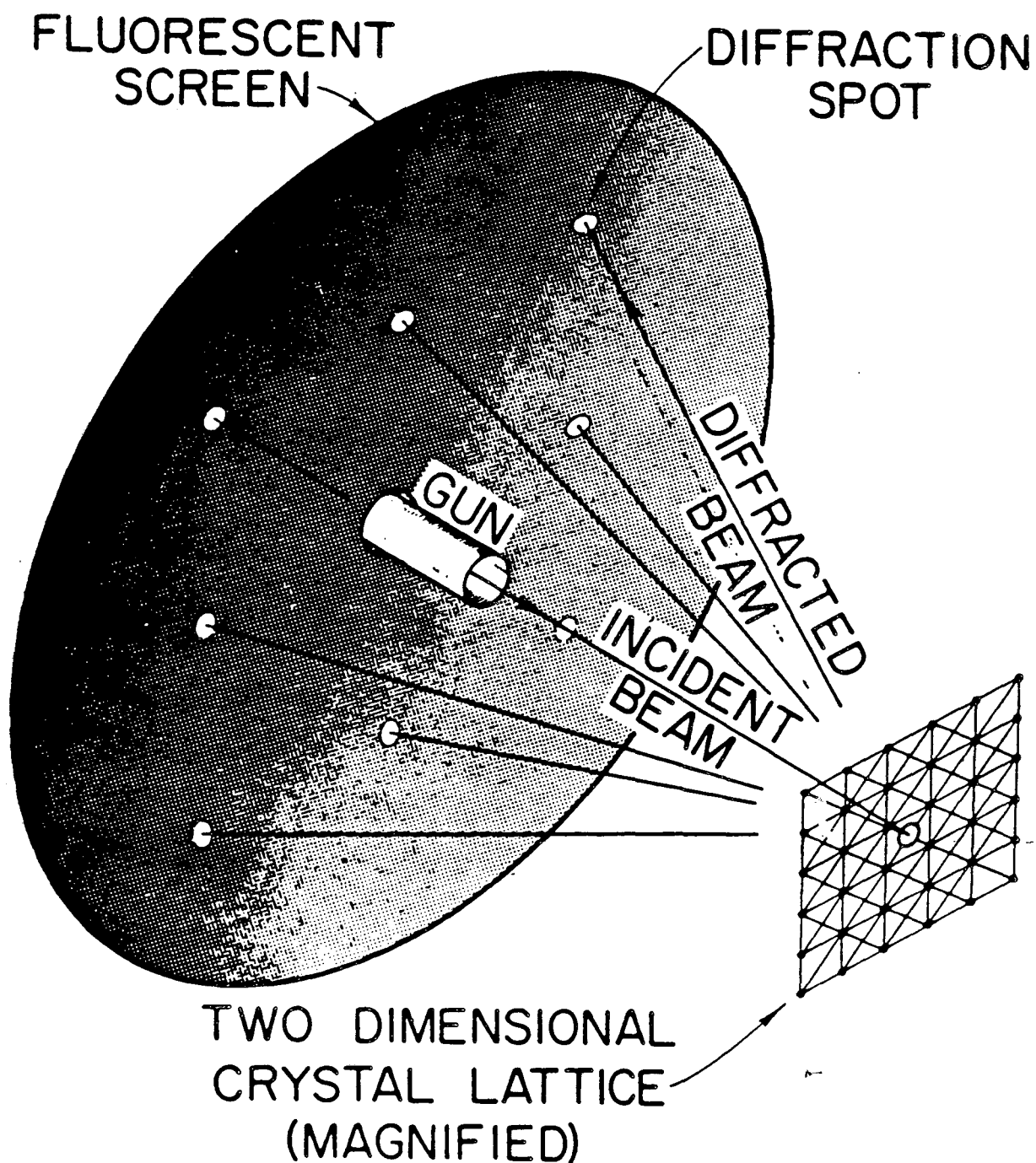
Figure 5.8.

Energy Distribution of Scattered Electrons from a Sample



XBL855-6261

Figure 5.9.



$$\vec{k}' = \vec{k} + \vec{G}$$

Figure 5.10.

UPS Spectra

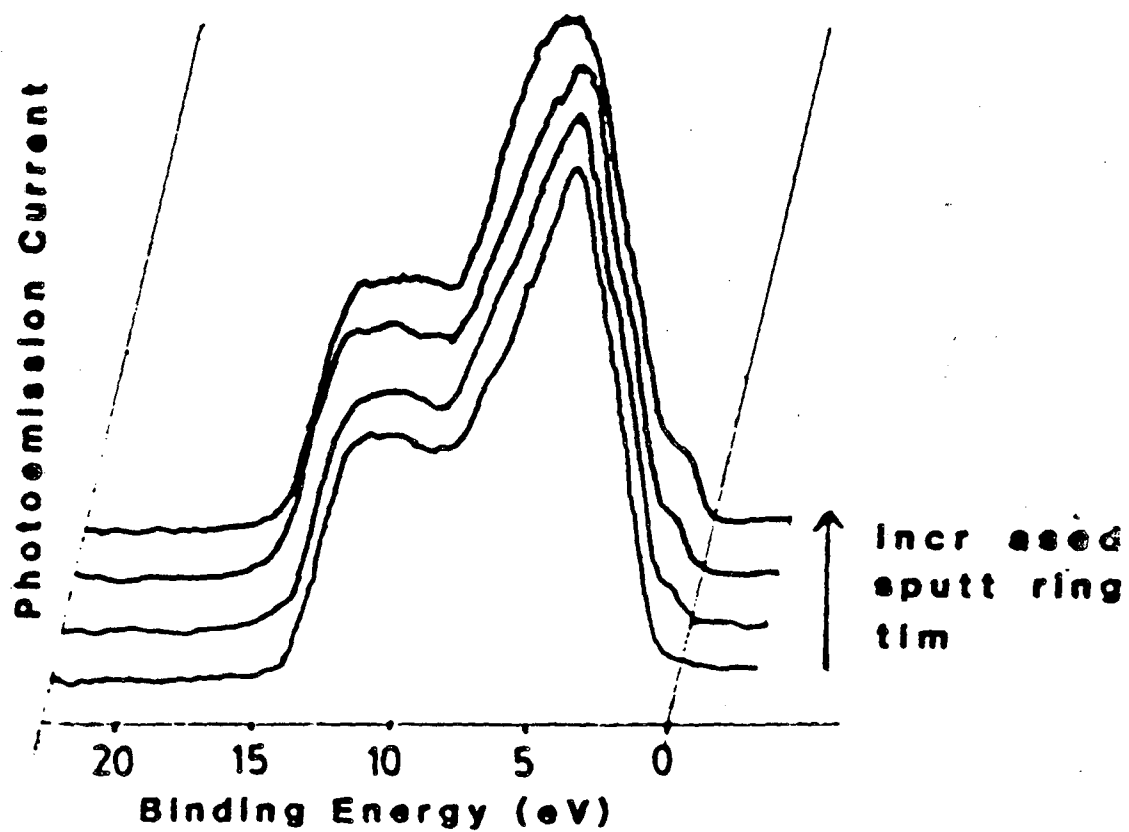


Figure 5.11.

successive Ar ion sputtering of Fe_2O_3 single crystals

UPS Difference Spectra

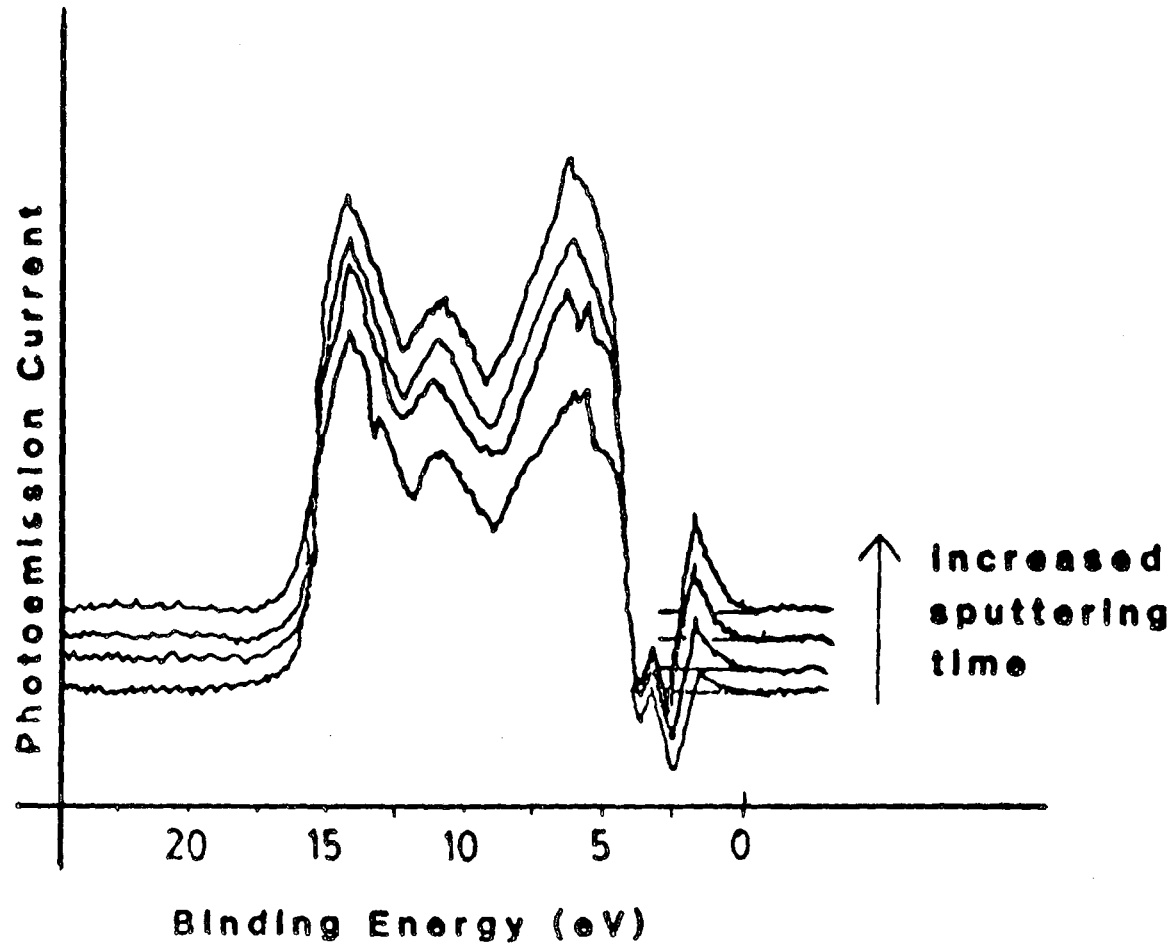


Figure 5.12.

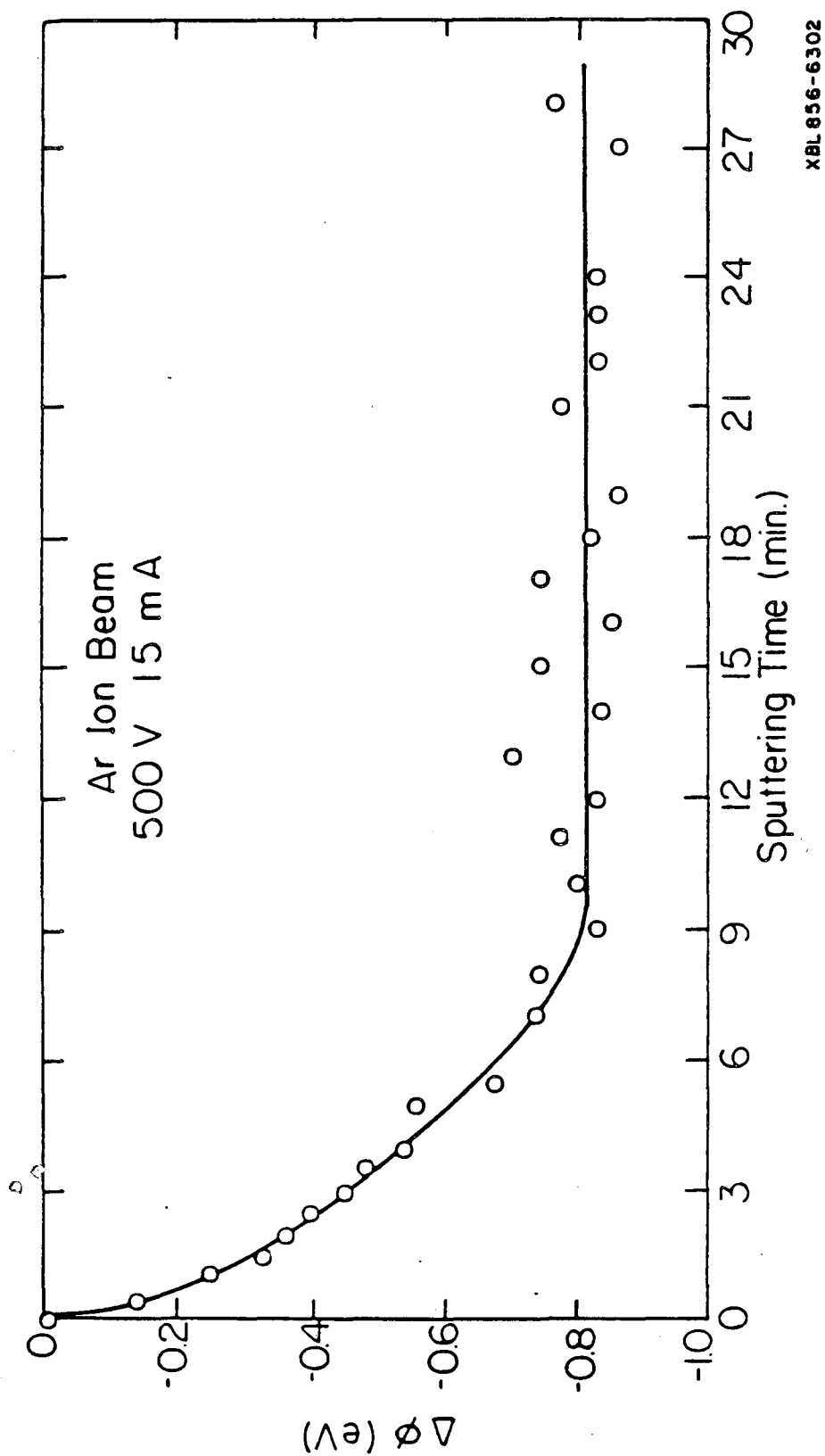
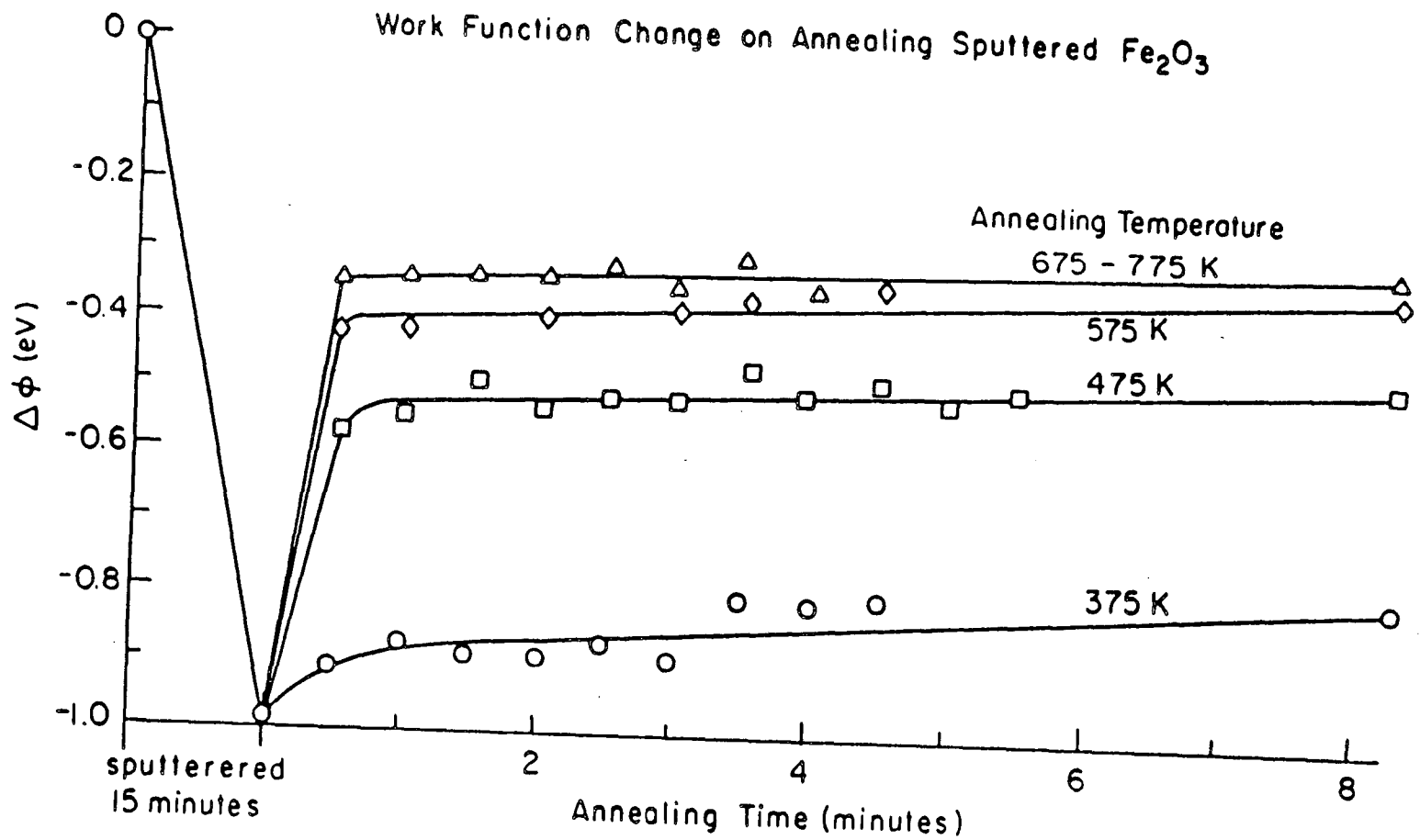
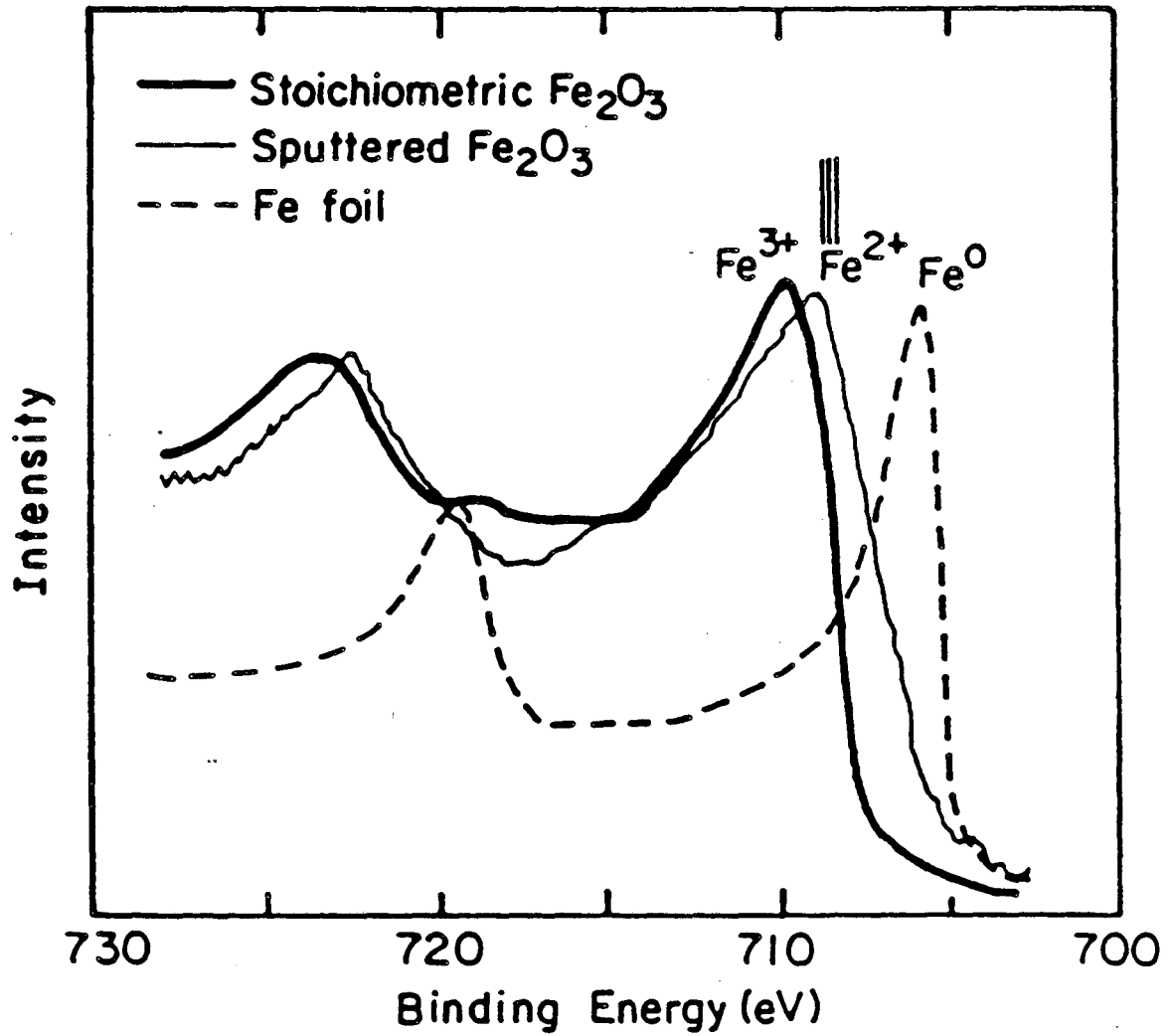


Figure 5.13.

Figure 5.14.

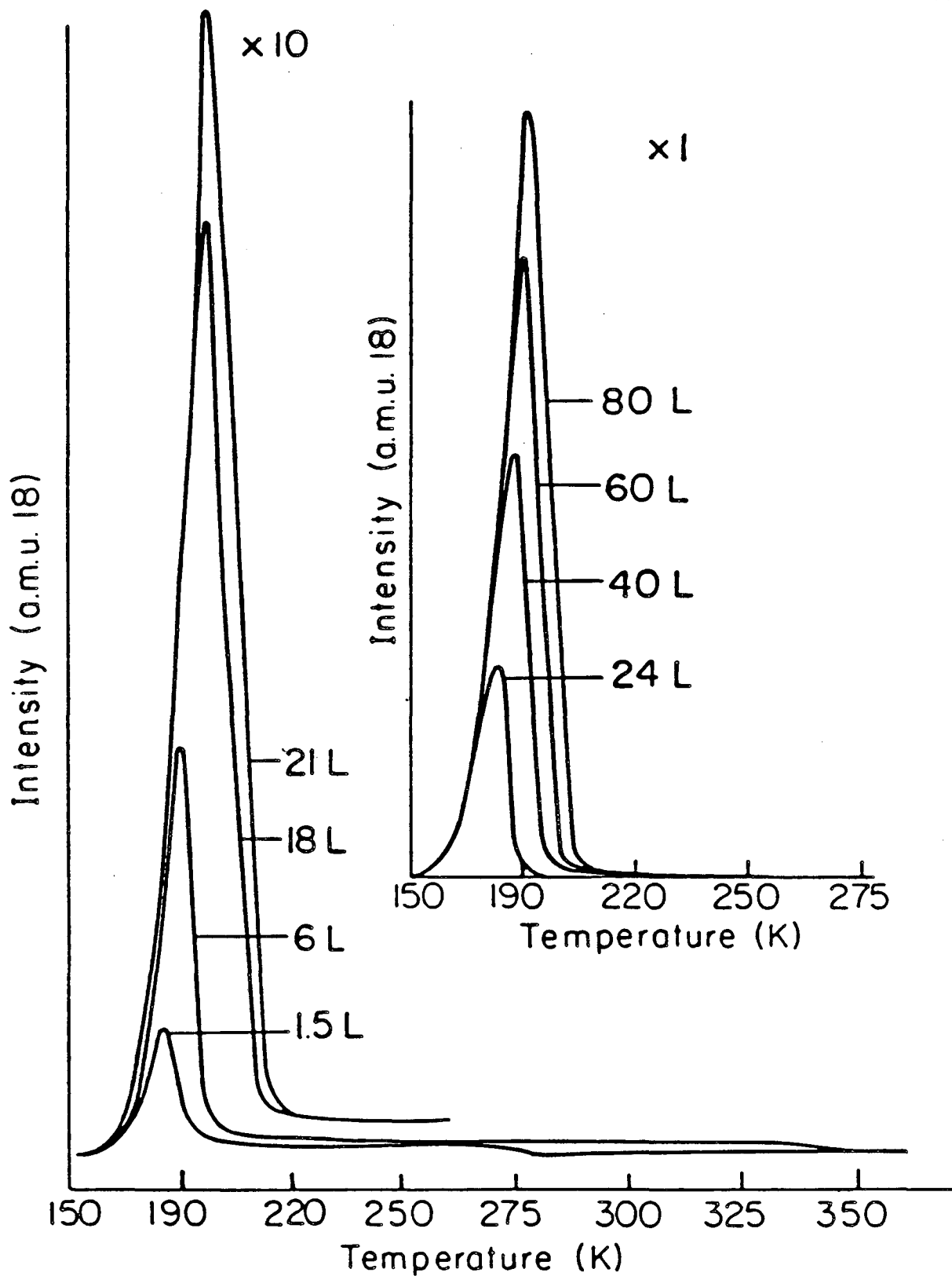


X-ray Photoelectron Spectra



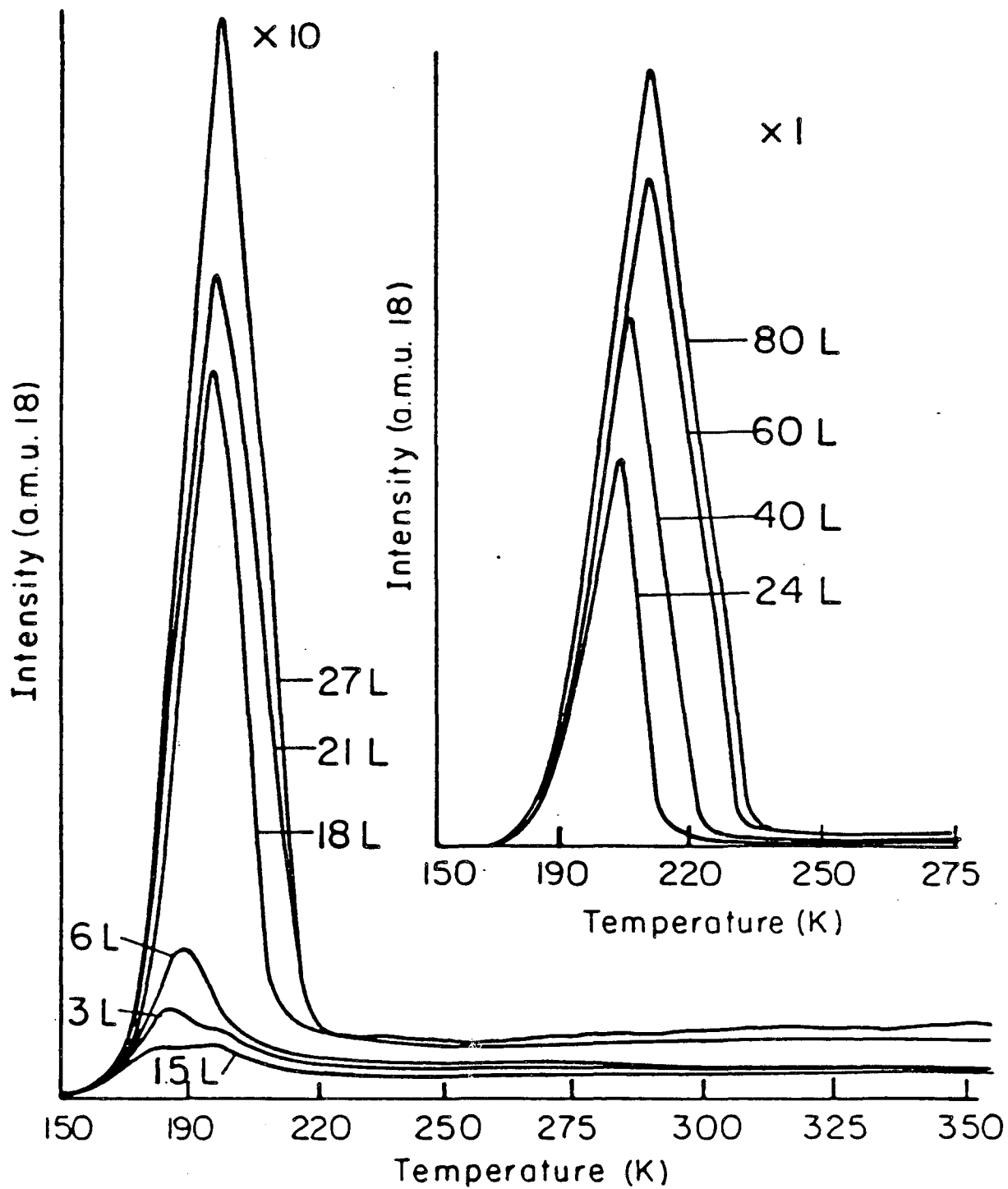
XBL 856-6296

Figure 5.15.



XBL 856-6297

Figure 5.16.



XBL 856-6298

Figure 5.17.

$\log(n_{\text{Fe}^{2+}}) \propto \text{rate of diffusion}$

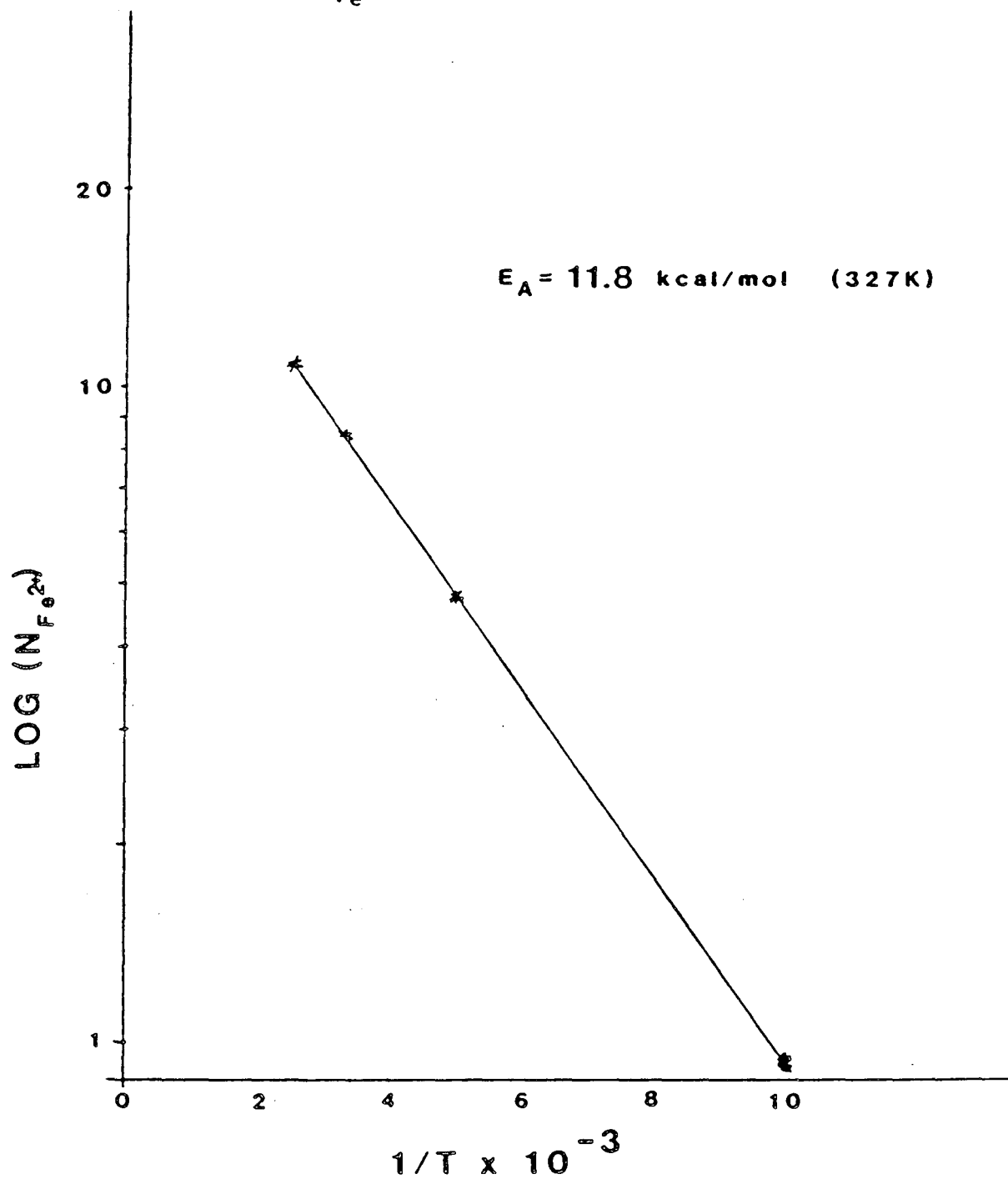


Figure 5.18.

H₂ Thermal Desorption From Iron Oxide AFTER SPUTTERING

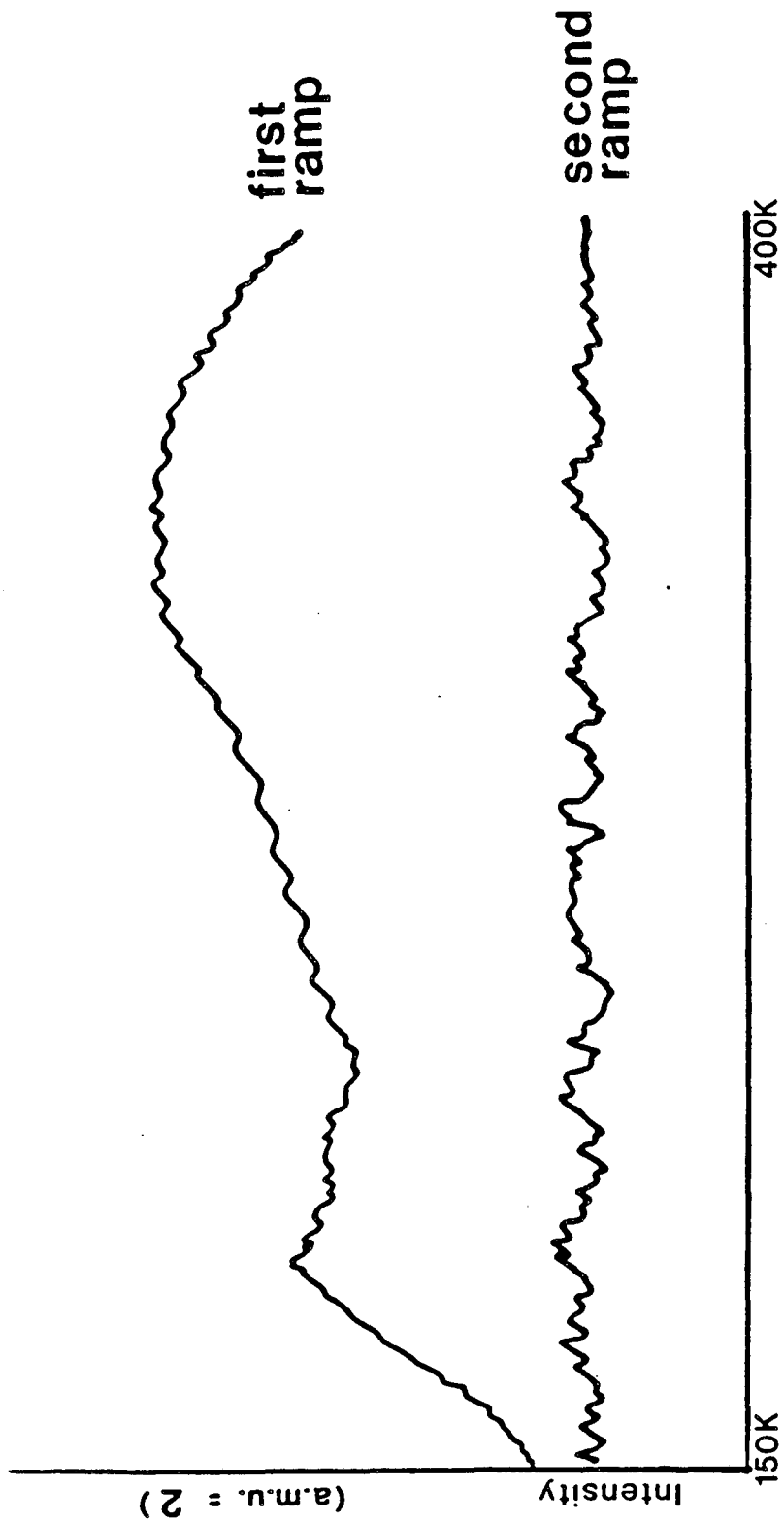


Figure 5.19.

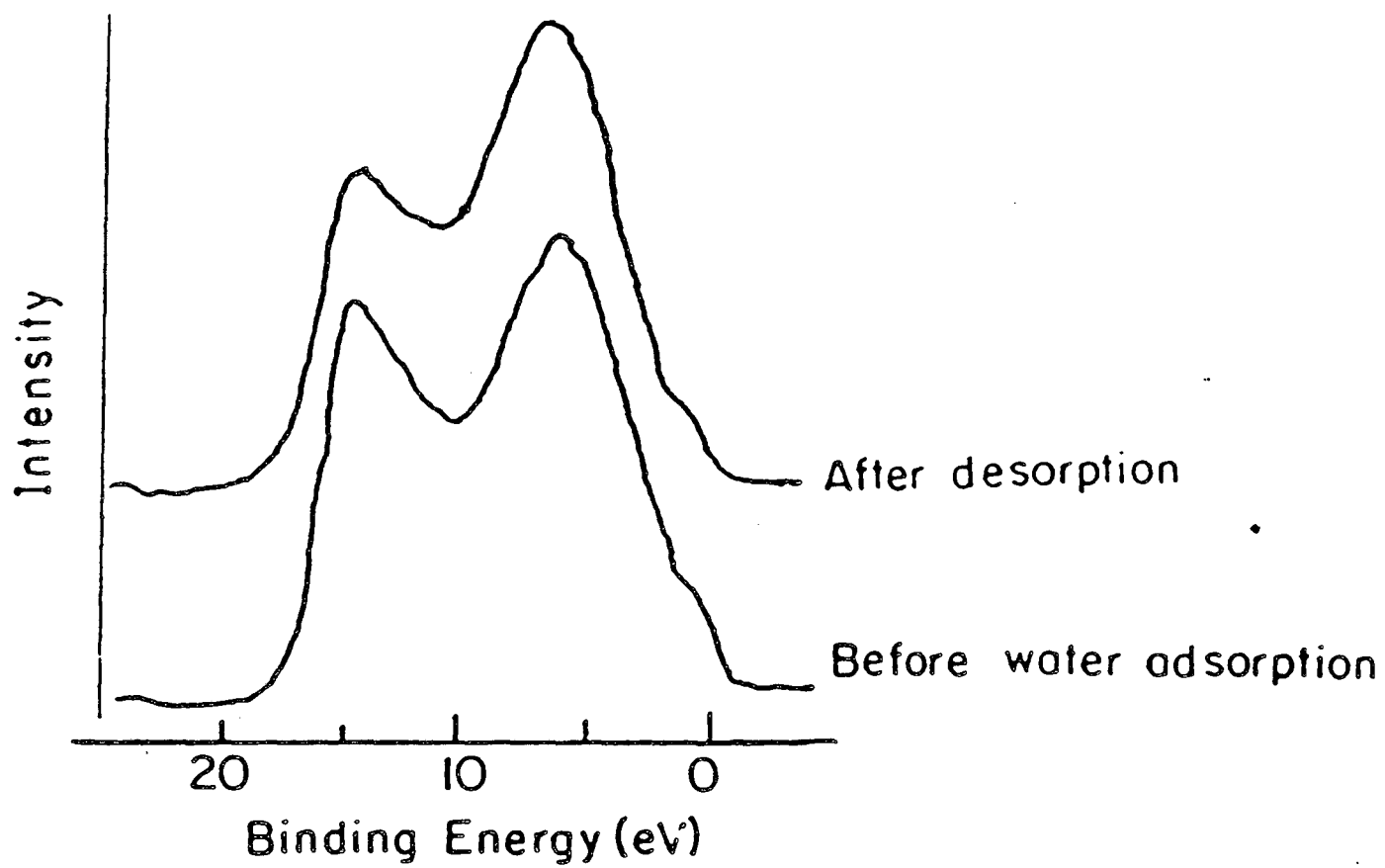


Figure 5.20.

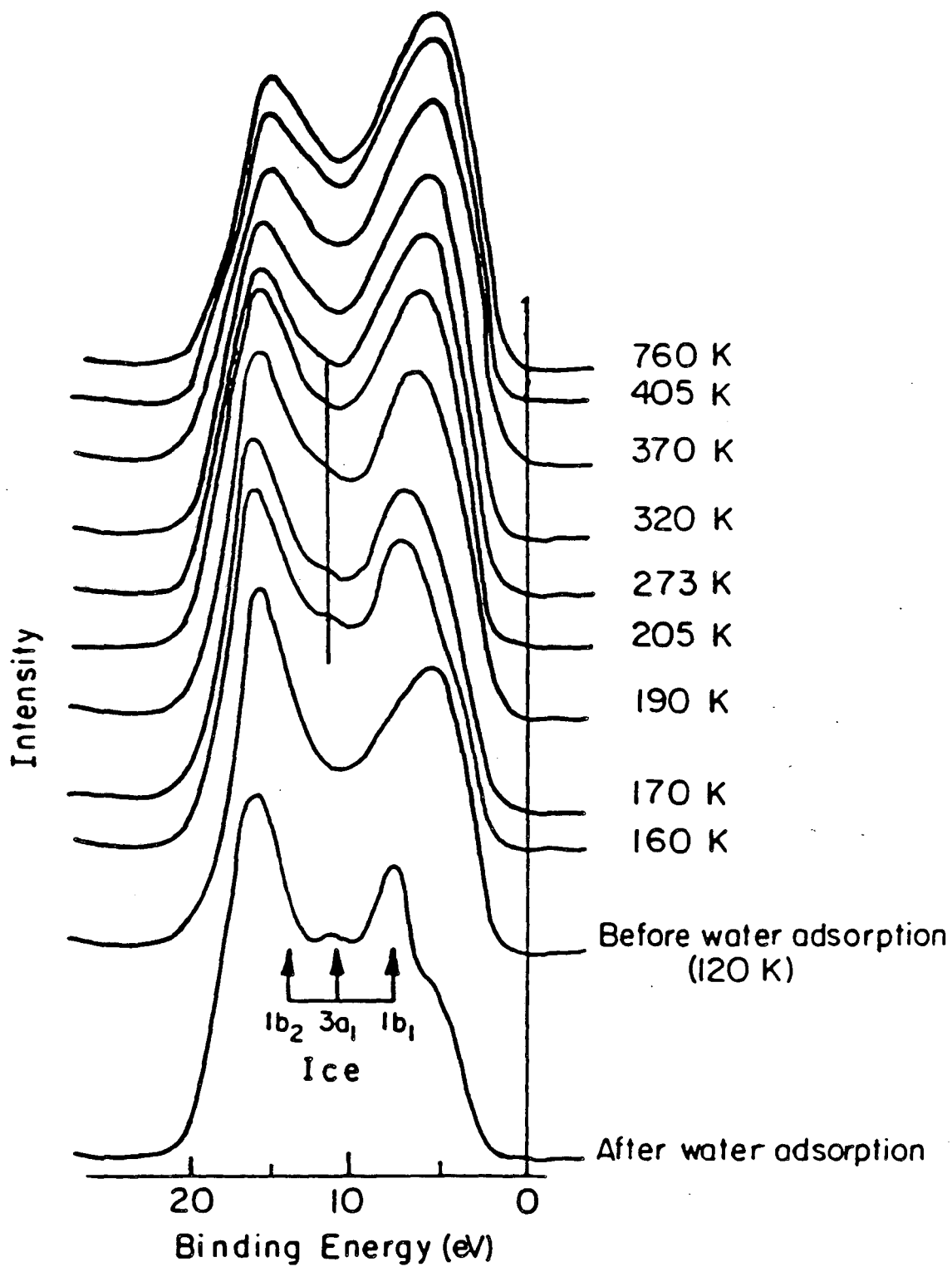


Figure 5.21.

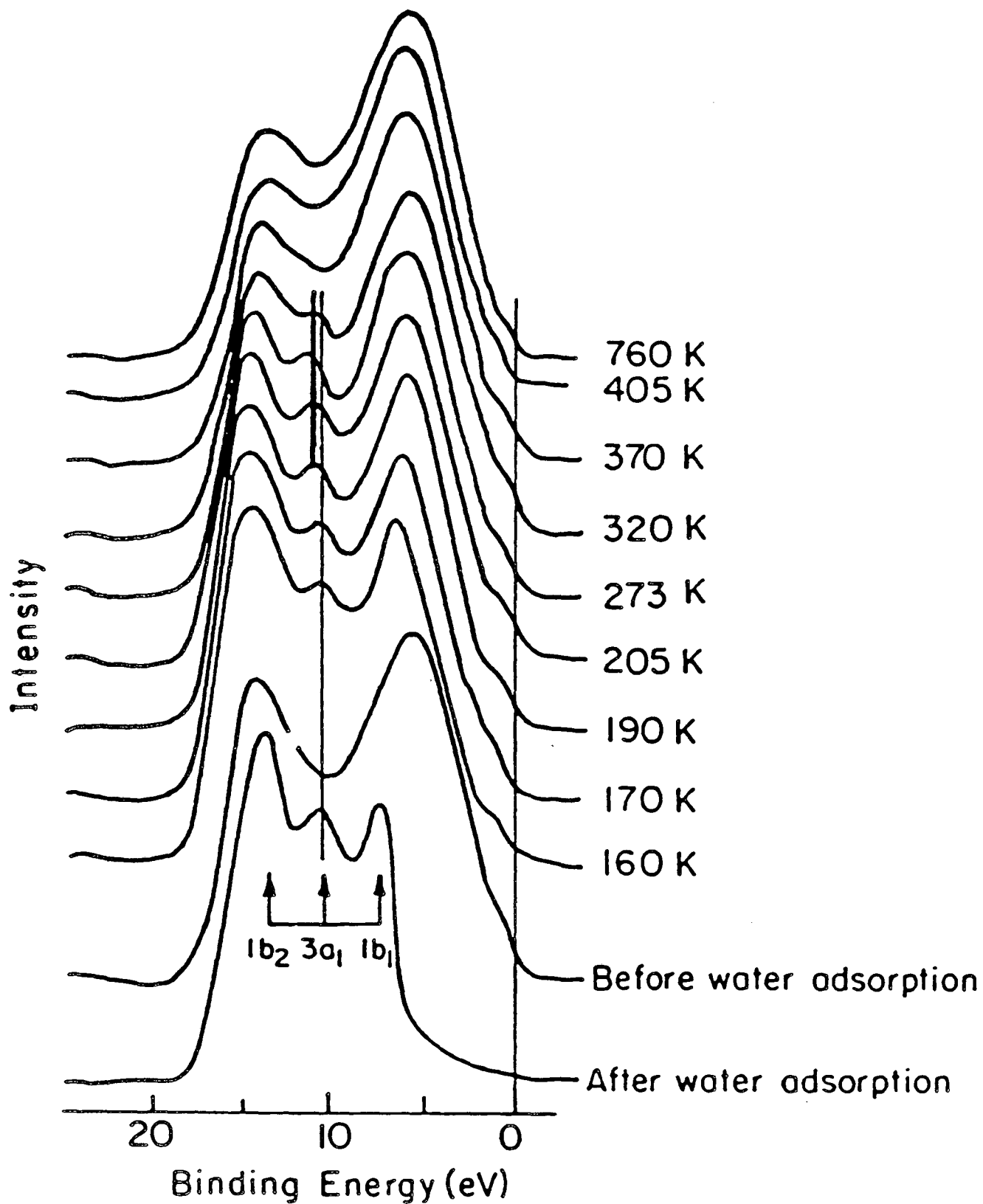


Figure 5.22.

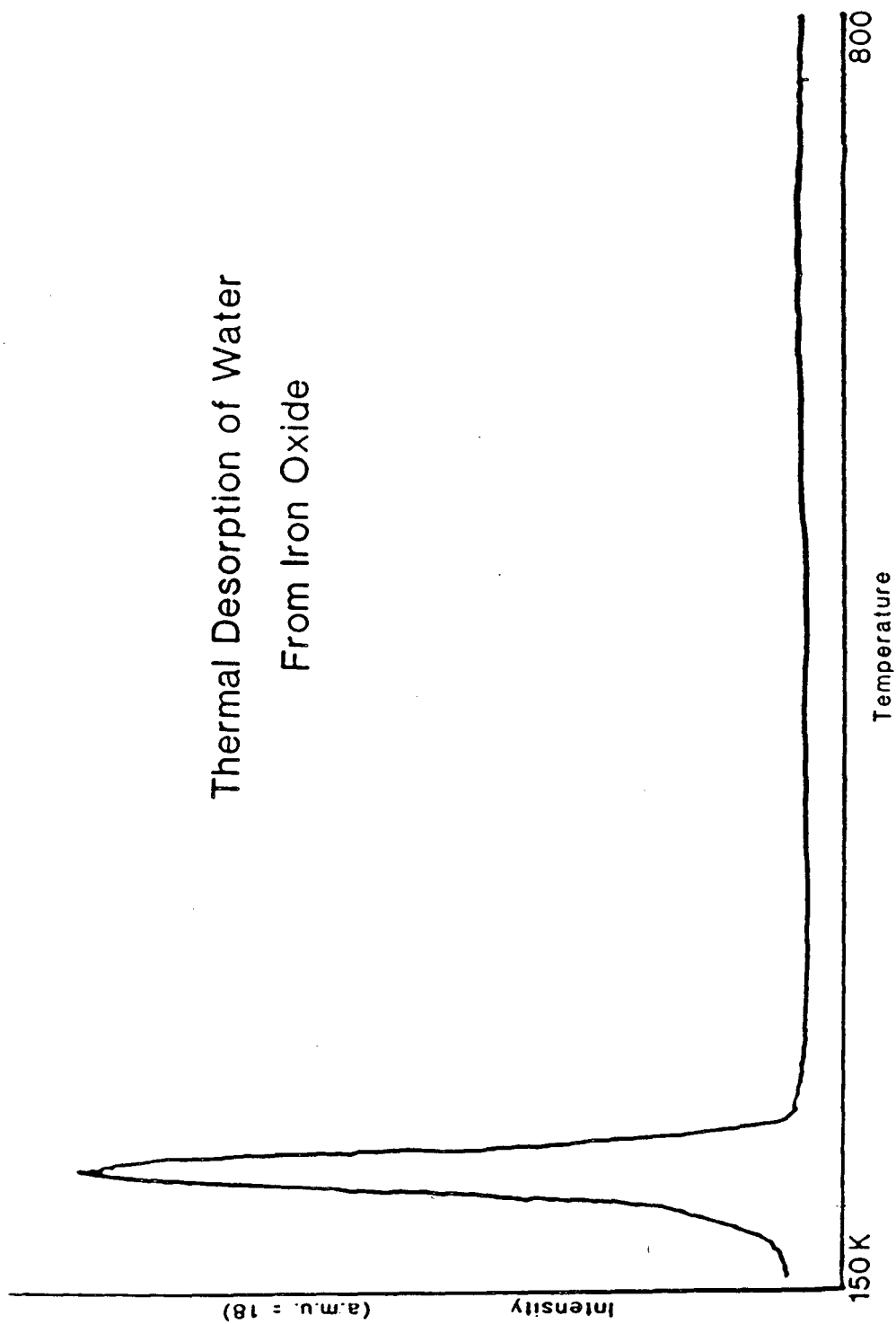
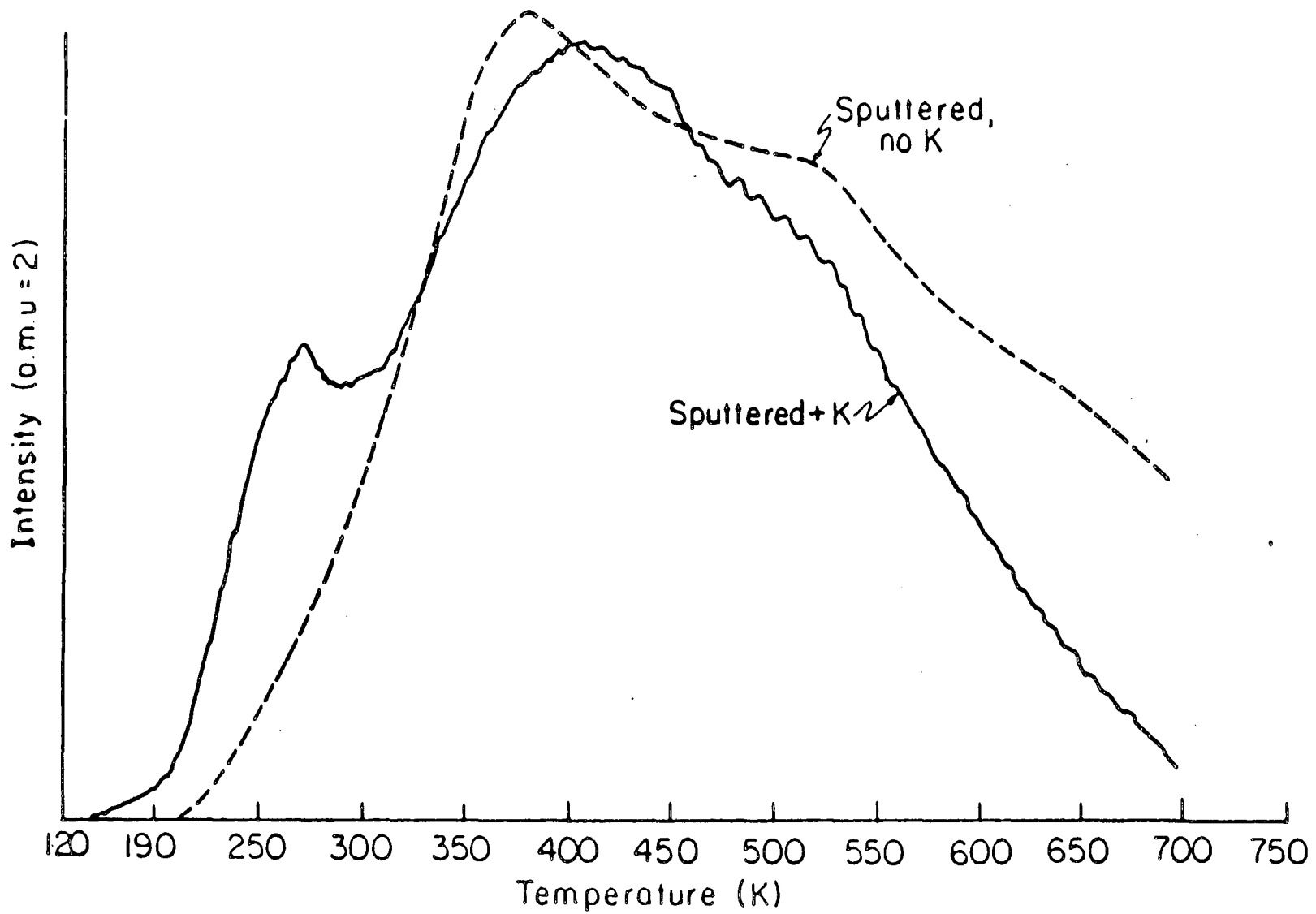


Figure 5.23.

Figure 5.24.



XBL 858-8300

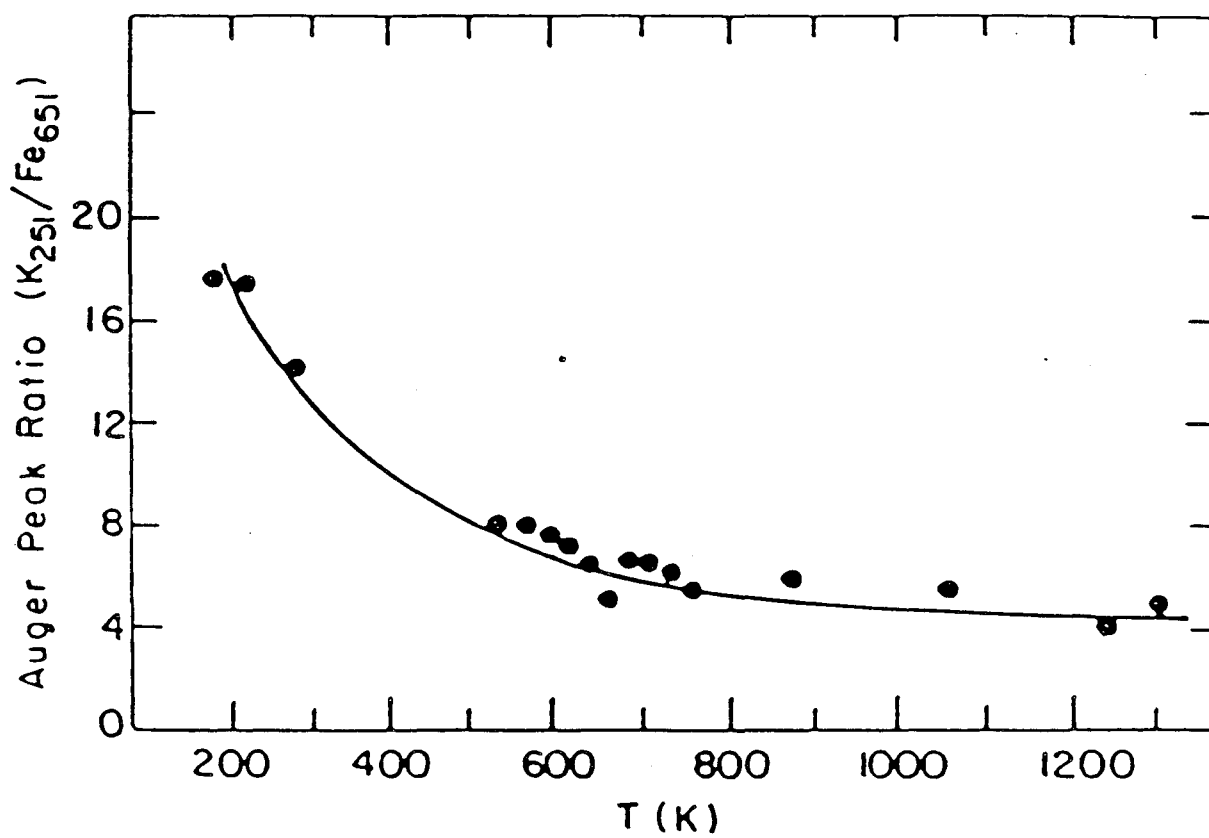


Figure 5.25.

References

- 5.1. A.B. Anderson, Surf. Sci., 105, 159 (1981).
- 5.2. N.C. Debnath, A.B. Anderson, Surf. Sci., 128, 61 (1983).
- 5.3. D.J. Dwyer, G.A. Simmons, A. Kaldor, Surf. Sci., 64, 617 (1977).
- 5.4. R.L. Kurtz, Surface Electronic Structure and Chemisorption on Corundum Transition Metal Oxides (Yale University, New Haven, CT, 1983).
- 5.5. P.D. Schulze, T.E. Neil, S.L. Shaffer, R.W. Smith, D.S. McKay, J. Vac. Sci. Technol., A3(1), 6 (1985).
- 5.6. K.D. Sieber, C. Sanchez, J.E. Turner, G.A. Somorjai, J. Chem. Soc., Faraday Trans. I, 81, 1263 (1985).
- 5.7. C.D. Wagner, W.H. Riggs, L.E. Davis, J.F. Moulder, G.E. Muilenberg, Handbook of Photoelectron Spectroscopy, Perkin Elmer Corp., Minnesota 1978.
- 5.8. G. Ertl, J. Küppers, Low Energy Electrons and Surface Chemistry, Verlag-Chemie, Germany 1974.
- 5.9. The software for the LSI-11 UTI thermal desorption was obtained from Cornell University by Simon Bare.
- 5.10. F. Zaera, Ph.D. Thesis, University of California, Berkeley, August 1984.
- 5.11. P.A. Redhead, Vacuum, 12, 203 (1962).
- 5.12. M. Khudar, personal communication. Preliminary results of ammonia synthesis from nitrogen bubbled through water using reduced iron oxide powders.
- 5.13. H. Nakanishi, C. Sanchez, M. Hendewerk, G.A. Somorjai, to be published.

- 5.14. C. Leygraf, M. Hendewerk, G.A. Somorjai, *J. Cat.*, 78, 341 (1982).
- 5.15. K.D. Sieber, C. Sanchez, J.E. Turner, G.A. Somorjai, *Mat. Res. Bull.*, 20, 153 (1985).
- 5.16. S.R. Kelemen, A. Kaldor, D.J. Dwyer, *Surf. Sci.*, 121, 45 (1982).
- 5.17. C.R. Brundle, T.J. Chuang, K. Wandelt, *Surf. Sci.*, 68, 459 (1977).
- 5.18. G.C. Allen, M.T. Curtis, A.J. Hooper, P.M. Tucker, *J. Chem. Soc., Dalton Trans.*, 1525 (1974).
- 5.19. P.D. Schulze, T.E. Neil, S.L. Shaffer, R.W. Smith, D.S. McKay, *J. Vac. Sci. Technol. (A)*, 3, 6 (1985).
- 5.20. G.B. Fischer, B.A. Sexton, *Phys. Rev. Letters*, 44, 683 (1980).
- 5.21. D.J. Dwyer, S.R. Keleman, A. Kaldor, *J. Chem. Phys.*, 76, 1832 (1982).
- 5.22. R.L. Kurtz, V.E. Heinrich, *Phys. Rev. B*, 25, 3563 (1982).
- 5.23. T.F. Barth, *J. Chem. Phys.*, 3, 323 (1935).
- 5.24. G.C. Allen, M.T. Curtis, A.J. Hooper, P.M. Tucker, *J.C.S. Dalton*, 1525 (1974).
- 5.25. C. Leygraf, M. Hendewerk, G.A. Somorjai, *J. Cat.*, 78, 341 (1982).
- 5.26. F.T. Wagner, G.A. Somorjai, *Nature*, 285, 559 (1980).

- J.A. Tossel, K.J. Vaughan, K.H. Johnson, *Nature*, 244, 42 (1973).
73. S. Lowell, Introduction to Powder Surface Area, Wiley Interscience, N.Y. 1979.
74. a) T. Dawai, T. Sakata, *J. Chem. Soc., Chem. Commun.*, 1980, 694 (1980). b) *Nature*, 256, 474 (1980). c) *Chem. Phys. Letters*, 72, 87 (1980).
75. S. Sato, J.M. White, *Chem. Phys. Letters*, 72, 87 (1980).
76. A.J. Nozik, *Ann. Rev. Phys. Chem.*, 29, 189 (1978).
77. J.B. Goodenough, "Metallic Oxides", in Progress in Solid State Chemistry. ed. by H. Reiss (Pergamon Press, N.Y., 1971), p. 297.
78. C.M. Srivastava, *Bull. Mat. Sci.*, 5, 247 (1983).
79. P. Merchant, R. Collins, K. Dwight, A. Wold, *J. Sol. St. Chem.*, 27, 307 (1979).
80. L.A. Marusak, R. Messier, W.B. White, *J. Phys. Chem. Solids*, 41, 981 (1980).
81. J.A. Tossell, D.J. Vaughan, K.H. Johnson, *Nature*, 246, 42 (1973).
84. S. Lowell, *Anal. Chem.* 45, 1576 (1973).
85. R. Degryse, W.P. Gomes, F. Cardon, J. Vennik, *J. Electrochem. Soc.*, 122, 711 (1975).
88. B.M. Warnes, F.F. Aplan, G. Simkovich, *Sol. St. Ionics*, 12, 271 (1984).

This report was done with support from the Department of Energy. Any conclusions or opinions expressed in this report represent solely those of the author(s) and not necessarily those of The Regents of the University of California, the Lawrence Berkeley Laboratory or the Department of Energy.

Reference to a company or product name does not imply approval or recommendation of the product by the University of California or the U.S. Department of Energy to the exclusion of others that may be suitable.

*LAWRENCE BERKELEY LABORATORY
TECHNICAL INFORMATION DEPARTMENT
UNIVERSITY OF CALIFORNIA
BERKELEY, CALIFORNIA 94720*